THE CONVERGENCE PROPERTIES AND APPLICATIONS OF THE INVARIANT IMBEDDING T-MATRIX AND PSEUDO-SPECTRAL TIME DOMAIN METHODS

A Dissertation

by

SIYAO ZHAI

Submitted to the Office of Graduate and Professional Studies of
Texas A&M University
in partial fulfillment of the requirements for the degree of

DOCTOR OF PHILOSOPHY

Chair of Committee,	Richard Lee Panetta
Co-Chair of Committee,	Ping Yang
Committee Members,	Sarah Brooks
	Edward Fry
Head of Department,	R. Saravanan

August 2019

Major Subject: Atmospheric Sciences

ABSTRACT

This study focuses on investigating and improving the convergence of two numerical schemes for electromagnetic single scattering simulations: The pseudo-spectral time domain (PSTD) method and the invariant-imbedding T-matrix (II-TM) method. The single scattering properties (phase matrix, extinction, scattering cross section, etc.) can be obtained with these two methods for non-spherical and inhomogeneous particles. The single scattering properties are vital input for radiative transfer simulations of the atmosphere and oceans and are also used in retrievals for interpreting satellite observations of the atmosphere and surface.

PSTD and II-TM are numerically exact methods because they solve Maxwell's Equations. Given the proper choice of model parameters, their model outputs could be made as close as possible to the real solution. In this study, we study their convergence behaviors to make sure that they actually converge to the right solution. Specifically, for PSTD, we study the electromagnetic near field in its computational domain to see how the near field decays to zero. This is important since it determines how long we should integrate the discretized Maxwell's equation in time domain. For the II-TM method, we study the Gaussian quadrature employed to compute the surface integrations. In the version of II-TM for hexagonal columns, we modify the original quadrature scheme to avoid quadrature over discontinuities. We also implement a new node and weight generating method into II-TM. These two improvements greatly accelerated II-TM method for hexagonal columns and spheroids.

An application of II-TM and a physical geometric optics method (PGOM) is presented. The application is to compute and compile a dataset intended for marine hydrosols. A hexahedral ensemble is used to simulate the complicated particle geometry. The size and refractive indices included in the dataset cover most natural marine hydrosols. We compare the single and bulk scattering properties of our hexahedra dataset with those obtained with the Lorenz-Mie method and discover major differences in the shape of the volume scattering function.

DEDICATION

To my family

ACKNOWLEDGEMENTS

I would like to thank my committee chair, Dr. Panetta, co-chair Dr. Ping Yang and my committee members, Dr. Sarah Brooks, Dr. Edward Fry, for their guidance and support throughout the course of my research.

Thanks also go to my friends and colleagues and the department faculty and staff for making my time at Texas A&M University a great experience.

Finally, thanks to my mother and father for their encouragement and love.

CONTRIBUTORS AND FUNDING SOURCES

Contributors

This work was supervised by a dissertation committee consisting of Professor Richard Panetta, Professor Ping Yang, Professor Sarah Brooks of the Department of Atmospheric Sciences department, and Professor Edward Fry of the Department of Physics and Astronomy.

This study is supported by NSF awards AGS-1338440 and OCE-1459180.

NOMENCLATURE

II-TM	Invariant imbedding T-matrix
FDTD	Finite difference time domain
PSTD	Pseudo spectral time domain
DDA	Discrete dipole approximation
IGOM	Improved geometric optics method
PGOM	Physical geometric optics method
EBCM	Extended boundary condition method
VRTE	Vector radiative transfer equation
VSWF	Vector spherical wave functions
RE	Relative error
IOP	Inherent optical properties
g	Asymmetry factor
SSA	Single scattering albedo
VSF	Volume scattering function

TABLE OF CONTENTS

Page

ABSTRACT ii

DEDICATION iv

ACKNOWLEDGEMENTS v

CONTRIBUTORS AND FUNDING SOURCES vi

NOMENCLATURE vii

TABLE OF CONTENTS viii

LIST OF FIGURES x

LIST OF TABLES xiv

1. INTRODUCTION 1

1.1. Single scattering 7

2. THE PSEUDO SPECTRAL TIME DOMAIN METHOD 14

2.1. Pseudo-spectral time domain (PSTD) method 15
2.2. 2-dimensional PSTD simulations to understand the near field behavior 25

3. THE INVARIANT IMBEDDING T-MATRIX METHOD 51

3.1. The invariant imbedding T-matrix method 54
3.2. Improving the surface integrations in U-matrix elements 79
3.3. Accelerating the node generating scheme for Gaussian quadrature in II-TM 95

4. MARINE HYDROSOL SINGLE SCATTERING DATASET 99

4.1. Water constituents 100
4.2. The hexahedral ensemble dataset 104
4.3. The physical geometric optics method (PGOM) 109
4.4. Comparison with spheres 111

5. CONCLUSIONS 117

REFERENCES.....119

LIST OF FIGURES

Page

Figure 1.1 The scattering particle. The particle (green patch) is surrounded in a volume indicated by the red dashed line. Circle with an infinity symbol marks the boundary at infinity. $m2r' = 1$ outside the particle.....8

Figure 1.2 Single scattering geometry. The green patch represents the scattering particle and is located at the coordinate origin. The scattering plane is the plane marked with the 2 orthogonal dashed lines. Scattering angle θ is indicated in the figure and ranges from 0 to 180 degrees.....9

Figure 2.1 PSTD computational domain. Left panel indicate our idea of truncating the actual infinite single scattering geometry to a finite box. Right panel shows the use of the absorbing layer to truncate the domain. 17

Figure 2.2 PSTD computation flowchart. 23

Figure 2.3 Time series of Ex component recorded at the six spots (red dots) on centers of the six Huygens surface. (Reprinted with permission from [16]) 24

Figure 2.4 2D simulation geometry. Color map shows the strength of the *Ez* field. In this case, the incident Gaussian pulse is coming into the computational domain from the top. White arrows indicate the strength and direction of the Poynting vectors. The number at the bottom indicates the time step. (Reprinted with permission from [16]).....27

Figure 2.5 Incident Gaussian pulse interacting with cylindrical crystal with circular cross-section. Time steps are indicated in the panels. (Reprinted with permission from [16]) 33

Figure 2.6 Time series of data gathered inside and outside and outside the circular cross section. The quantities shown are (a,e) pointwise maximum |Ez|; (b,f) total electromagnetic energy; (c,g) distance of pointwise maximum, with red line indicating particle boundary; and (d,h) Angle of the pointwise maximum. see text for details. (Reprinted with permission from [16]) 35

Figure 2.7 Tangential speed measurements of movements of |Ez| maxima. The speeds are normalized with vacuum light speed. See text for details. (Reprinted with permission from [16]).....36

Figure 2.8 As in Fig.2.5, but evolution of the Ez field around a particle with elliptical cross section. (Reprinted with permission from [16]) 39

Figure 2.9 As in Fig.2.6, but for an elliptical cross section. (Reprinted with permission from [16]) 41

Figure 2.10 Time series of surface curvature at point on interface of elliptical particle with same angle as nearby interior |Ez| maximum, and total electromagnetic energy, for two aspect ratios of the ellipse. In panels 2 and 4, the time series of the total energy for the circular cross section is included for comparison. (Reprinted with permission from [16]) 42

Figure 2.11 As in Fig.2.5 but showing the Ez field evolution of the hexagonal cross section. (Reprinted with permission from [16]) 46

Figure 2.12 As in Fig.2.9, but for a hexagonal cross section. (Reprinted with permission from [16]) 48

Figure 2.13 Comparison of time series of total internal electromagnetic energy for cases of circular cross section, two different elliptical cross sections (aspect ratio 0.5 and 0.75), and hexagonal cross section. (Reprinted with permission from [16]) 49

Figure 2.14 Angle-time diagram for (top row)circle, (middle row)ellipse and (bottom row)hexagonal cross sections: (a) at a fixed distance outside (b) total inside. See text for details. (Reprinted with permission from [16]) 50

Figure 3.1 Schematic of the radial recurrence. Particle in this schematic is an irregular hexahedron marked in green. It could be any non-spherical inhomogeneous particles. Coordinate origin is on the geometric center of the hexahedra. Two spherical shells are indicated in transparent grey color. Red dashed arrows indicate the two radii rp and $rp + 1$. 53

Figure 3.2 Comparison between II-TM and the Lorenz-Mie theory. Sphere is indicated in the figure, size parameter x=30 at incident wavelength 550nm, refractive index is 1.3. 73

Figure 3.3 Comparison between II-TM and the Lorenz-Mie theory. Sphere is indicated in the figure, size parameter x=30 at incident wavelength 550nm, refractive index is 1.3+i0.01. 74

Figure 3.4 Comparison between II-TM and the EBCM method. Spheroid is indicated in the figure, size parameter x=30 at incident wavelength 550nm, aspect ratio=0.5, refractive index is 1.3. 75

Figure 3.5 Comparison between II-TM and the EBCM method. Spheroid is indicated in the figure, size parameter x=30 at incident wavelength 550nm, aspect ratio=0.5, refractive index is 1.3+i0.01. 76

Figure 3.6 Comparison between II-TM and the PGOM method. Hexagonal column is indicated in the figure, size parameter x=225 defined with the circumscribing sphere radius. Refractive index m=1.308+i1.43 × 10 − 9. This corresponds to ice refractive index at 650 nm wavelength. 77

Figure 3.7 Comparison between II-TM and the PGOM method. Hexagonal column is indicated in the figure, size parameter x=225 defined with the circumscribing sphere radius. Refractive index m=1.276+i0.413. This corresponds to ice refractive index at 120 μm wavelength. 78

Figure 3.8 Progression of the spherical shell on a spheroid. In this case, $\theta 1 = 0$. and $\theta 2$ is the angle where the spherical shell intersects the spheroid. 81

Figure 3.9 Progression of the spherical shell on a long hexagonal column. 83

Figure 3.10 An example $Fmm'\ \ r, \theta$ as a function of θ. 84

Figure 3.11 $f1x$ and $f2x$ 86

Figure 3.12 Convergence rate of the code outputs ($Qext, g, P11180o$) with respect to the number of quadrature nodes Nq. Each row has different aspect ratios, 3 panels in each row has different size parameters indicated in the top-left corner of each panel. 90

Figure 3.14 Convergence rate of the code outputs($Qext, g, P11180o$) with respect to number of quadrature nodes Nq as in Fig.3.12. Unlike Fig.3.12, the integration range is split into 2 smooth intervals, so the convergence rate is accelerated (see text). 94

Figure 4.1 The 20-shapes ensemble. 4 rows from top to bottom were constructed with $\sigma 2$=0.3,0.4,0.5,1.0, respectively. 106

Figure 4.2 Individual phase matrix elements(green) against their ensemble averaged values. The average(red) is in between the individual lines. 107

Figure 4.3 Parameter space of the dataset. 108

Figure 4.4 Phase matrix elements of ocean particles at incident wavelength 658 nm, particle refractive index 1.02+i0.0005, and particle equivalent-volume-sphere radius 2.0 μm. 109

Figure 4.5 (a)Beam tracing in a faceted particle. (b)Schematic of reflection and refraction event at an interface of changing refractive index. 111

Figure 4.6 Qext, Qsca, SSA (single scattering albedo) and asymmetry factor as functions of particle size. Refractive index=1.18+i0.0005.....112

Figure 4.7 Normalized VSF of a sphere (red line) and hexahedra ensemble (blue dotted). Two refractive indices are indicated in the titles. The integration size range [0.1um,70um] is used in the computation of VSF. In this case, our hexahedral model produces much higher backscattering than the spherical model.....115

Figure 4.8 Normalized VSF of sphere (red line) and hexahedra ensemble (blue dotted). Two refractive indices are indicated in the titles. The integration size range [1um,70um] is used in the computation of VSF. In this case, our hexahedral model produces lower backscattering than the spherical model..116

LIST OF TABLES

Page

Table 3.1 Convergence rate of Gaussian quadrature for 2 different integrands in Fig.3.10. “RE” indicates the relative error which is given by the ratio of the difference between the quadrature and integral over the integral, or $RE = estimate - exactexact.$ 87

Table 3.2 CPU time required to run the same code section (integrate $f1x = 1, 0 \leq x \leq 0.521 - x, 0.5 < x \leq 1$) with Newton and Bogaert algorithms. 96

Table 3.3 Acceleration for hexagonal columns and spheroids of various sizes and aspect ratios. 97

Table 4.1 Categorization of different phytoplankton based on their sizes along with examples of those phytoplankton. 102

1. INTRODUCTION

Based on fundamental physical theories (Maxwell's Equations), the theory of radiative transfer describes the radiance field in an absorbing medium with scattering objects. Conceptually, the path from fundamental physics to radiative transfer theory involves the following stages, with increasing applicable length scale:

1.Quantum electrodynamics

2.Maxwell's Equations

3.The vector radiative transfer equation

Quantum electrodynamics (QED) is the fundamental theory which explains with complete accuracy the interactions of light and matter [1]. In that theory, the electromagnetic field is quantized with photons, and electromagnetism is described at the level of individual photons. QED is a conceptual starting point for much of modern physics.

At the "classical physics limit" of QED, the electromagnetic field is no longer quantized. Applying classical field theory gives the four Maxwell's equations. Maxwell's equations describe the electric and magnetic fields as continuous functions of space and time. The Maxwell's differential equations in SI units [2],

$$\nabla \cdot \vec{E} = \frac{\rho}{\epsilon_0} \tag{1.1}$$

$$\nabla \cdot \vec{B} = 0 \tag{1.2}$$

$$\nabla \times \vec{E} = -\frac{\partial \vec{B}}{\partial \mathrm{t}} \tag{1.3}$$

$$\nabla \times \vec{B} = -\mu_0 \vec{j} + \mu_0 \epsilon_0 \frac{\partial \vec{E}}{\partial \mathrm{t}} \tag{1.4}$$

$\vec{E}$ is the electric field, $\vec{B}$ is the magnetic field, ρ is the electric charge density, $\vec{j}$ is the electric current density. ϵ_0 is the electric permittivity of free space, μ_0 is the magnetic permeability in free space. In a material medium, the Maxwell's equations become more complicated, but the general form remains the same. Maxwell's equations written in this form are linear in nature and the resulting electromagnetic fields can be superposed.

In the frequency domain, the time averaged electric field can be given by the complex amplitude $\overrightarrow{E_0}(\vec{r})$ of a monochromatic plane electromagnetic wave $\vec{E}(\vec{r}) = \overrightarrow{E_0}(\vec{r})e^{i(\vec{k}\vec{r}-\omega t)}$. The wavenumber vector $\vec{k}$ is in the direction of propagation and ω is the frequency. In the reference plane which is perpendicular to the propagation direction, the complex amplitude $\overrightarrow{E_0}(\vec{r})$ can be decomposed into orthogonal components $E_{\parallel}$ and $E_{\perp}$ with respect to the two conventionally chosen orthogonal vectors $\hat{e}_0^{\perp}$ and $\hat{e}_0^{\parallel}$ (as discussed later in Sec.1.1, Fig.1.2).

The Stokes vector gives the state of polarization along with the intensity of the light field

$$\begin{pmatrix} I \\ Q \\ U \\ V \end{pmatrix} = \frac{1}{2}\sqrt{\frac{\epsilon}{\mu}} \begin{pmatrix} E_{\parallel}\ E_{\parallel}^{*} + E_{\perp}\ E_{\perp}^{*} \\ E_{\parallel}\ E_{\parallel}^{*} - E_{\perp}\ E_{\perp}^{*} \\ E_{\parallel}\ E_{\perp}^{*} + E_{\perp}\ E_{\parallel}^{*} \\ i\left(E_{\parallel}\ E_{\perp}^{*} - E_{\perp}\ E_{\parallel}^{*}\right) \end{pmatrix}. \tag{1.5}$$

where ϵ is the electric permittivity of the medium and μ is the magnetic permeability of the medium. Each element has the units of irradiance (W/m^2). I indicates the intensity, Q indicates the degree of linear polarization, U indicates the degree of linear polarization with respect to the directional vector 45 degrees away from $\hat{e}_0^{\parallel}$ and V indicates the degree of circular polarization.

Switching from the instantaneous electromagnetic field in time domain to the Stokes vector in frequency domain, a 3D vector radiative transfer equation (VRTE) can be obtained. $\vec{S}(\vec{x},\hat{r})$ is the Stokes vector at spatial position $\vec{x}$ with propagation direction $\hat{r}$

$$\vec{S}(\vec{x},\hat{r}) = \begin{pmatrix} I(\vec{x},\hat{r}) \\ Q(\vec{x},\hat{r}) \\ U(\vec{x},\hat{r}) \\ V(\vec{x},\hat{r}) \end{pmatrix} = \hat{r}\begin{pmatrix} I(\vec{x}) \\ Q(\vec{x}) \\ U(\vec{x}) \\ V(\vec{x}) \end{pmatrix} = \hat{r}\vec{S}(\vec{x}), \tag{1.6}$$

the VRTE has the form [3] (omitting the inelastic scattering term):

$$\hat{r}\cdot\nabla\vec{S}(\vec{x},\hat{r}) = -\bar{\bar{K}}(\vec{x},\hat{r})\vec{S}(\vec{x},\hat{r}) + \int_{4\pi} d^2\hat{r}'\,\bar{\bar{Z}}(\vec{x};\hat{r}',\hat{r})\vec{S}(\vec{x},\hat{r}') \tag{1.7}$$

$\overline{\overline{K}}(\vec{x},\hat{r})$ is the 4×4 extinction matrix. This matrix describes the attenuation by the background medium and any particles immersed in the medium. $\overline{\overline{Z}}(\vec{x};\hat{r}',\hat{r})$ is the phase matrix, which describes the transformation of the incident light direction and polarization to the scattered direction and polarization. Note that $\overline{\overline{K}}$ and $\overline{\overline{Z}}$ are the bulk extinction and scattering matrices for a volume containing a number of particles. Eq.1.7 can describe polarized light propagation in a medium that is non-isotropic, and that contains scattering particles with random or fixed orientations [3].

$\overline{\overline{K}}$ and $\overline{\overline{Z}}$ require the single scattering properties of those immersed particles. Since the distances between the scattering particles are large enough in the atmosphere and oceans, the single scattering approximation can be applied, where the incident light on each particle is purely composed of sunlight (not containing scattered waves from other particles). Thus, the single scattering simulation of individual particles is separated from the radiative transfer calculation and can be treated accurately by solving the Maxwell's equations with boundary conditions at infinity. Conceptually, the computational domain of a single scattering simulation is a single particle (of any shape, composition and internal structure) situated in a background medium. The incident plane wave comes, and we solve for the electromagnetic field with respect to this particle and the boundary condition at infinity (scattered wave radiating to infinity). Thus, the current forward radiative transfer problem can be seen as a "multiscale" problem where the single scattering properties of small particles obtained from solving the Maxwell's equations serve as input to the radiative transfer equation with a larger length scale, and

the conceptual “infinitely small volume” contains a large number of single scattering particles.

The problem of single scattering is a classic mathematical-physics problem. For a spherical particle shape, the method of separation of variables can be applied to Maxwell’s equations in the frequency domain [4]. Naturally, the basis functions in spherical coordinates are used (spherical Bessel functions and spherical harmonics). The linear transformation between the expansion coefficients of the incident and scattered waves contains all of the single scattering properties and is used to compute the corresponding extinction and scattering matrices. For spheroids, a similar approach was attempted [5]. Separation of variables was carried out in spheroidal coordinates, and spheroidal basis functions are used.

For non-spherical and inhomogeneous particles, separation of variables does not work so a proper discretization scheme must be used based on the particle shape. For particles possessing certain rotational symmetry or mirror symmetries, the Transition Matrix (T-matrix) method is the most efficient. Mathematically speaking, the T-matrix is the linear transformation between the expansion coefficients of the scattered wave and the incident wave. All information of a particle’s single scattering properties are contained in the T-matrix. Classical T-matrix solution schemes include the Extended Boundary Condition Method (EBCM) where the T-matrix is obtained through a direct matrix inversion resulting from a surface integral equation for the electric field surrounding the particle[6]. EBCM is very efficient for spheroids, bodies of revolution and Chebyshev particles. The invariant imbedding method has been applied to a volume

integral equation to generate an iterative formula for the T-matrix of the particle [7][8]. The resulting solution scheme is named the invariant-imbedding T-matrix (II-TM) method and this scheme is also efficient for particles with symmetry.

For irregular particles possessing no symmetries, various discretizing schemes have been applied. One most widely used and the easiest to understand is the finite-difference method [9][10]. The finite difference scheme is applied to Maxwell's differential equations. The discrete dipole approximation is applied to a volume integral equation for the electric field inside the particle [11]. The pseudo-spectral method is used on the spatial derivatives in the discretized Maxwell's equations, and the resulting scheme is called the pseudo-spectral time domain (PSTD) method [12]. PSTD is an improved version of the finite difference time domain (FDTD) method [10].

This dissertation will focus on the aforementioned II-TM and PSTD methods. Specifically, we improve the performance of the Gaussian quadrature in the II-TM method by implementing a new node and weight generating algorithm [13]. Modifications are also made to avoid quadrature over discontinuities in certain particle shape.

Finally, a marine hydrosol dataset is computed and compiled. The main feature of the dataset is the particle shapes. A random hexahedral ensemble is used. The II-TM method mentioned above is used to compute properties of particles on the smaller end of the size spectrum. The physical geometric optics method (PGOM) [14] is used to compute properties of large particles. Single particle optical properties are obtained by

averaging over the ensemble. Comparisons between the hexahedra ensemble dataset and spherical dataset are made.

1.1. Single scattering

Consider a time harmonic electric field at a single frequency ω

$$\vec{E}(\vec{r}) = \overrightarrow{E_0}(\vec{r}, \omega)e^{i(\vec{k}\vec{r}-\omega t)}, \tag{1.8}$$

the amplitude of the wavenumber vector k is defined by $k = \frac{2\pi}{\lambda}$ with λ being the wavelength. The volume integral equation with the electric field $\vec{E}(\vec{r}, \omega)$ (omitting subscript 0) at a certain frequency ω [2] is

$$\vec{E}(\vec{r}) = \overrightarrow{E_{inc}}(\vec{r}) + k^2 \iiint_V d^3\overrightarrow{r'} \left[m^2\left(\overrightarrow{r'}\right) - 1\right] \left(\bar{\bar{I}} + \frac{1}{k^2}\nabla'\nabla'\right) \frac{e^{ik\left|\vec{r}-\overrightarrow{r'}\right|}}{4\pi\left|\vec{r}-\overrightarrow{r'}\right|} \cdot \vec{E}\left(\overrightarrow{r'}\right), \tag{1.9}$$

where $\vec{E}(\vec{r})$ is the total electric field and $\overrightarrow{E_{inc}}(\vec{r})$ is the incident field. The volume V encloses the scattering particle, $m^2\left(\overrightarrow{r'}\right) = 1$ outside the particle (Fig.1.1). This equation describes the electric field with respect to the Somerfield radiation condition at infinity (scattered field radiating to infinity) and a certain scattering particle geometry $m^2\left(\overrightarrow{r'}\right)$.

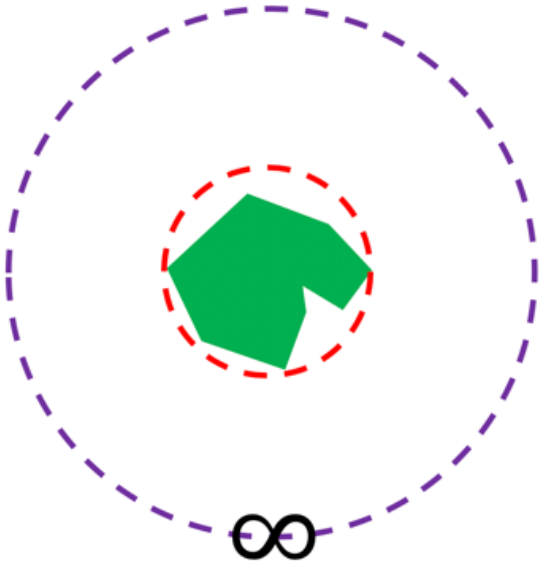

Figure 1.1 The scattering particle. The particle (green patch) is surrounded in a volume indicated by the red dashed line. Circle with an infinity symbol marks the boundary at infinity. $m^2(\vec{r'}) = 1$ outside the particle.

The particle size parameter is defined as

$$x = \frac{2\pi d}{\lambda}, \tag{1.10}$$

where d is either the equivalent-volume-sphere radius or the radius of the circumscribing sphere. Eq. (1.9) is the fundamental equation to be solved in the PSTD and II-TM method to obtain the far field properties of the scattering particle.

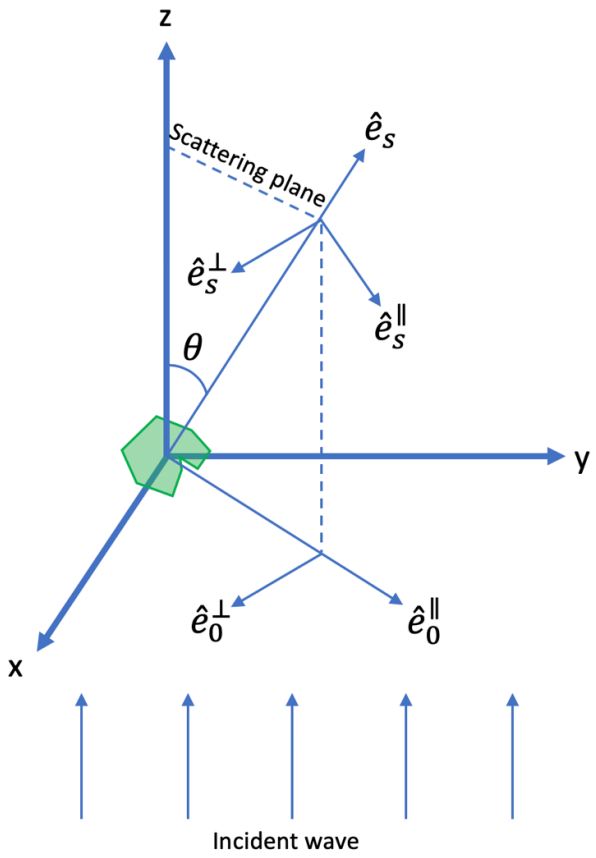

Figure 1.2 Single scattering geometry. The green patch represents the scattering particle and is located at the coordinate origin. The scattering plane is the plane marked with the 2 orthogonal dashed lines. Scattering angle θ is indicated in the figure and ranges from 0 to 180 degrees.

The incident wave can be expanded into components with respect to $\hat{e}_0^{\perp}$ and $\hat{e}_0^{\parallel}$ (Fig.1.2) ,$\overrightarrow{E_{inc}} = \hat{e}_0^{\parallel} E_{inc}^{||} + \hat{e}_0^{\perp} E_{inc}^{\perp}$. Similarly, for the scattered wave that are sufficiently far away from the particle ($kr \rightarrow \infty$), $\overrightarrow{E_s} = \hat{e}_s^{\parallel} E_s^{||} + \hat{e}_s^{\perp} E_s^{\perp}$. With respect to the scattering plane,

the scattered far field can be related to the incident field through a rotation matrix called the amplitude scattering matrix [15],

$$\begin{pmatrix} E_s^{\parallel}(\vec{r}) \\ E_s^{\perp}(\vec{r}) \end{pmatrix}\Bigg|_{kr \to \infty} = \frac{e^{ikr}}{-ikr}\begin{pmatrix} s_2 & s_3 \\ s_4 & s_1 \end{pmatrix}\begin{pmatrix} E_{inc}^{||} \\ E_{inc}^{\perp} \end{pmatrix} \tag{1.11}$$

The amplitude scattering matrix indicates the angular distribution of scattered energy around the particles where k is the wavenumber and r is the distance between the scattering particle and the observation point. The four elements of the Stokes vector describe both the amplitude and polarization state of the electric field, Far-field physical properties of interest can all be obtained with this matrix.

$$\begin{pmatrix} I \\ Q \\ U \\ V \end{pmatrix} = \frac{1}{2}\sqrt{\frac{\epsilon}{\mu}}\begin{pmatrix} E_{\parallel}\ E_{\parallel}^* + E_{\perp}\ E_{\perp}^* \\ E_{\parallel}\ E_{\parallel}^* - E_{\perp}\ E_{\perp}^* \\ E_{\parallel}\ E_{\perp}^* + E_{\perp}\ E_{\parallel}^* \\ i\left(E_{\parallel}\ E_{\perp}^* - E_{\perp}\ E_{\parallel}^*\right) \end{pmatrix} \tag{1.12}$$

The linear transformation between the Stokes vectors of incident and scattered fields is the 4× 4 Mueller matrix,

$$\vec{S}_{sca} = \begin{pmatrix} I_{sca} \\ Q_{sca} \\ U_{sca} \\ V_{sca} \end{pmatrix} = (\frac{1}{kr})^2 \begin{pmatrix} S_{11} & S_{12} & S_{13} & S_{14} \\ S_{21} & S_{22} & S_{23} & S_{24} \\ S_{31} & S_{32} & S_{33} & S_{34} \\ S_{41} & S_{42} & S_{43} & S_{44} \end{pmatrix} \begin{pmatrix} I_{inc} \\ Q_{inc} \\ U_{inc} \\ V_{inc} \end{pmatrix}$$
$$= (\frac{1}{kr})^2 \begin{pmatrix} S_{11} & S_{12} & S_{13} & S_{14} \\ S_{21} & S_{22} & S_{23} & S_{24} \\ S_{31} & S_{32} & S_{33} & S_{34} \\ S_{41} & S_{42} & S_{43} & S_{44} \end{pmatrix} \vec{S}_{inc} \tag{1.13}$$

The 16 Mueller matrix elements can be written as combinations of amplitude scattering matrix elements. We only list a few here:

$$\mathrm{S}_{11} = \frac{1}{2}(|s_1|^2 + |s_2|^2 + |s_3|^2 + |s_4|^2) \tag{1.14}$$

$$\mathrm{S}_{12} = \frac{1}{2}(|s_2|^2 - |s_1|^2 + |s_4|^2 - |s_3|^2) \tag{1.15}$$

$$\mathrm{S}_{22} = \frac{1}{2}(|s_1|^2 + |s_2|^2 - |s_3|^2 - |s_4|^2) \tag{1.16}$$

$$\mathrm{S}_{33} = \mathrm{Re}(s_2^* s_1 + s_3 s_4^*) \tag{1.17}$$

Using the Optical Theorem [15], the extinction cross section C_{ext} can be written in terms of the amplitude scattering matrix and the incident Stokes vector as

$$C_{ext} = \frac{2\pi}{k^2} Re \left\{ [s_1(0) + s_2(0)] + [s_2(0) - s_1(0)] \frac{Q_{inc}}{I_{inc}} + [s_3(0) - s_4(0)] \frac{U_{inc}}{I_{inc}} + [s_3(0) - s_4(0)] \frac{V_{inc}}{I_{inc}} \right\} \tag{1.18}$$

The scattering cross section is given by,

$$C_{sca} = \frac{1}{k^2} \iint_{4\pi} d^2\Omega S_{11} \tag{1.19}$$

Due to energy conservation, the absorption cross section C_{abp} is

$$C_{abp} = C_{ext} - C_{sca} \tag{1.20}$$

The single scattering albedo (SSA) is defined as,

$$\text{SSA} = \frac{C_{sca}}{C_{ext}} \tag{1.21}$$

With respect to the particle's projected cross-sectional area C_{proj}, the extinction, scattering and absorption efficiencies are,

$$Q_{ext} = \frac{C_{ext}}{C_{proj}}, Q_{sca} = \frac{C_{sca}}{C_{proj}}, Q_{abp} = \frac{C_{abp}}{C_{proj}} \tag{1.22}$$

the scattering function $f(\theta)$ is defined as,

$$f(\theta) = S_{11} + S_{12}\frac{Q_{inc}}{I_{inc}} + S_{13}\frac{U_{inc}}{I_{inc}} + S_{14}\frac{V_{inc}}{I_{inc}} \tag{1.23}$$

The scalar phase function $p(\theta)$ is defined as,

$$p(\theta) = \frac{f(\theta)}{k^2 C_{sca}} \tag{1.24}$$

The phase function gives the relative distribution of scattered radiation with respect to scattering angle θ. The asymmetry factor g is defined as [15],

$$g = \iint_{4\pi} p(\theta) cos\theta \, d^2\Omega \tag{1.25}$$

The asymmetry factor is a rough indication of the characteristics of the angular distribution of scattered energy where $g = -1$ indicates pure backward scattering, $g = 1$ indicates pure forward scattering, and $g = 0$ means that the scattered energy is evenly distributed across the 4π steradian.

2. THE PSEUDO SPECTRAL TIME DOMAIN METHOD*

The pseudo spectral time domain (PSTD) method has its origin in the finite difference time domain (FDTD) method [10]. The FDTD uses a finite difference scheme to discretize the spatial derivative in time domain Maxwell's Equations. In the near field computational domain of PSTD and FDTD, the field smoothly decays to 0 in the absorbing boundary layer. Due to this periodicity, a pair of Fast Fourier Transforms (FFT) can be used to calculate the spatial derivative in Maxwell's Equation.

The collected time domain data from the near field is Fourier transformed to the frequency domain for computation of far field single scattering properties. For smooth fields, the pseudo spectral method is very efficient, and requires only several grid points per wavelength in the computational domain. In this dissertation, we conduct 2-D simulations to investigate how the time domain near field decays inside the PSTD computational domain. The decay time affects the elapsed computational time of the near field time stepping which in turn affects the total computational time of the method.

2.1. Pseudo-spectral time domain (PSTD) method

For the far field, r ≫ λ, r ≫ r' the Green Function can be simplified, and Eq.(1.9) reduces to [10],

$$\overrightarrow{E_s}(\vec{r})\Big|_{kr\to\infty} = \frac{k^2 e^{ikr}}{4\pi r}\iiint_V d^3\overrightarrow{r'}\left[m^2\left(\overrightarrow{r'}\right)-1\right]e^{-ik\hat{r}\cdot\overrightarrow{r'}}\left\{\vec{E}\left(\overrightarrow{r'}\right) - \hat{r}\left[\hat{r}\cdot\vec{E}\left(\overrightarrow{r'}\right)\right]\right\}, \tag{2.1}$$

where $\hat{r} = \frac{\vec{r}}{r}$. Writing the scattered field in components with respect to $\hat{e}_s^{\parallel}$ and $\hat{e}_s^{\perp}$, using Eq. (1.11), we have,

$$\begin{pmatrix} E_s^{\parallel}(\vec{r}) \\ E_s^{\perp}(\vec{r}) \end{pmatrix}\Big|_{kr\to\infty} = \frac{k^2 e^{ikr}}{4\pi r}\iiint_V d^3\overrightarrow{r'}\left[m^2\left(\overrightarrow{r'}\right)-1\right]e^{-ik\hat{r}\cdot\overrightarrow{r'}}\begin{pmatrix}\vec{E}\left(\overrightarrow{r'}\right)\cdot\hat{e}_s^{\parallel} \\ \vec{E}\left(\overrightarrow{r'}\right)\cdot\hat{e}_s^{\perp}\end{pmatrix} \tag{2.2}$$

$$= \frac{e^{ikr}}{-ikr}\begin{pmatrix} s_2 & s_3 \\ s_4 & s_1\end{pmatrix}\begin{pmatrix} E_{inc}^{||} \\ E_{inc}^{\perp}\end{pmatrix},$$

To obtain the amplitude scattering matrix, two different incident polarizations are needed, and we have,

$$\frac{-ik^3}{4\pi}\iiint_V d^3\overrightarrow{r'}\left[m^2\left(\overrightarrow{r'}\right)-1\right]e^{-ik\hat{r}\cdot\overrightarrow{r'}}\begin{pmatrix}\vec{E}\left(\overrightarrow{r'}\right)\cdot\hat{e}_s^{\parallel}\\ \vec{E}\left(\overrightarrow{r'}\right)\cdot\hat{e}_s^{\perp}\end{pmatrix}\Bigg|_{\substack{E_0^{\parallel}=1\\ E_0^{\perp}=0}}=\begin{pmatrix}S_2\\ S_4\end{pmatrix}, \tag{2.3}$$

$$\frac{-ik^3}{4\pi}\iiint_V d^3\overrightarrow{r'}\left[m^2\left(\overrightarrow{r'}\right)-1\right]e^{-ik\hat{r}\cdot\overrightarrow{r'}}\begin{pmatrix}\vec{E}\left(\overrightarrow{r'}\right)\cdot\hat{e}_s^{\parallel}\\ \vec{E}\left(\overrightarrow{r'}\right)\cdot\hat{e}_s^{\perp}\end{pmatrix}\Bigg|_{\substack{E_0^{\parallel}=0\\ E_0^{\perp}=1}}=\begin{pmatrix}S_3\\ S_1\end{pmatrix}, \tag{2.4}$$

Now we need to obtain the electric field in V at a certain frequency $\vec{E}\left(\overrightarrow{r'},\omega\right)$. It is achieved by collecting time domain data $\vec{E}\left(\overrightarrow{r'},\mathrm{t}\right)$ and then perform a discrete Fourier Transform back to the frequency domain,

$$F(\overrightarrow{r'},\omega)=\frac{1}{N}\sum_{n=1}^{N}f(\overrightarrow{r'},n)\,e^{-i\,\omega\mathrm{n}\Delta\mathrm{t}}, \tag{2.5}$$

Where f and F represent any of the components of $\vec{E}$. Time domain data $\vec{E}\left(\overrightarrow{r'},\mathrm{t}\right)$ is obtained through time-stepping the Maxwell's Equation. The Pseudo-Spectral Time Domain (PSTD) method is developed to carry out the aforementioned procedures to obtain the single scattering properties of non-spherical and inhomogeneous particles.

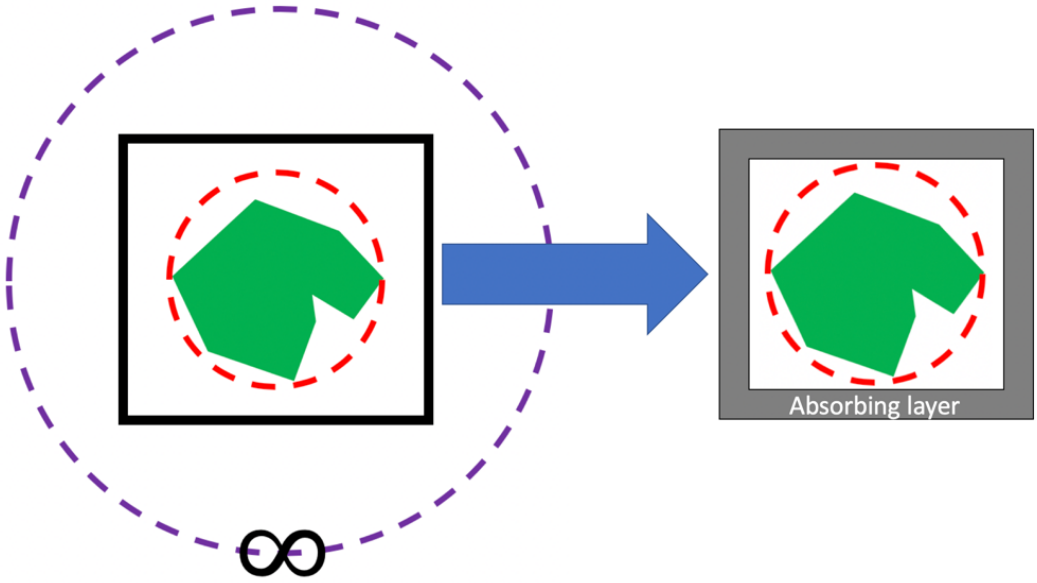

Figure 2.1 PSTD computational domain. Left panel indicate our idea of truncating the actual infinite single scattering geometry to a finite box. Right panel shows the use of the absorbing layer to truncate the domain.

The near field computational domain is truncated with an absorbing layer (Fig.2.1). The absorbing layer absorbs any incoming wave and is used to satisfy the boundary condition that the scattered wave radiates to infinity. Macroscopic Maxwell's Equations (in Gaussian units) are solved inside the absorbing layer [12],

$$\frac{\epsilon(\vec{r})}{c}\frac{\partial \vec{E}(\vec{r},t)}{\partial t} = \nabla \times \vec{H}(\vec{r},t) \tag{2.6}$$

$$\frac{1}{c}\frac{\partial \vec{H}(\vec{r},t)}{\partial t} = -\nabla \times \vec{E}(\vec{r},t) \tag{2.7}$$

c is light speed in vacuum, separate the incident and scattered electromagnetic fields as follows:

$$\vec{E} = \vec{E}_{inc} + \vec{E}_s, \;\; \vec{H} = \vec{H}_{inc} + \vec{H}_s \tag{2.8}$$

the permittivity has real and imaginary parts,

$$\epsilon = \epsilon_r + i\epsilon_i \tag{2.9}$$

plugging Eqs.2.8 and 2.9 into Eq.2.6 and 2.7, we have,

$$\frac{\partial \vec{E}_s}{\partial t} = \frac{c}{\epsilon_r}\nabla \times \vec{H}_s - \omega\frac{\epsilon_i}{\epsilon_r}\vec{E}_s + \vec{f}_{inc} \tag{2.10}$$

$$\frac{\partial \vec{H}_s}{\partial t} = -c\nabla \times \vec{E}_s \tag{2.11}$$

and

$$\vec{f}_{inc} = \left[\left(\frac{1-\epsilon_r}{\epsilon_r}\right)\frac{\partial}{\partial t} - \omega\frac{\omega_i}{\omega_r}\right]\vec{E}_{inc} \tag{2.12}$$

At each time step, $\vec{f}_0$ is given analytically, so the right hand side of Eq.2.10 involves only spatial derivatives. Write all fields in discrete time and space as follows:

$$U^n(i,j,k) = U(n\Delta t, i\Delta x, j\Delta y, k\Delta z) \tag{2.13}$$

where superscript *n* indicates time step. Eq.2.10 and 2.11 become,

$$\frac{\partial \vec{E}_s^n(i,j,k)}{\partial t} = \frac{c}{\epsilon_r}\nabla \times \vec{H}_s^n(i,j,k) - \omega\frac{\epsilon_i}{\epsilon_r}\vec{E}_s^n(i,j,k) + \vec{f}_{inc}(n,i,j,k) \tag{2.14}$$

$$\frac{\partial \vec{H}_s^{n+\frac{1}{2}}(i,j,k)}{\partial t} = -c\nabla \times \vec{E}_s^{n+\frac{1}{2}}(i,j,k) \tag{2.15}$$

Using a 2nd order finite difference in time, the time derivative has the following form:

$$\frac{\partial \vec{E}_s^n(i,j,k)}{\partial t} \sim \frac{\vec{E}_s^{n+\frac{1}{2}}(i,j,k) - \vec{E}_s^{n-\frac{1}{2}}(i,j,k)}{\Delta t} \tag{2.16}$$

And using the following approximation,

$$\vec{E}_s^n(i,j,k) \sim \frac{\vec{E}_s^{n+\frac{1}{2}}(i,j,k) - \vec{E}_s^{n-\frac{1}{2}}(i,j,k)}{2} \tag{2.17}$$

Eqs.2.14 and 2.15 become,

$$\vec{E}_s^{n+\frac{1}{2}}(i,j,k) = a_1(i,j,k)\nabla \times \vec{H}_s^n(i,j,k) + a_2(i,j,k)\vec{E}_s^{n-\frac{1}{2}}(i,j,k) + a_3(i,j,k)\frac{\partial}{\partial t}\vec{E}_0^n(i,j,k) + a_4(i,j,k)\vec{E}_0^n(i,j,k) \tag{2.18}$$

$$\vec{H}_s^{n+1}(i,j,k) = \vec{H}_s^n(i,j,k) - c\Delta t\nabla \times \vec{E}_s^{n+\frac{1}{2}}(i,j,k) \tag{2.19}$$

where

$$\begin{aligned} a_1(i,j,k) &= \frac{2c\Delta t}{2\epsilon_r(i,j,k) + kc\Delta t\epsilon_i(i,j,k)} \\ a_2(i,j,k) &= \frac{2\epsilon_r(i,j,k) - kc\Delta t\epsilon_i(i,j,k)}{2\epsilon_r(i,j,k) + kc\Delta t\epsilon_i(i,j,k)} \\ a_3(i,j,k) &= \frac{2(1-\epsilon_r(i,j,k))\Delta t}{2\epsilon_r(i,j,k) + kc\Delta t\epsilon_i(i,j,k)} \\ a_4(i,j,k) &= -\frac{2kc\Delta t\epsilon_r(i,j,k)}{2\epsilon_r(i,j,k) + kc\Delta t\epsilon_i(i,j,k)} \end{aligned} \tag{2.20}$$

We can choose any form of incident wave $\vec{E}_{inc}(\vec{r},t)$. In our numerical simulations, a plane wave with a Gaussian envelope is used,

$$\begin{aligned} \vec{E}_{inc}(\vec{r},t) &= \vec{E}_{inc}\left(\vec{k}\cdot\vec{r} - \omega t\right) \\ &= E_0\cos\left(\vec{k}\cdot\vec{r} - \omega t\right)exp\left[-\left(\frac{\vec{k}\cdot\vec{r} - \omega t - \sigma_0}{4\pi}\right)^2\right] \end{aligned} \tag{2.21}$$

σ_0 is the initial phase of the pulse, it is so chosen that the pulse has negligibly small amplitude at the start of the simulation.

In the pseudo-spectral method that we discuss here, we write the interpolant of a function *u(x)* in the form of a discrete inverse Fourier transform,

$$U(x) = \sum_{k=-\frac{N}{2}}^{\frac{N}{2}-1} \widetilde{U}_k \, e^{i\hat{k}x} \tag{2.22}$$

where $\hat{k} = \frac{2\pi}{L} k$ is the scaled wavenumber. L is the length of the computational domain (including the absorbing layer in Fig.2.1). The coefficients are given by the discrete Fourier transform,

$$\widetilde{U}_k = \frac{1}{N} \sum_{j=1}^{N} u(x_j) \, e^{-i\hat{k}x_j}, \;\; k \in [-\frac{N}{2}, \frac{N}{2} - 1] \tag{2.23}$$

Note that these discrete Fourier transforms can be efficiently computed with the Fast Fourier Transform (FFT). The derivative of u(x) can be written as,

$$\frac{d}{dx}U(x) = \sum_{k=-\frac{N}{2}}^{\frac{N}{2}-1} i\hat{k}\widetilde{U}_k\, e^{i\hat{k}x} = \sum_{k=-\frac{N}{2}}^{\frac{N}{2}-1} i\hat{k}\frac{1}{N}\sum_{j=1}^{N} u(x_j)\, e^{-i\hat{k}x_j}\, e^{i\hat{k}x} \tag{2.24}$$

$$= IFFT\left[i\widehat{\boldsymbol{k}} \cdot [FFT(\boldsymbol{u})]\right]$$

where *IFFT* indicates inverse fast Fourier transform, and,

$$\widehat{\boldsymbol{k}} = \frac{2\pi}{L}\left[-\frac{N}{2}, -\frac{N}{2}+1, \dots, \frac{N}{2}-1\right] \tag{2.25}$$

$$\boldsymbol{u} = [u(1), u(2), \dots, u(N)]^T \tag{2.26}$$

Note that the maximum wavenumber k=$\frac{N}{2}$ is associated with the number of grid points. A finer grid can describe a smaller scale oscillation using the spectral method. When function $u(x)$ is smooth, Eq.2.24 converges to the exact value rapidly meaning that N is small. When function $u(x)$ contains discontinuities in itself or its higher order derivatives, Eq.2.24 converges slowly (meaning that a large N is required). Spectral filters were implemented into the PSTD method to mitigate the Gibbs phenomenon when the field is oscillatory or discontinuous [12].

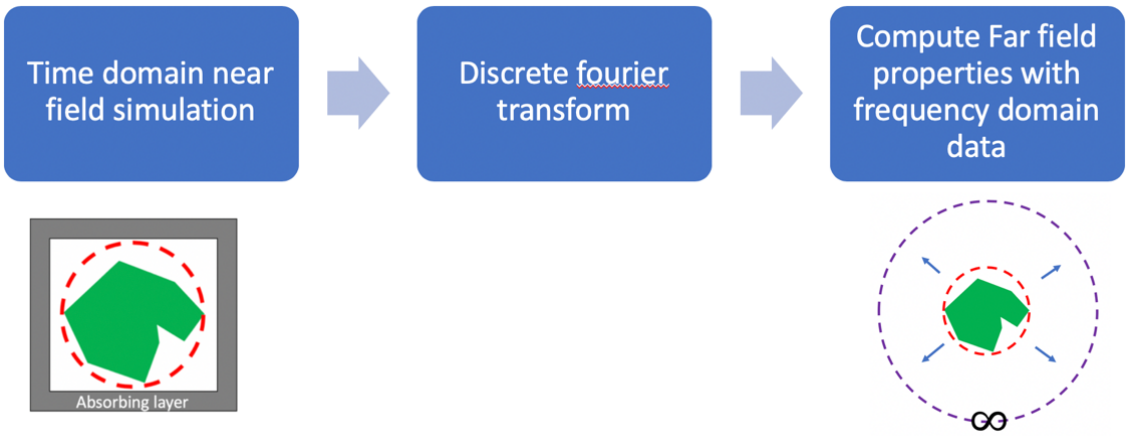

Figure 2.2 PSTD computation flowchart.

The simulation time in the time domain is controlled by *N* in Eq.2.5,

$$F(\vec{r'},\omega) = \frac{1}{N}\sum_{n=1}^{N} f(\vec{r'},n)\, e^{-i\,\omega n\Delta t} = \frac{1}{N}\sum_{n=1}^{N-1} f(\vec{r'},n)\, e^{-i\,\omega n\Delta t} + \frac{1}{N} f(\vec{r'},N) e^{-i\,\omega N\Delta t}. \tag{2.27}$$

In general when $f(\vec{r'},N) < 10^{-10}$, we can safely terminate the simulation in the time domain since the contribution from further simulations will be negligible. However, in most situations, the decay of the electric field in the near field of the particle is not monotonic, and it depends on the structure of the particle. For example, Fig.2.3 shows the time series of the *Ex* component at six spots on the Huygens surface in the case of a sphere in the PSTD computational domain. In the case of a sphere, the time series is filled with semi-periodic pulses. The presence of such pulses causes a challenge in

predicting the simulation length. It can be imagined the signal will be even more irregular for complex particle shapes.

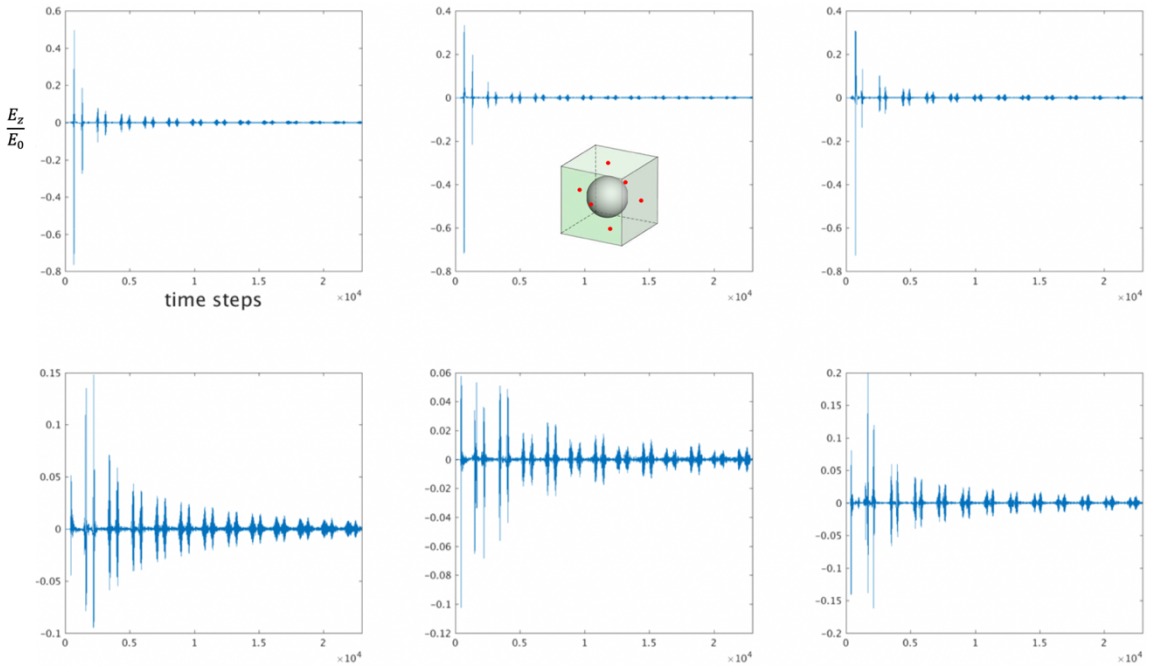

Figure 2.3 Time series of Ex component recorded at the six spots (red dots) on centers of the six Huygens surface. (Reprinted with permission from [16]**)**

2.2. 2-dimensional PSTD simulations to understand the near field behavior

For simplicity we first look at 2-dimensional simulations. The two-dimensional problem here is a cylindrical particle (of various cross-section) illuminated by an incident wave or wave packet approaching at an angle normal to the cylinder axis. The Transverse Electric (TE) case is considered here, in which the incident field is polarized parallel to the cylinder axis, and the model equations are [16],

$$\frac{\epsilon}{c}\frac{\partial \vec{E}}{\partial t} = \nabla \times \vec{H} \tag{2.28}$$

$$\frac{1}{c}\frac{\partial \vec{H}}{\partial t} = -\nabla \times \vec{E} \tag{2.29}$$

$$\vec{E} = E_z\hat{z}, \;\; \vec{H} = H_x\hat{x} + H_y\hat{y} \tag{2.30}$$

The particle shape (cross section) is described by the spatial dependence of the permittivity, $\epsilon = \epsilon(x, y)$. In this study, we consider cases of circular, elliptical, and hexagonal shapes. The incident wave has central wavelength $0.55\mu m$ and the particle refractive index m=1.3.

First, we present a circular cross-sectional shape with size parameter x=30. The size parameter is defined as in Eq.1.10 with r being the circle radius. In Fig.2.4, the colormap indicates the strength of the *Ez* component within the absorbing layer. The incident wave

is coming in from the top at this instance. White arrows indicate the Poynting vector, or the local flux of electromagnetic energy,

$$\vec{P} = \vec{E} \times \vec{H} \tag{2.31}$$

Relative to the incident direction, we have the θ angle indicating the scattering angle. The angular position θ was recorded at each timestep for diagnostic calculations that will be discussed below. The red dot indicates the maximum intensity of within the cross section. The maximum is slightly off center because the internal field is already reacting to the leading edge of the pulse. There is another maximum on the other side of the particle because of the symmetry of the problem and it's not shown. The number at the bottom right indicates the number of time steps where each time step is $\Delta t \sim 2.62 \times 10^{-17}$ sec.

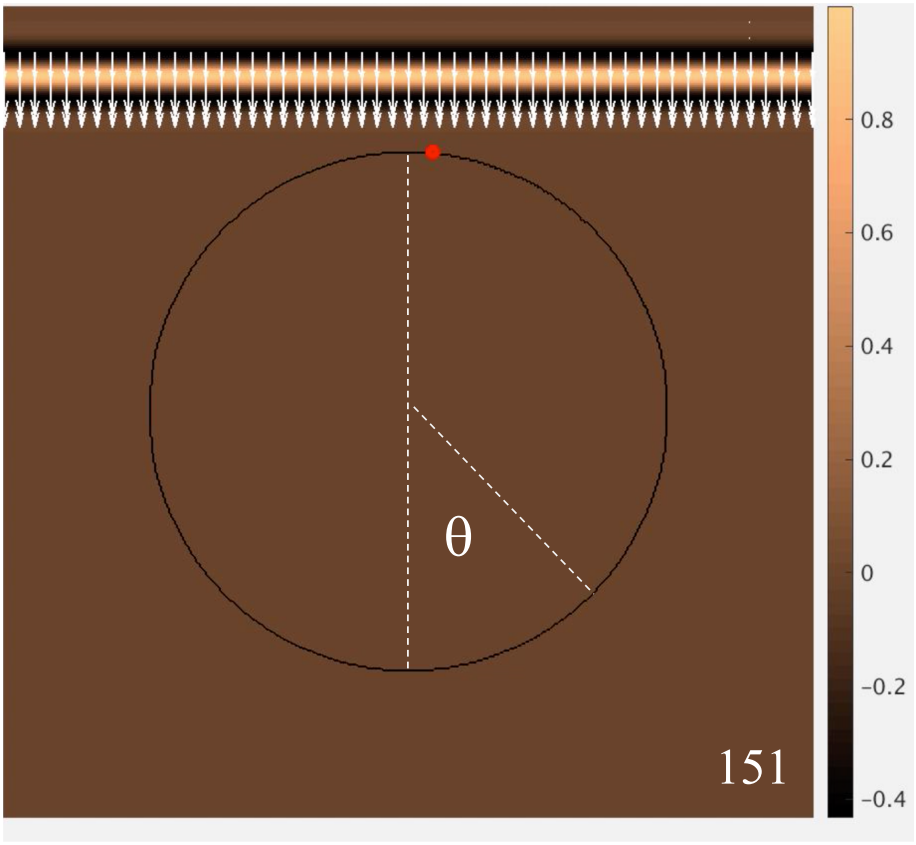

Figure 2.4 2D simulation geometry. Color map shows the strength of the *Ez* field. In this case, the incident Gaussian pulse is coming into the computational domain from the top. White arrows indicate the strength and direction of the Poynting vectors. The number at the bottom indicates the time step. (Reprinted with permission from [16]**)**

Fig.2.5 shows the *Ez* field at later stages of the simulation. Fig.2.5(a) and (b) show that parts of the incoming pulse outside the particle has moved further down than the part that has entered the particle. This is expected since wave moves more slowly inside the particle due to its higher index of refraction. Also, the internal energy flux gradually focuses in the forward scattering direction. The maximum amplitude of the *Ez* field moves near the surface of the particle.

Fig.2.5c shows the instant just after the two counter-propagating wave packets inside the particle have met and coalesced. The counter-propagating wave packets moved further and started to "split" apart symmetrically. At this moment the maximum amplitude is concentrated in a relatively narrow stream outside the particle moving off in the forward-scattering direction. This is similar to the presence of a "photonic nanojet" in images of the electric field in the frequency domain [17]. After this stage, the major characteristics of the *Ez* field evolution can be described as dominated by wave packets with maximum amplitude near the surface of the particle, along with internal curvilinear concentrations of amplitude similar to caustic-like features. Wave packets travelling near the particle surface can in a sense be related to the classical "electromagnetic surface waves" [18][19].

Fig.2.5 (e~l) shows that the counter-propagating surface wave packets continue travelling around the particle surface and during this process, gradual energy release is happening around the circle. While the wave packets meet and collide, bursts of energy are shed in the direct forward and backward scattering direction. The amplitude decreases with time.

Major release of energy in the forward and backward directions can generally be conceptually related to the familiar forward and backward peaks in the phase function S_{11}, although we cannot see the interferences of the scattered waves happening outside our limited computational domain. The intermittent bursts of oscillatory *Ez* leaves a signal in time when they pass certain observation points outside the particle. These signals must have the appearances of the semi-periodic pulses in Fig.2.3.

Fig.2.14 shows evolution of field energy in a different way inspired by [20]. The time evolution shown is after timestamp 1500, by which time the incident pulse has already left the computational domain; it is happening between Fig.2.5(e) and (f). Fig.2.14(a) shows the energy at a fixed radius outside the particle as a function of the scattering angle θ and time. Fig.2.14(b) shows the total energy within the particle as function of angle and time. The energy is recorded in a cone of width 2 degrees centered on the angle θ. The upper row of 3 panels are of the circular case; lower rows of 3 panels are for the elliptical and hexagonal cross sections discussed later. In order to deal with the decay of energy with time, the rows are divided into 3 successive time intervals.

The amplitude maxima occurring at near backscattering in the 2nd panel for the circle in Fig.2.14(a) and the one at the forward scattering angle in the 3rd panel are to be expected (wave front passes in Fig.2.5(g)and(j) at the same time and location). The maximum near 105 degrees near timestep 2000 in the 1st panel is difficult to interpret. It also shows up in the internal energy plot at about the same time. at these times, the animations show that the energy being launched at about timestep 1771(Fig.2.5(f))

reaches the observation radius during the interval of the amplitude maximum in the 1st panel.

The 2nd two panels in Fig.2.14(a) and (b) suggest that there is approximately constant angular velocity in the movement of the wave packet. Another method of diagnosis is called upon which helps in relating the features of the wave field and release of energy from the particle. The red dots in Fig.2.5 record the location of maximum |Ez| inside the particle. The amplitudes and corresponding positions of the red dots, together with values of total internal electromagnetic energy inside and outside the particle were recorded during the simulations and are displayed in Fig.2.6. Fig.2.6 also shows features of the electromagnetic field inside (left column) and outside (right column) the particle. "Outside the particle" refers to the area outside the particle and within the absorbing layer in our computational domain. Logarithmic scale is used in panels a,b,e,f on the y-axis. Panel (a) (b) show, respectively, a time series of the value of the total electromagnetic energy within the particle and maximum |*Ez*| at any interior grid point. The asterisks on the curve in the internal energy time series (2.6b) marks the times of the events shown in Fig.2.5; the same meaning applies for the asterisks on the time series of external energy (2.6f). To help in recognizing the transition of internal and external events, the dotted curve in panel 2.6f is a copy of the internal energy curve shown in Figure 2.6b. The subsequent pulse emissions are not as clearly defined as the first in the total energy field in the circle case. It is recognizable by the episodic burst-like behavior of the interior grid point maximum |*Ez*|.

At first the interior maximum |*Ez*| (2.6a) increases as part of the incident pulse enters the particle, remains approximately constant until the "focusing" of energy in Fig.2.5(b)(c) causes a local rise at the area from which the first forward pulse will be emitted. As the first forward pulse is emitted, the maximum |*Ez*| drops. At the same time, the total internal electromagnetic energy drops sharply, while outside the particle, the maximum |Ez| and total electromagnetic energy (2.5e,f) rise.

After that, the formation of backward and forward jets are indicated by the short jiggles on the maximum |Ez| curve in 2.6a, which are observed to occur when counter-propagating packets coalesce. Subsequent decreases in total energy inside the particle when backward or forward jets are formed are too small to show on the plots.

The bottom 2 panels in each column show the positions of grid point |Ez| maxima. It is quite difficult to track locations of maximum |Ez| because the maximum is attained along a curve, rather than a single point in a locally oscillating wave packet structure. In Fig.2.5(a~l), the "bottom" of the circular boundary corresponds to the bottom edge (0^o) of a θ plot in the panels. In Fig.2.6c,g, which show radial position, the solid red line indicates the distance corresponding to the radius of the particle. Certain features are clearly apparent in spite of the irregularities, especially after the main pulse passes by.

First, the confinement of maximum interior |*Ez*| near the boundary of the particle is clear. In other words, the maximum point does stick to the boundary, although there is some kind of a "hopping" between two preferred near-boundary positions that eventually disappears. This hopping can be related to the complicated near surface structure

reported in [21]. our numerical resolution may be insufficient to represent every detail of the structure. After the incident pulse has passed by, the movement of the maximal |*Ez*| location around the particle boundary appears to be at a constant angular velocity (θ_{max} plots in panels 2.6(d)(h)).

The θ_{max} plots "time" events in the other panels of Fig.2.5. The 3 short bursts of interior maximum |Ez| of similar shape seen in Fig.2.6a mentioned above are associated with the interaction of the counter-propagating wave structures that result in the emission of pulses. The times at which maximum |Ez| outside the particle gets far away from the particle mainly happen in the period between the first forward nanojet pulse and the first backward pulse. Parts of the incident pulses that passes by the particle and the nanojet pulse itself are connected to the first two outward movement events. The third outward movement of the field maximum in the particle exterior occurs before the first backscatter pulse in between Fig.2.5f and 2.5g. The outward moving field maximum is part of a broader outward-sweep structure that follows the exiting nanojet pulse. The pulse maintains a clear but weak connection to the field in the particle interior as it spreads away from it. Recall that after the incident pulse has existed the computational domain, the field maximum |*Ez*| in the particle interior is travelling at an approximately constant angular velocity. This observation suggests a consideration of how this speed might compare with the light speeds inside and outside the particle. Although the hopping of the |Ez| maximum and numerical noises makes the resulting series quite noisy, we attempted to measure the speed by measuring the radial position and using a finite difference approximation for angular velocity.

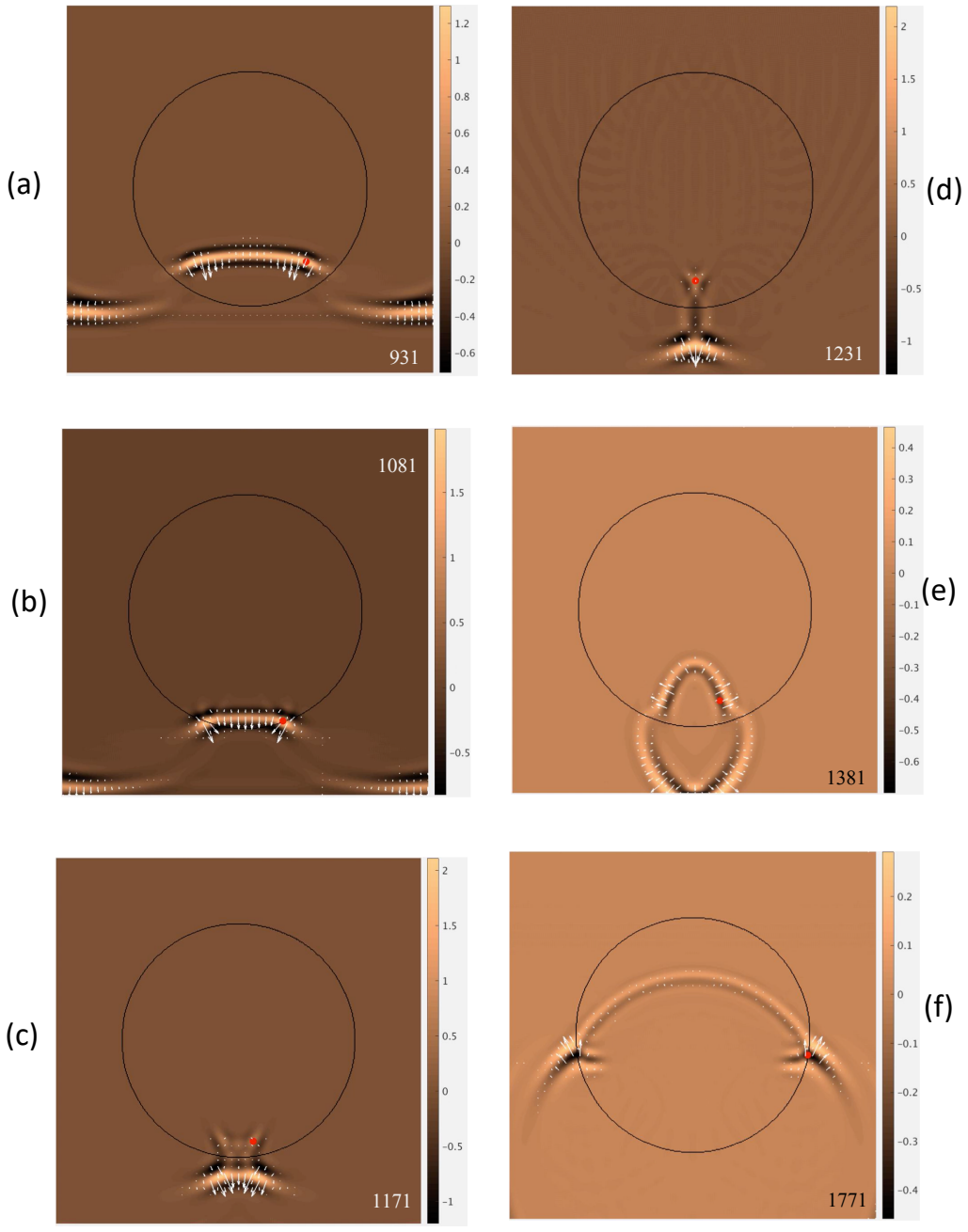

Figure 2.5 Incident Gaussian pulse interacting with cylindrical crystal with circular cross-section. Time steps are indicated in the panels. (Reprinted with permission from [16]**)**

Figure 2.5 Continued

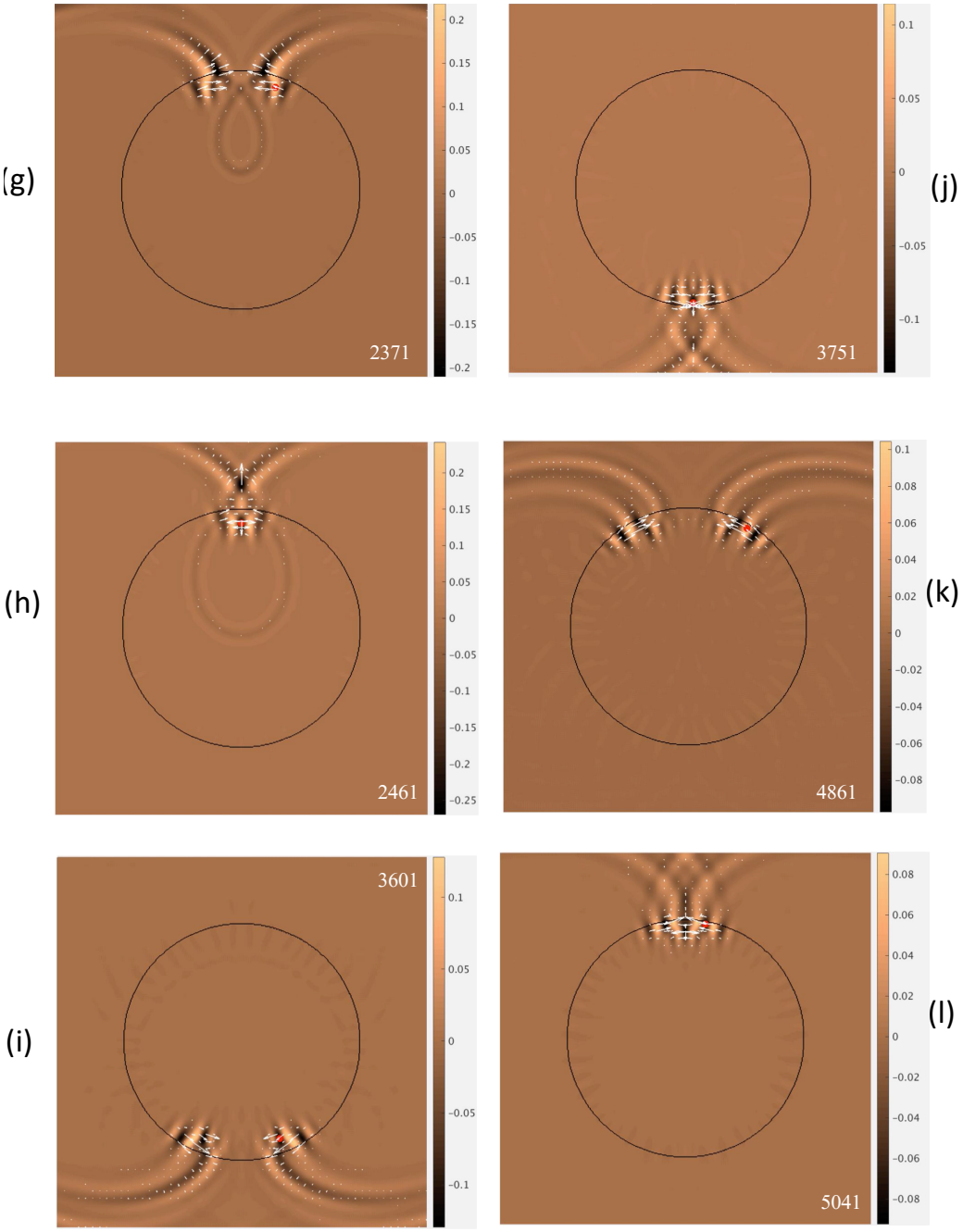

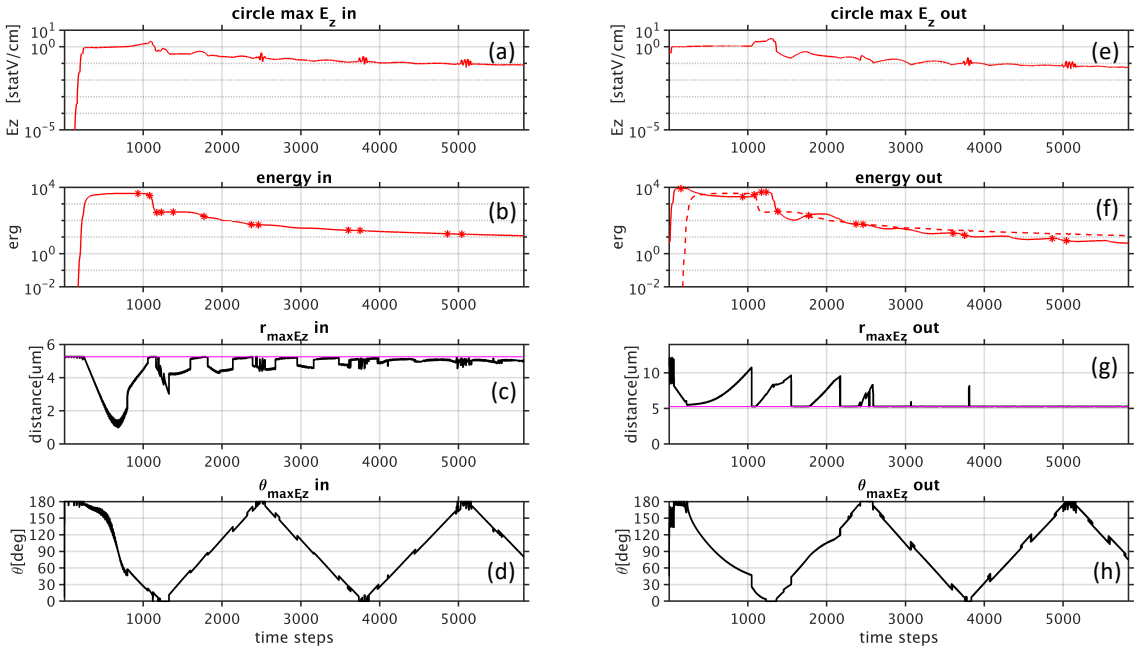

Figure 2.6 Time series of data gathered inside and outside and outside the circular cross section. The quantities shown are (a,e) pointwise maximum |Ez|; (b,f) total electromagnetic energy; (c,g) distance of pointwise maximum, with red line indicating particle boundary; and (d,h) Angle of the pointwise maximum. see text for details. (Reprinted with permission from [16])

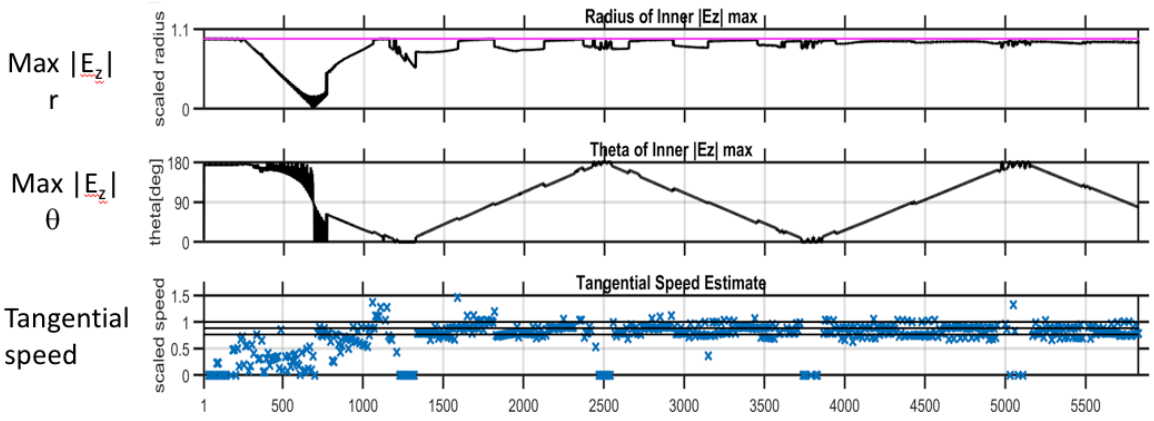

Figure 2.7 Tangential speed measurements of movements of |Ez| maxima. The speeds are normalized with vacuum light speed. See text for details. (Reprinted with permission from [16]**)**

Now we turn to two other cross sections with less symmetry: Elliptical and hexagonal. In these shapes there are other mechanistic features that excite pulse releases, namely variation in surface curvature.

Figures 2.8(a-l) show images from an elliptical cross-section for which the size parameter is x=30 and the aspect ratio is 0.5 (ratio of the semi-minor axis to the semi-major axis). Overall, the ellipsoid field snapshots are qualitatively similar to those of a sphere. The nanojet feature in fig.2.5d is no longer strong but it is visible in Fig.2.8d. We see a broad and less focused wave front. Figs.2.8(e-g) show something not present in the circular case: as the wave packets travel near the surface of the particle to around 90 degrees, a wave is generated and spins out, carrying electromagnetic energy away from the particle.

Remaining panels show the same kind of energy release as the near-surface wave packets encounter regions of high curvature. Figs.2.8i,j show that compared to the circle, the backscattered pulse is broader and less focused. These qualitative observed patterns about the energy release at high curvature spots can be quantified as shown in Fig.2.9 and 2.10. As in Fig. 2.6, Fig.2.9 shows time series of local |*Ez*| maximum values, total electromagnetic energy, the radial and angular position of the |*Ez*| maximum inside and outside the particle.

As in Fig.2.6f, the internal energy curve is plotted as a dotted curve in Fig.2.9f. Again, tracking position with the θ_{max} time series, it can be recognized that the intermittent "bursts" in the |Ez| series correspond to surface wave packet maxima colliding at direct forward and direct backward scattering angles. We see that the major drops in electromagnetic energy happen in between these events, when the maxima enter the regions of maximal curvature.

Unlike the case of a circle, the angular velocity indicated by the θ_{max} time series in Fig.2.9d is not constant. As the wave packets travel to areas of higher surface curvature their velocity decreases. After the wave packets pass this region their angular velocity increases again. Also, this is the spot where major energy release takes place. Similar behavior is seen in the movement of total internal energy (middle row of Fig.2.14b). The appearance of strong energy maxima outside the particle is a very striking feature (middle row in Fig.2.14a, at around 90 degrees)

Fig.2.10 shows the relation between energy release and curvature, for ellipses with 2 different aspect ratios. Green curves are analogous quantities of circular cases.

For the ellipses, it is the radius of curvature divided by the incident Gaussian pulse half-width. It is apparent that the electromagnetic energy drops most dramatically for the ellipse with smaller aspect ratio(b/a=0.5) when the wave packet hits regions of high curvature. In the case of the ellipse with a larger aspect ratio the effect is less dramatic, and the overall rate of energy loss is much slower (closer to that of a circle).

Another consideration is that the situation is different for a different orientation of the ellipse. We do not show here the detailed field evolution when the major axis is parallel to the incident direction. We only point out some notable features seen in the simulations: There are no massive spin-outs at regions of maximum curvature, since they are in the exact forward and backward directions parallel to the incident direction. The major energy release is in nanojet-like features in the direct forward and backward directions similar to those in the circular case. When the major axis has an orientation between these 2 extremes, mixtures of energy release of both kinds occur.

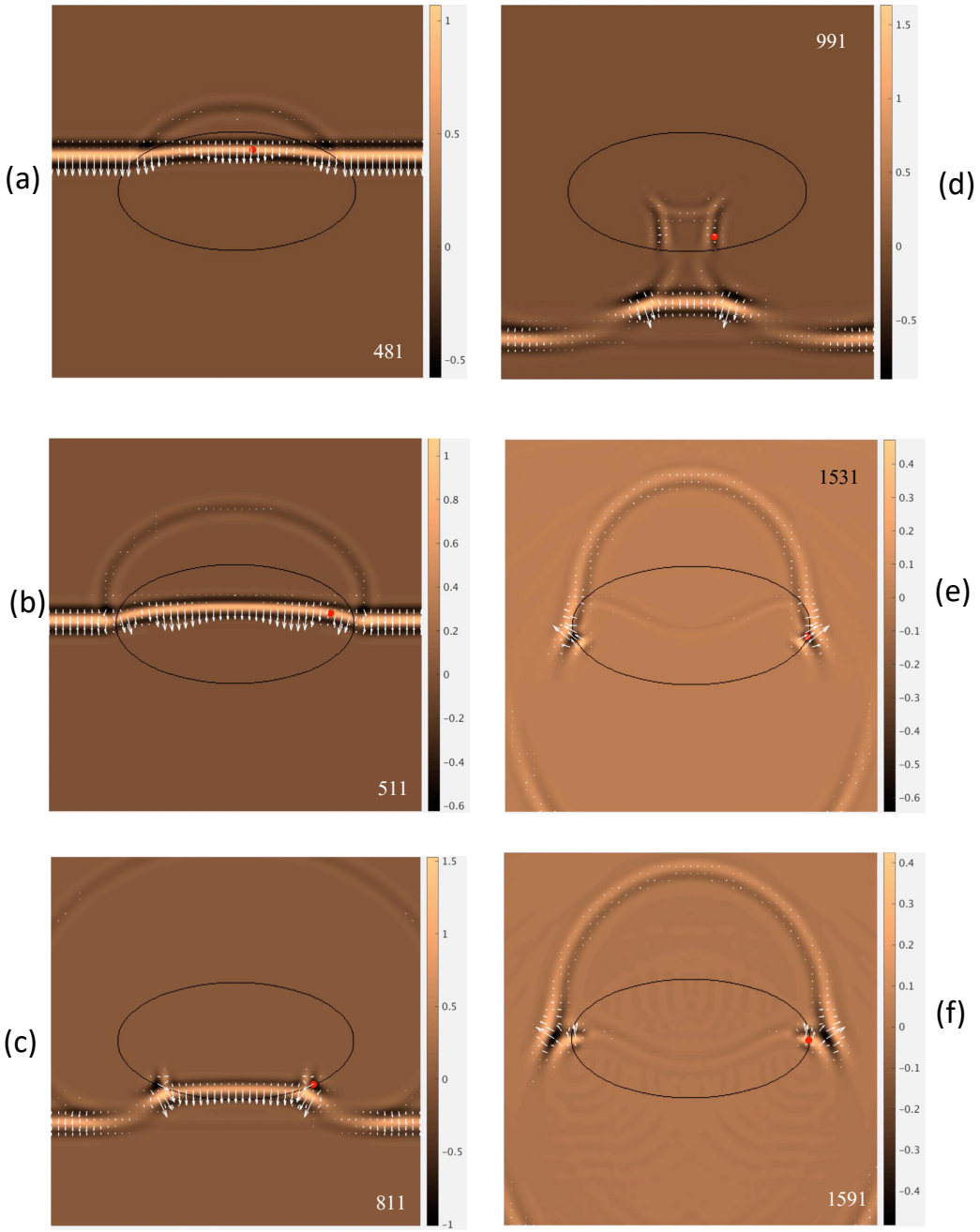

Figure 2.8 As in Fig.2.5, but evolution of the Ez field around a particle with elliptical cross section. (Reprinted with permission from [16])

Figure 2.8 continued

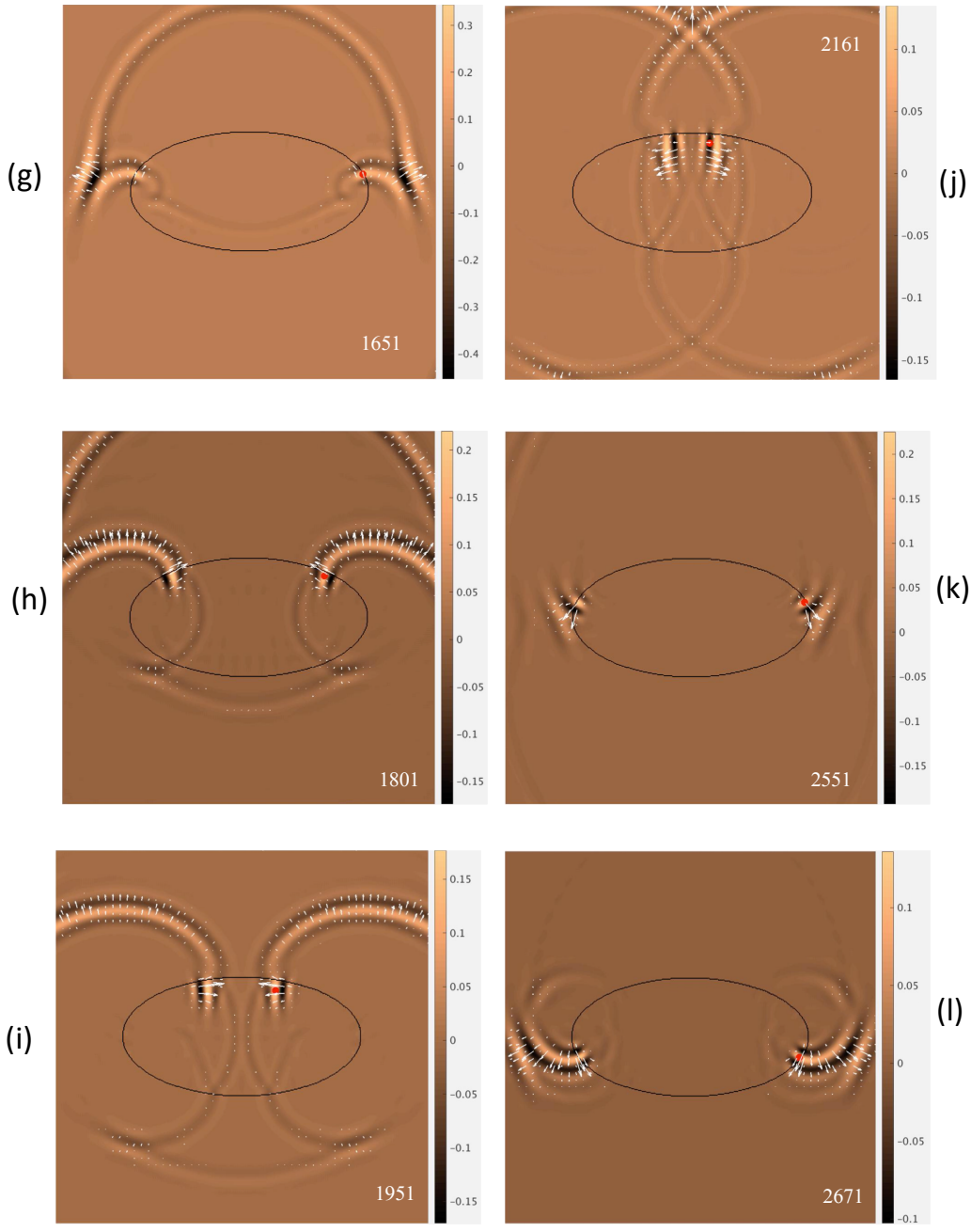

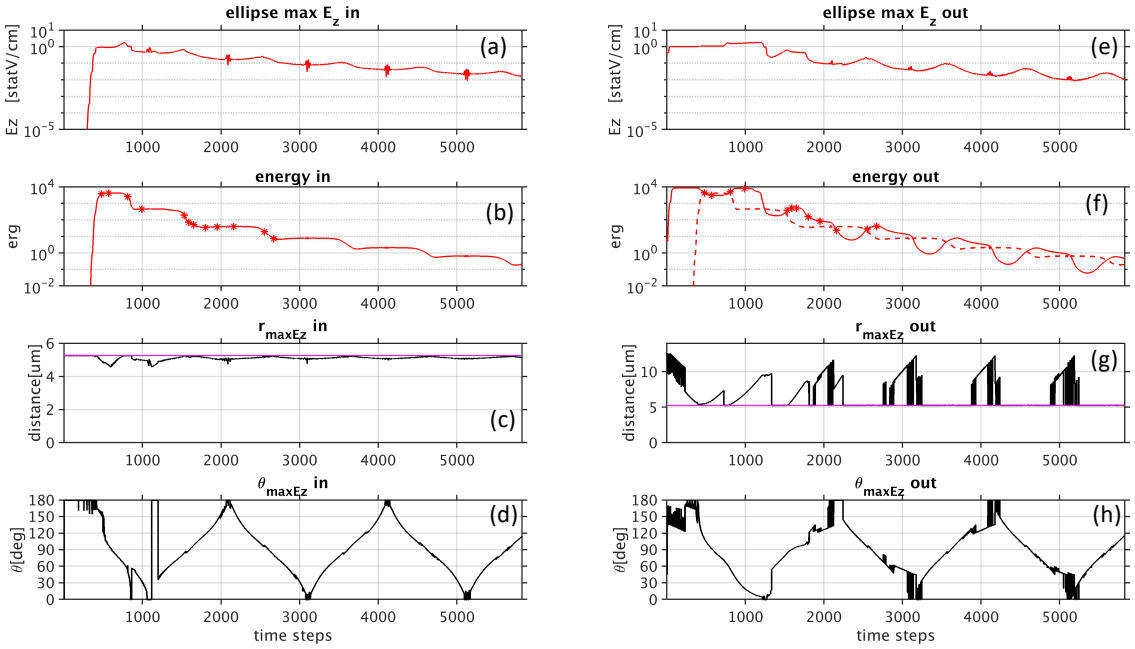

Figure 2.9 As in Fig.2.6, but for an elliptical cross section. (Reprinted with permission from [16])

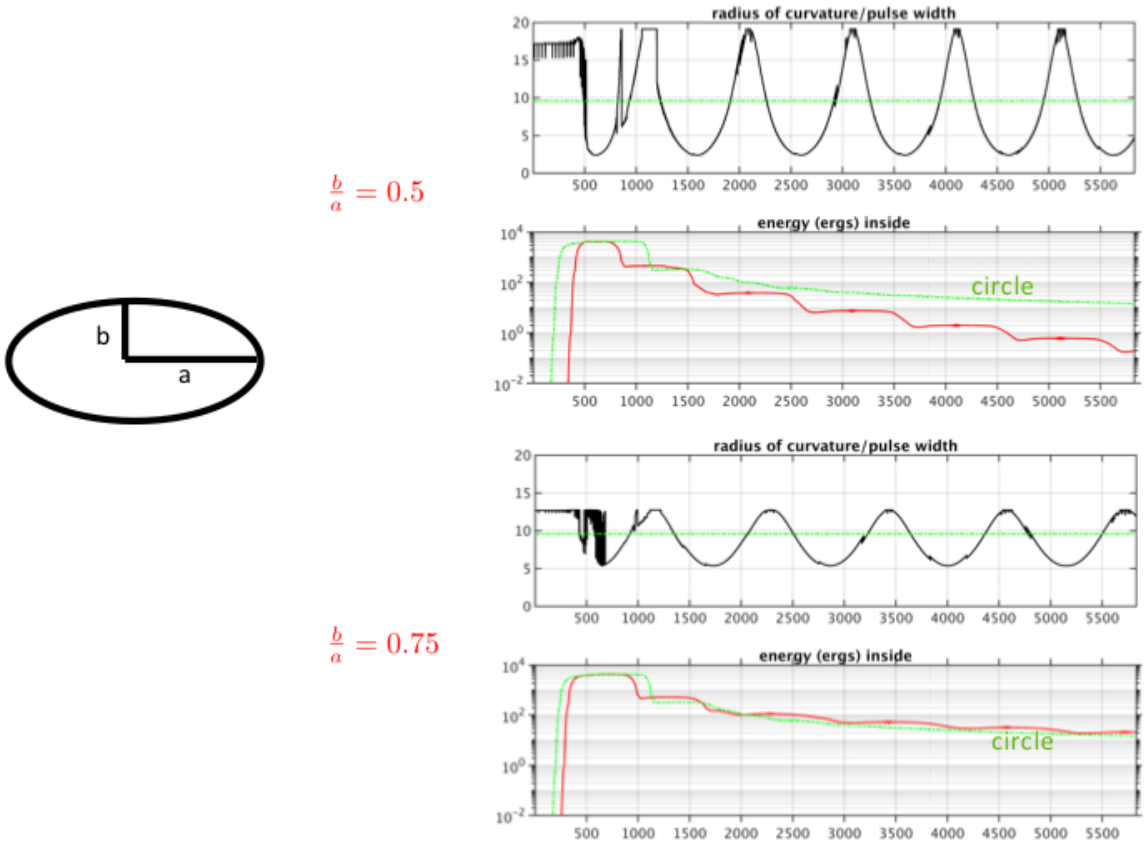

Figure 2.10 Time series of surface curvature at point on interface of elliptical particle with same angle as nearby interior |Ez| maximum, and total electromagnetic energy, for two aspect ratios of the ellipse. In panels 2 and 4, the time series of the total energy for the circular cross section is included for comparison. (Reprinted with permission from [16]**)**

In the case of a hexagonal cross-section, it is expected that there is more energy release when the surface wave packet moves across corners, based on the effect of curvature in the case of an elliptical cross section.

Fig.2.11 shows selections of field images chosen to illustrate behaviors near corners. In Fig.2.11b, the first forward nanojet has almost existed the domain, and the incident pulse has mostly exited the computational domain. The red dot in the image indicates a maximum at a midpoint position along the bottom edge of the particle, but evidence can be seen of a leading pair of oppositely propagating features near the boundary. In 2.11c, the internal maximum has travelled around the first corner on its way back to the backscatter direction.

Note that the flux of electromagnetic energy indicated by the Poynting vector, which is parallel to the bottom surface of the particle, is heading away from the particle. When the travelling maximum |*Ez*| meets a corner, energy will be released parallel to the particle side at the same time. This turns out to be a characteristic of the field evolution in the case of a hexagonal cross section. Figs.2.11f and g show this phenomenon at the next corner, at the next corner, at the top corners. Figure 2.11h shows the bonus effect of enhancing the backscattering jet shown in Figure 2.11i. This jet is formed by interference between the outward moving wave packet generated at each of the top corners by the counter-propagating wave packets and another created by the coalescence of wave packets. The remaining 3 panels in Fig.2.11 show subsequent corner encounters of the wave packet. The final one of the three shows the emerging of a flux that will contribute to another forward-scatter pulse a few timesteps later in Fig.2.11i. Note that the |Ez| maximum often appears well within the particle interior, mostly along the vertical symmetry axis. Those images are not all shown here. Suggestions of how this

might occur are seen in Fig.2.11(c-e). In non-circular particles we have simulated, occurrence of internal energy maximum well within the particle is a common feature.

Similar to the case of the elliptical cross section, the time-angle dependence of the energy outside the particle shown in third row of Figure 2.14a is distinctive. Outward bursts of energy are recorded at angles near 30 ,60 and 120 degrees. In addition, the first panel shows amplitude maxima near 180 degrees. Figure 2.11i displays the Ez field at timestep 2281, during the period when the maxima appear: clearly the maxima are a signal of the first backscattering pulse. At timestep 3500, the subsequent forward scattering pulse appears as the maximum in the lower-right edge of the middle panel.

To illustrate the major events just described more quantitatively, Figure 2.12 is constructed as in Figures 2.6 (circle) and 2.9 (ellipse). One surprising finding is the apparent constancy of angular velocity shown in the θ_{max} time series, unlike in the case of the ellipse. While in the movement of the radial position of the |Ez| maxima, there is evidence of corner encounters, there is virtually no impact on the speed of progression of the maxima around the particle.

Again, this time series serves to track the timing of key events: The three major drops in internal electromagnetic energy, equally spaced in time between these corner encounter events, near-surface location of the maximal |Ez| at the onset of these energy drops and the quasi-periodic bursts of maximal |Ez| in the forward and backscatter pulse generation events. (Note: The two red lines in the time series for distance from the particle center indicate the maximum and minimum distances of points on the hexagon profile from its center.)

Fig.2.13 compares time series for the three non-circular cases (two ellipses and one hexagon) and with the time series for the circle. It is clear from the figure that the strong "flattening" of the ellipse with aspect ratio 0.5 has accelerated the rate of energy release dramatically in comparison with the other cases. If an ellipse with larger aspect ratio is considered to be a less deformed circle, we might expect the ellipse with a larger aspect ratio to have a rate of energy release closer to that of the circle. However, we have no explanation for the fact that the rate of release is actually slower than that of the circle for most of the evolution after the main incident pulse has passed by. We also have no explanation for the fact that the rate of release of energy from the hexagonal particle is similar to that seen in the circular case for a while, but then increases significantly.

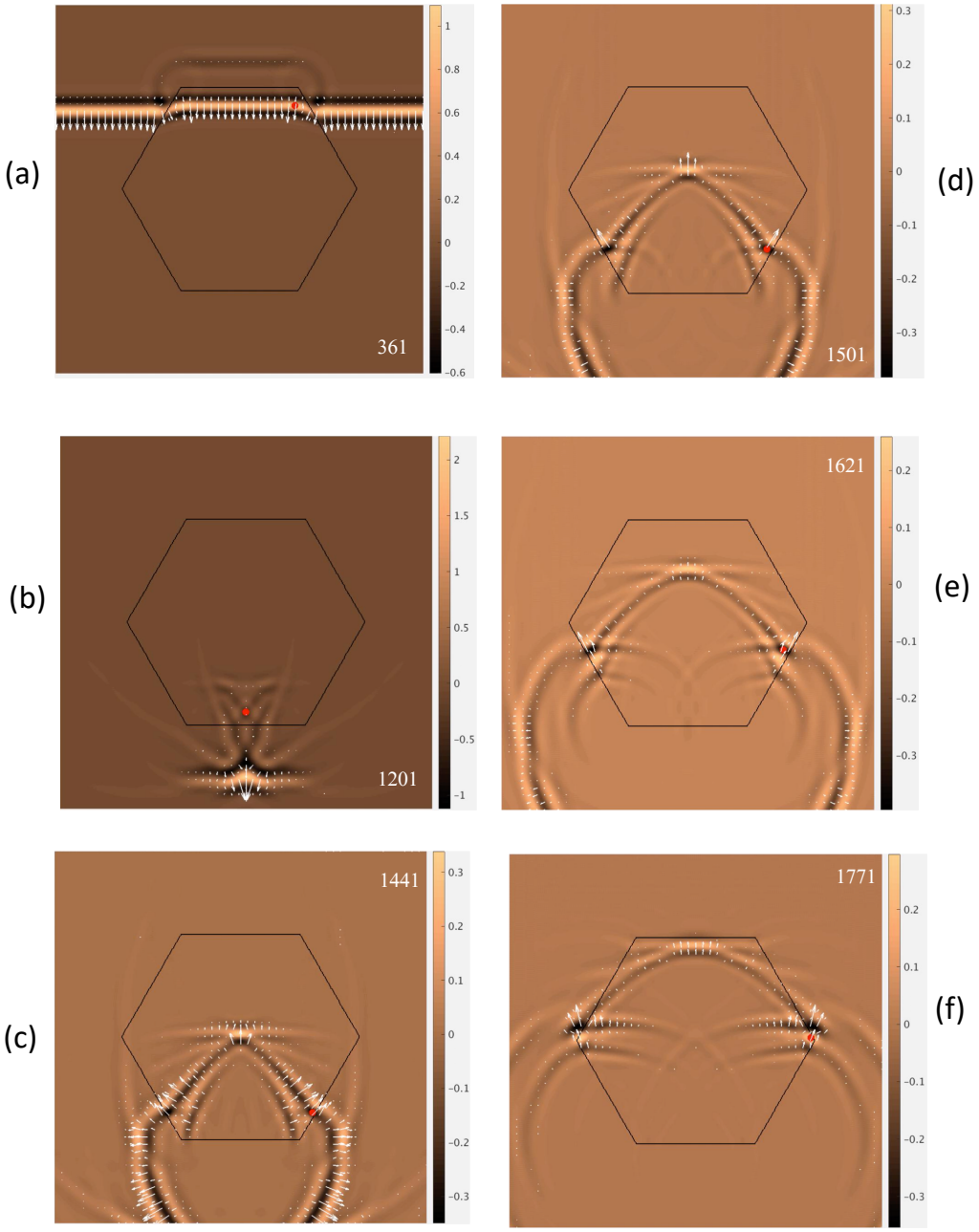

Figure 2.11 As in Fig.2.5 but showing the Ez field evolution of the hexagonal cross section. (Reprinted with permission from [16])

Figure 2.11 Continued

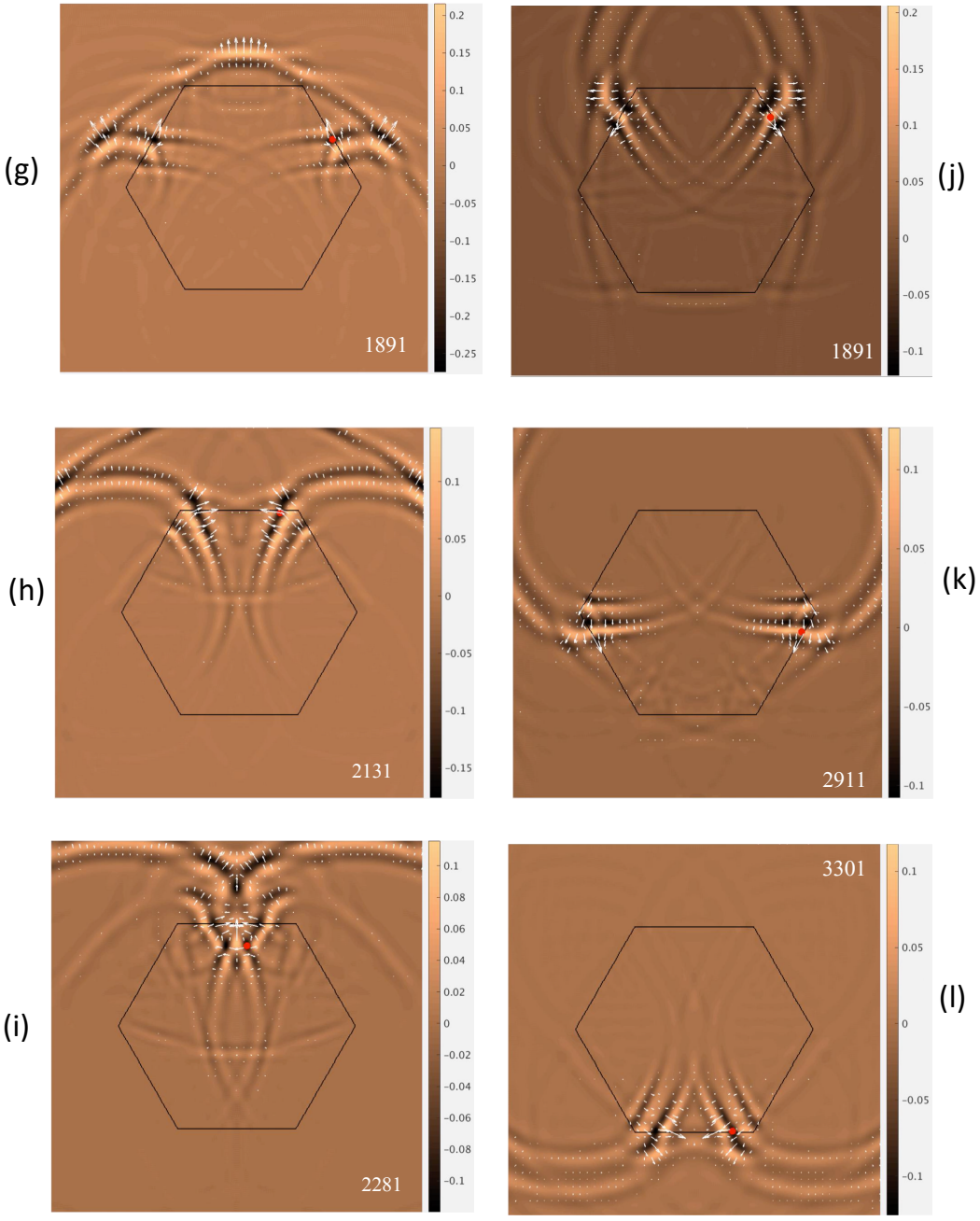

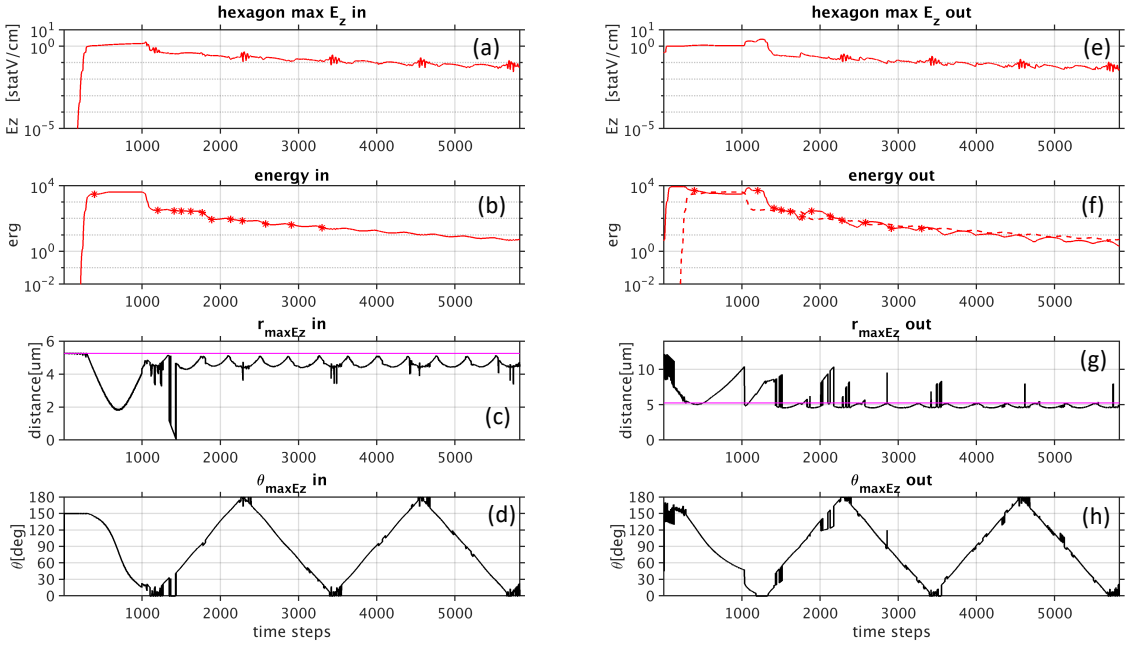

Figure 2.12 As in Fig.2.9, but for a hexagonal cross section. (Reprinted with permission from [16]**)**

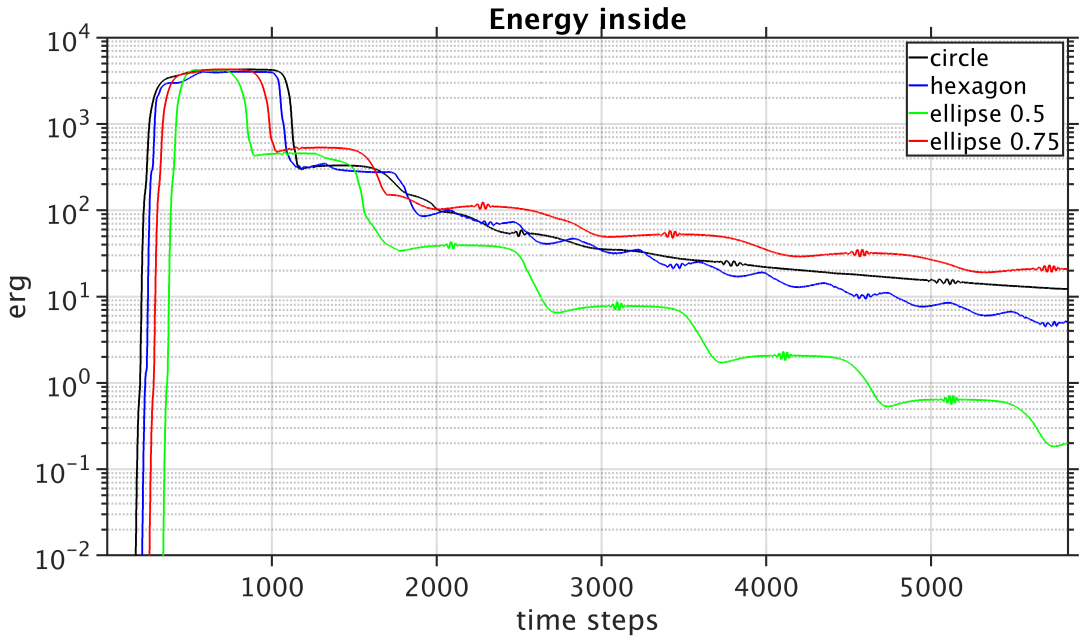

Figure 2.13 Comparison of time series of total internal electromagnetic energy for cases of circular cross section, two different elliptical cross sections (aspect ratio 0.5 and 0.75), and hexagonal cross section. (Reprinted with permission from [16])

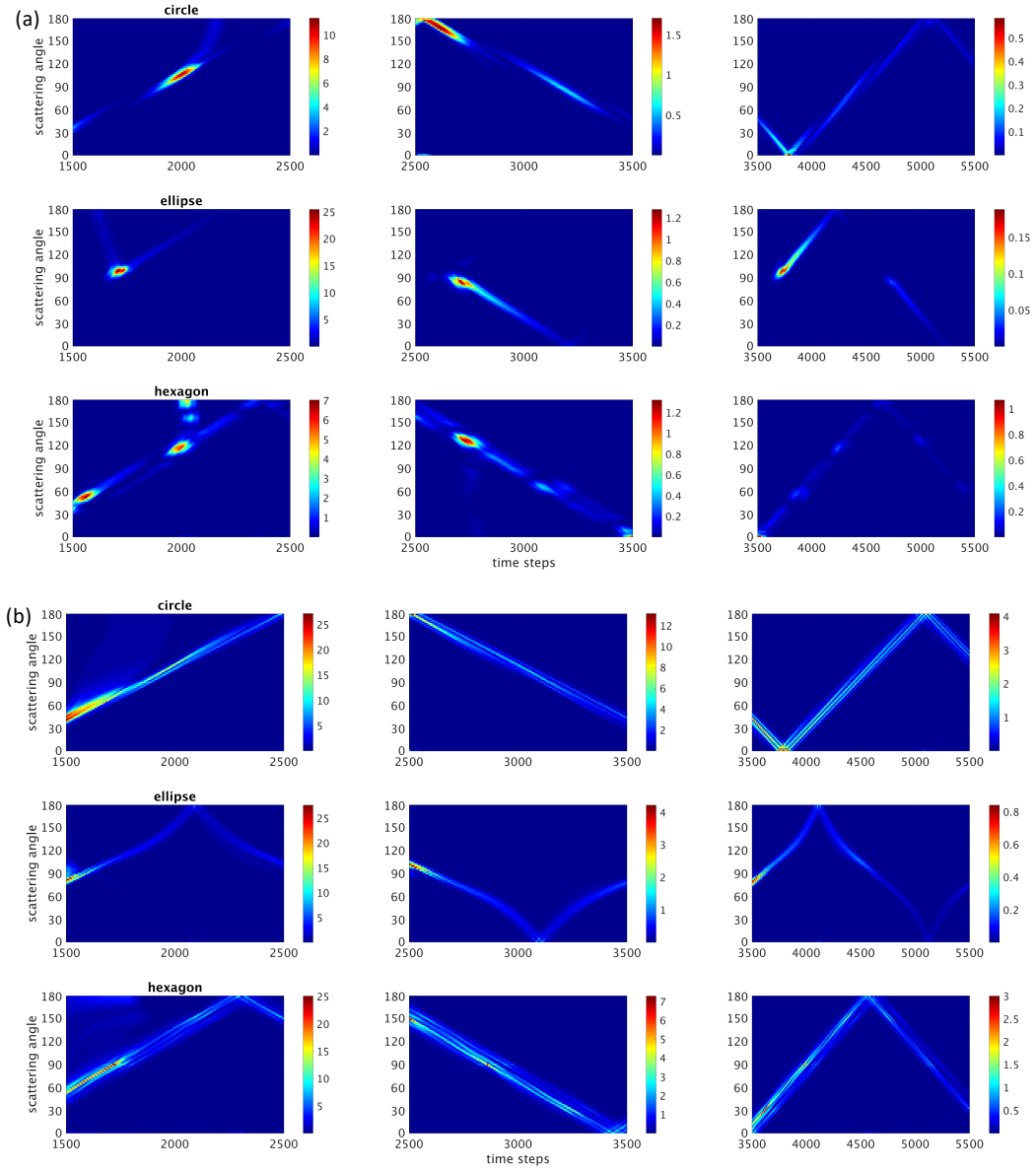

Figure 2.14 Angle-time diagram for (top row)circle, (middle row)ellipse and (bottom row)hexagonal cross sections: (a) at a fixed distance outside (b) total inside. See text for details. (Reprinted with permission from [16])

3. THE INVARIANT IMBEDDING T-MATRIX METHOD

A special approach to the single scattering problem is the Transition Matrix (T-matrix) method. The T-matrix is the linear transformation between the expansion coefficients of the incident wave and the scattered wave. All information about a particle's single scattering properties are contained in the T-matrix. The T-Matrix is an inherent property of the particle; in particular, it depends only on the particle structure, size and refractive index. The T-matrix of a homogeneous sphere reduces to a diagonal form with matrix elements corresponding to the Lorenz-Mie series expansion coefficients. For nonspherical particles, the T-matrix method is computationally efficient because it is feasible to analytically average the optical properties over random orientations, as originally illustrated by [6].

This dissertation focuses on one particular discretization scheme for solving the T-matrix: The invariant-imbedding T-matrix (II-TM) method [7][8]. Mathematically speaking, Eq.3.1 with the free-space Green's Function is a Fredholm integral equation with a degenerate kernel. Eq.3.1 is a two-point boundary value problem before we apply the method of invariant imbedding. Expanding all field quantities with the vector spherical wave functions (VSWFs), the T-matrix relating the expansion coefficients is introduced into the equation sets. The method of invariant imbedding is applied in matrix equations 3.40~41. By regarding the solution at a fixed point as a function of the interval of integration, a matrix differential equation is obtained for the T-matrix. In its discretized form, the matrix differential equation provides a radial recurrence formula

for the T-matrix. The T-matrix corresponding to the portion of the scattering particle enclosed by a spherical shell of one radius can be used to obtain the T-matrix of the next radius.(Fig.3.1) Through the use of the invariant imbedding method, the original boundary value problem of Eqs 3.1, 3.40, and 3.41 is transformed into an initial value problem suitable for numerical computation.

The computational procedure of II-TM method for a non-spherical particle can be divided into three major parts:

1.Surface integrations on each spherical shell to obtain the particle geometry

2.Radial recurrence to obtain the final T-matrix

3.Orientation averaging

We aim to improve the computational efficiency of the Gaussian quadrature in the surface integrations by implementing a new node and weight generating algorithm [13]. Also, the method is modified to avoid doing quadrature over discontinuities for hexagonal columns so the convergence rate can be accelerated.

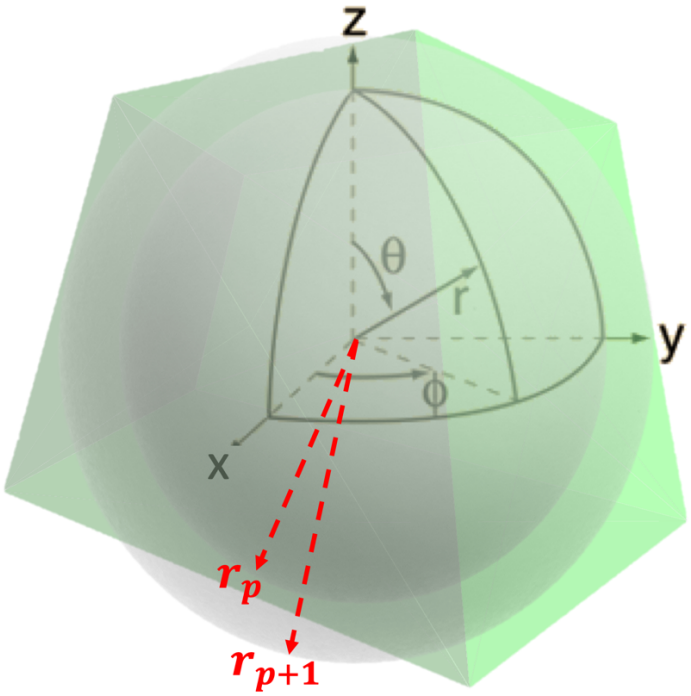

Figure 3.1 Schematic of the radial recurrence. Particle in this schematic is an irregular hexahedron marked in green. It could be any non-spherical inhomogeneous particles. Coordinate origin is on the geometric center of the hexahedra. Two spherical shells are indicated in transparent grey color. Red dashed arrows indicate the two radii r_p and r_{p+1}.

3.1. The invariant imbedding T-matrix method

The volume integral equation containing the total field $\vec{E}(\vec{r},\omega)$ at a certain frequency ω [8] is

$$\vec{E}(\vec{r}) = \overrightarrow{E_0}(\vec{r}) + k^2 \iiint_V d^3\overrightarrow{r'}\left[m^2\left(\overrightarrow{r'}\right) - 1\right]\left[\left(\bar{\bar{I}} + \frac{1}{k^2}\nabla'\nabla'\right)\frac{e^{ik\left|\vec{r}-\overrightarrow{r'}\right|}}{4\pi\left|\vec{r}-\overrightarrow{r'}\right|}\right] \cdot \vec{E}\left(\overrightarrow{r'}\right), \tag{3.1}$$

Due to the linearity of the equation, the incident $\overrightarrow{E_0}$ and the scattered field $\overrightarrow{E_s}$ can be related through a linear transformation with respect to their expansion with Vector Spherical Wave Functions (VSWF) [8],

$$\overrightarrow{E_s}(\vec{r}) = \sum_{n=1}^{\infty}\sum_{m=-n}^{n} \bar{\bar{Y}}_{mn}(\theta,\varphi)\bar{\bar{H}}_n(r)\begin{pmatrix} p_{mn} \\ q_{mn}\end{pmatrix}, \quad r > R \tag{3.2}$$

$$\overrightarrow{E_0}(\vec{r}) = \sum_{n=1}^{\infty}\sum_{m=-n}^{n} \bar{\bar{Y}}_{mn}(\theta,\varphi)\bar{\bar{J}}_n(r)\begin{pmatrix} a_{mn} \\ b_{mn}\end{pmatrix}, \tag{3.3}$$

where R is the radius of the circumscribing sphere of the particle. The angular functions are contained in the $\bar{\bar{Y}}_{mn}(\theta,\varphi)$ matrix given by,

$$\bar{\bar{Y}}_{mn}(\theta,\varphi) = (-1)^m \left(\frac{2n+1}{4\pi n(n+1)}\right)^{\frac{1}{2}} \times$$
$$e^{im\varphi}\begin{pmatrix} 0 & 0 & \sqrt{n(n+1)}d_{0m}^{n}(\theta) \\ i\pi_{mn}(\theta) & \tau_{mn}(\theta) & 0 \\ -\tau_{mn}(\theta) & i\pi_{mn}(\theta) & 0 \end{pmatrix} \tag{3.4}$$

where $d_{0m}^{n}(\theta)$ is the Wigner-d function and,

$$\pi_{mn}(\theta) = \frac{m}{sin\theta} d_{0m}^{n}(\theta), \tag{3.5}$$

$$\tau_{mn}(\theta) = \frac{d}{d\theta} d_{0m}^{n}(\theta), \tag{3.6}$$

the radial functions are contained in the $\bar{\bar{H}}_n(r)$ and $\bar{\bar{J}}_n(r)$ matrices given by,

$$\bar{\bar{H}}_n(r) = \begin{pmatrix} h_n^{(1)}(kr) & 0 \\ 0 & \frac{1}{kr}\frac{\partial}{\partial r}\left(rh_n^{(1)}(kr)\right) \\ 0 & \sqrt{n(n+1)}\frac{h_n^{(1)}(kr)}{kr} \end{pmatrix} \tag{3.7}$$

$$\bar{\bar{J}}_n(r) = \begin{pmatrix} j_n(kr) & 0 \\ 0 & \frac{1}{kr}\frac{\partial}{\partial r}(rj_n(kr)) \\ 0 & \sqrt{n(n+1)}\frac{j_n(kr)}{kr} \end{pmatrix} \tag{3.8}$$

where $h_n^{(1)}(kr)$ is the spherical Hankel function of the 1st kind, and $j_n(kr)$ is the spherical Bessel function of the 1st kind.

The transition matrix (T-matrix) relates the expansion coefficients,

$$\begin{pmatrix} p_{mn} \\ q_{mn} \end{pmatrix} = \sum_{m'n'} \begin{pmatrix} T^{11}_{mnm'n'} & T^{12}_{mnm'n'} \\ T^{21}_{mnm'n'} & T^{22}_{mnm'n'} \end{pmatrix} \begin{pmatrix} a_{m'n'} \\ b_{m'n'} \end{pmatrix} \tag{3.9}$$

The single scattering properties can be obtained with the T-matrix, in other words, the T-matrix contains all information about a particle's single scattering properties,

$$\begin{pmatrix} S_2 & S_3 \\ S_4 & S_1 \end{pmatrix} \sim \bar{\bar{T}} \tag{3.10}$$

To compute the T-matrix, we start from Eq.3.1, which can be rewritten as,

$$\vec{E}(\vec{r}) = \overrightarrow{E_0}(\vec{r}) + k^2 \iiint_V d^3\overrightarrow{r'}\, \chi\left(\overrightarrow{r'}\right) \left[\bar{\bar{G}}_0(\vec{r},\vec{r}') - \frac{1}{k^2}\delta(\vec{r}-\vec{r}')\hat{r}\otimes\hat{r}\right] \cdot \vec{E}\left(\overrightarrow{r'}\right), \tag{3.11}$$

Where $\bar{\bar{G}}_0(\vec{r},\vec{r}')$ is the free-space Green Function valid for a point source at $\vec{r}'$ in a medium that is otherwise a vacuum, $\chi\left(\overrightarrow{r'}\right) = k^2\left(m^2\left(\overrightarrow{r'}\right) - 1\right)$, $\hat{r}$ is the radial component of the spherical coordinates ($\hat{r} \quad \hat{\theta} \quad \hat{\varphi}$), the purpose of these maneuvers is to bring out

the $\bar{\bar{G}}_0(\vec{r},\vec{r}')$ explicitly so that we can use the series expansion in Eq.3.16. The outer product leads to,

$$\hat{r}\otimes\hat{r} = \begin{pmatrix}1\\0\\0\end{pmatrix}(1 \quad 0 \quad 0) = \begin{pmatrix}1 & 0 & 0\\0 & 0 & 0\\0 & 0 & 0\end{pmatrix}. \tag{3.12}$$

After some manipulations, we have,

$$\vec{E}(\vec{r}) = \overrightarrow{E_0}(\vec{r}) + \iiint_V d^3\overrightarrow{r'}\,\chi\left(\overrightarrow{r'}\right)\bar{\bar{G}}_0(\vec{r},\vec{r}')\cdot\bar{\bar{Z}}(\vec{r}')\cdot\vec{E}\left(\overrightarrow{r'}\right), \tag{3.13}$$

where $\vec{E}$ is the scaled version of the original electric field,

$$\vec{E}(\vec{r}) = \begin{pmatrix}m^2(\vec{r})E_r(\vec{r})\\E_\theta(\vec{r})\\E_\varphi(\vec{r})\end{pmatrix} \tag{3.14}$$

and $\bar{\bar{Z}}(\vec{r}')$ is,

$$\bar{\bar{Z}}(\vec{r}') = \begin{pmatrix}\dfrac{1}{m^2(\vec{r}')} & 0 & 0\\0 & 1 & 0\\0 & 0 & 1\end{pmatrix} \tag{3.15}$$

The free-space Green Function can be factorized into,

$$\bar{\bar{G}}_0(\vec{r},\vec{r}') = \sum_{n=1}^{\infty}\sum_{m=-n}^{n} \bar{\bar{Y}}_{mn}(\theta,\varphi)\,\bar{\bar{g}}_n(r,r')\bar{\bar{Y}}^{T*}_{mn}(\theta',\varphi') \tag{3.16}$$

where

$$\bar{\bar{g}}_n(r,r') = \begin{cases} ik\bar{\bar{H}}_n(r)\bar{\bar{J}}^T_n(r'), & r > r' \\ \dfrac{ik}{2}\left[\bar{\bar{H}}_n(r)\bar{\bar{J}}^T_n(r') + \bar{\bar{J}}_n(r)\bar{\bar{H}}^T_n(r')\right], & r = r' \\ ik\bar{\bar{J}}_n(r)\bar{\bar{H}}^T_n(r'), & r < r' \end{cases} \tag{3.17}$$

Insert Eq.3.16 into Eq.3.13. Then,

$$\begin{aligned} &\vec{E}(\vec{r}) \\ &= \overrightarrow{E_0}(\vec{r}) \\ &+ \iiint_V r'^2 sin\theta' dr' d\theta' d\varphi'\, \chi\left(\overrightarrow{r'}\right) \sum_{n=1}^{\infty}\sum_{m=-n}^{n} \bar{\bar{Y}}_{mn}(\theta,\varphi)\,\bar{\bar{g}}_n(r,r')\bar{\bar{Y}}^{T*}_{mn}(\theta',\varphi') \\ &\cdot \bar{\bar{Z}}(\vec{r}') \cdot \vec{E}\left(\overrightarrow{r'}\right), \end{aligned} \tag{3.18}$$

Practically speaking, through integration in the azimuth (φ) and zenith (θ) direction, this function aims at separating the angular (θ, φ) and radial (r) variables.

$$\vec{F}_{mn}(r) = r^2 \int_{\Omega} sin\theta d\theta d\varphi\, \bar{\bar{Y}}^{T*}_{mn}(\theta,\varphi)\chi\left(\overrightarrow{r'}\right)\bar{\bar{Z}}(r,\theta,\varphi)\vec{E}(r,\theta,\varphi) \tag{3.19}$$

Inserting Eq.3.18 into Eq.3.19,

$$\begin{aligned}
&\vec{F}_{mn}(r) \\
&= r^2 \int_{\Omega} sin\theta d\theta d\varphi\, \bar{\bar{Y}}^{T*}_{mn}(\theta,\varphi)\chi(\vec{r})\bar{\bar{Z}}(r,\theta,\varphi)\left[\overrightarrow{E_0}(\vec{r})\right. \\
&+ \iiint_{V} r'^2 sin\theta' dr' d\theta' d\varphi'\, \chi(\overrightarrow{r'}) \sum_{m'n'} \bar{\bar{Y}}_{m'n'}(\theta,\varphi)\, \bar{\bar{g}}_{n'}(r,r')\bar{\bar{Y}}^{T*}_{m'n'}(\theta',\varphi') \\
&\left.\cdot \bar{\bar{Z}}(\vec{r}') \cdot \vec{E}(\overrightarrow{r'})\right]
\end{aligned} \tag{3.20}$$

Grouping terms with $r', \theta'\ and\ \varphi'$ together, the integral in the square brackets becomes,

$$\begin{aligned}
&\int_0^R dr' \sum_{m'n'} \bar{\bar{Y}}_{m'n'}(\theta,\varphi)\bar{\bar{g}}_{n'}(r,r')\left(r'^2 \int_{\Omega} sin\theta' d\theta' d\varphi'\, \chi(\overrightarrow{r'})\bar{\bar{Y}}^{T*}_{m'n'}(\theta',\varphi')\right. \\
&\qquad \left.\cdot \bar{\bar{Z}}(\vec{r}') \cdot \vec{E}(\overrightarrow{r'})\right) \\
&\qquad = \int_0^R dr' \sum_{m'n'} \bar{\bar{Y}}_{m'n'}(\theta,\varphi)\bar{\bar{g}}_{n'}(r,r')\, \vec{F}_{m'n'}(r')
\end{aligned} \tag{3.21}$$

Eq.3.20 becomes,

$$\vec{F}_{mn}(r) = r^2 \int_{\Omega} sin\theta d\theta d\varphi \, \bar{\bar{Y}}^{T*}_{mn}(\theta,\varphi)\chi(\vec{r})\bar{\bar{Z}}(r,\theta,\varphi) \left[\overrightarrow{E_0}(\vec{r}) + \int_0^R dr' \sum_{m'n'} \bar{\bar{Y}}_{m'n'}(\theta,\varphi)\bar{\bar{g}}_{n'}(r,r')\,\vec{F}_{m'n'}(r') \right] \tag{3.22}$$

Expand $\overrightarrow{E_0}(\vec{r})$ in VSWFs,

$$\vec{F}_{mn}(r) = r^2 \int_{\Omega} sin\theta d\theta d\varphi \, \bar{\bar{Y}}^{T*}_{mn}(\theta,\varphi)\chi(\vec{r})\bar{\bar{Z}}(r,\theta,\varphi) \times \left[\sum_{m''n''} \bar{\bar{Y}}_{m''n''}(\theta,\varphi)\bar{\bar{J}}_{n''}(r) \begin{pmatrix} a_{m''n''} \\ b_{m''n''} \end{pmatrix} + \int_0^R dr' \sum_{m'n'} \bar{\bar{Y}}_{m'n'}(\theta,\varphi)\bar{\bar{g}}_{n'}(r,r')\,\vec{F}_{m'n'}(r') \right] \tag{3.23}$$

Define $\bar{\bar{U}}_{mnm'n'}$ matrices, sticking to the idea of separating angular and radial variables,

$$\bar{\bar{U}}_{mnm'n'}(r) = r^2 \int_{\Omega} sin\theta d\theta d\varphi \, \bar{\bar{Y}}^{T*}_{mn}(\theta,\varphi)\chi(\vec{r})\bar{\bar{Z}}(r,\theta,\varphi)\bar{\bar{Y}}_{m'n'}(\theta,\varphi) \tag{3.24}$$

Eq.3.22 becomes,

$$\vec{F}_{mn}(r) = \sum_{m''n''} \bar{\bar{U}}_{mnm''n''}(r)\bar{\bar{J}}_{n''}(r)\begin{pmatrix} a_{m''n''} \\ b_{m''n''} \end{pmatrix} + \sum_{m'n'} \bar{\bar{U}}_{mnm'n'}(r)\int_0^R dr'\,\bar{\bar{g}}_{n'}(r,r')\,\vec{F}_{m'n'}(r') \tag{3.25}$$

Expand $\vec{F}_{mn}(r)$,

$$\vec{F}_{mn}(r) = \sum_{m''n''} \bar{\bar{F}}_{mnm''n''}(r)\begin{pmatrix} a_{m''n''} \\ b_{m''n''} \end{pmatrix} \tag{3.26}$$

$$\vec{F}_{m'n'}(r) = \sum_{m''n''} \bar{\bar{F}}_{m'n'm''n''}(r)\begin{pmatrix} a_{m''n''} \\ b_{m''n''} \end{pmatrix} \tag{3.27}$$

Insert into Eq.3.25,

$$\sum_{m''n''} \bar{\bar{F}}_{mnm''n''}(r)\begin{pmatrix} a_{m''n''} \\ b_{m''n''} \end{pmatrix} = \sum_{m''n''} \bar{\bar{U}}_{mnm''n''}(r)\bar{\bar{J}}_{n''}(r)\begin{pmatrix} a_{m''n''} \\ b_{m''n''} \end{pmatrix} + \sum_{m'n'} \bar{\bar{U}}_{mnm'n'}(r)\int_0^R dr'\,\bar{\bar{g}}_{n'}(r,r') \sum_{m''n''} \bar{\bar{F}}_{m'n'm''n''}(r)\begin{pmatrix} a_{m''n''} \\ b_{m''n''} \end{pmatrix} \tag{3.28}$$

Equate linear independent terms indexed with $m''n''$,

$$\bar{\bar{F}}_{mnm''n''}(r) = \bar{\bar{U}}_{mnm''n''}(r)\bar{\bar{J}}_{n''}(r) + \sum_{m'n'} \bar{\bar{U}}_{mnm'n'}(r) \int_0^R dr' \bar{\bar{g}}_{n'}(r,r') \bar{\bar{F}}_{m'n'm''n''}(r) \tag{3.29}$$

Eq.3.29 is one of the formulas needed for constructing the recurrence relation for the T-matrix. Now, we derive an explicit formula for the T-matrix. First, write Eq.3.18 for the scattered field,

$$\begin{aligned} &\vec{E}_s(\vec{r}) \\ &= \iiint_V r'^2 sin\theta' dr' d\theta' d\varphi' \, \chi(\overrightarrow{r'}) \sum_{n=1}^{\infty} \sum_{m=-n}^{n} \bar{\bar{Y}}_{mn}(\theta,\varphi) \, \bar{\bar{g}}_n(r,r') \bar{\bar{Y}}^{T*}_{mn}(\theta',\varphi') \\ &\cdot \bar{\bar{Z}}(\vec{r}') \cdot \vec{E}(\overrightarrow{r'}), \end{aligned} \tag{3.30}$$

For $r>R>r'$, we have according to Eq.3.17,

$$\bar{\bar{g}}_n(r,r') = ik\bar{\bar{H}}_n(r)\bar{\bar{J}}^T_n(r') \tag{3.31}$$

Eq.3.30 becomes,

$$\vec{E}_s(\vec{r}) = \iiint_V r'^2 sin\theta' dr' d\theta' d\varphi' \, \chi(\overrightarrow{r'}) \times$$
$$\sum_{n=1}^{\infty} \sum_{m=-n}^{n} \bar{\bar{Y}}_{mn}(\theta, \varphi) \, ik \bar{\bar{H}}_n(r) \bar{\bar{J}}_n^T(r') \bar{\bar{Y}}_{mn}^{T*}(\theta', \varphi') \bar{\bar{Z}}(\vec{r}') \cdot \vec{E}(\overrightarrow{r'}), \tag{3.32}$$

Relating this to Eq.3.2, we have,

$$\vec{E}_s(\vec{r}) = \sum_{n=1}^{\infty} \sum_{m=-n}^{n} \bar{\bar{Y}}_{mn}(\theta, \varphi) \bar{\bar{H}}_n(r) \iiint_V r'^2 sin\theta' dr' d\theta' d\varphi' \, \chi(\overrightarrow{r'}) \times$$
$$ik \bar{\bar{J}}_n^T(r') \bar{\bar{Y}}_{mn}^{T*}(\theta', \varphi') \bar{\bar{Z}}(\vec{r}') \cdot \vec{E}(\overrightarrow{r'}) \tag{3.33}$$
$$= \sum_{n=1}^{\infty} \sum_{m=-n}^{n} \bar{\bar{Y}}_{mn}(\theta, \varphi) \bar{\bar{H}}_n(r) \begin{pmatrix} p_{mn} \\ q_{mn} \end{pmatrix}$$

$$\begin{pmatrix} p_{mn} \\ q_{mn} \end{pmatrix} = \iiint_V r'^2 sin\theta' dr' d\theta' d\varphi' \, \chi(\overrightarrow{r'}) ik \bar{\bar{J}}_n^T(r') \bar{\bar{Y}}_{mn}^{T*}(\theta', \varphi') \bar{\bar{Z}}(\vec{r}') \tag{3.34}$$
$$\cdot \vec{E}(\overrightarrow{r'})$$

Connecting Eq.3.34 with $\begin{pmatrix} a_{mn} \\ b_{mn} \end{pmatrix}$, we have,

$$\begin{pmatrix} p_{mn} \\ q_{mn} \end{pmatrix}$$

$$= \iiint_V r'^2 sin\theta' dr' d\theta' d\varphi' \, \chi(\overrightarrow{r'}) ik \bar{\bar{J}}_n^T(r') \bar{\bar{Y}}_{mn}^{T*}(\theta', \varphi') \bar{\bar{Z}}(\vec{r}') \cdot \vec{E}(\overrightarrow{r'})$$

$$= ik \int_0^R dr' \, r'^2 \bar{\bar{J}}_n^T(r') \int_\Omega sin\theta' d\theta' d\varphi' \, \bar{\bar{Y}}_{mn}^{T*}(\theta', \varphi') \chi(\overrightarrow{r'}) \bar{\bar{Z}}(\vec{r}') \cdot \vec{E}(\overrightarrow{r'})$$

$$= ik \int_0^R dr' \, \bar{\bar{J}}_n^T(r') \vec{F}_{mn}(r') \tag{3.35}$$

$$= ik \int_0^R dr' \, \bar{\bar{J}}_n^T(r') \sum_{m''n''} \bar{\bar{F}}_{mnm''n''}(r') \begin{pmatrix} a_{m''n''} \\ b_{m''n''} \end{pmatrix}$$

$$= \sum_{m''n''} \left[ik \int_0^R dr' \, \bar{\bar{J}}_n^T(r') \bar{\bar{F}}_{mnm''n''}(r') \right] \begin{pmatrix} a_{m''n''} \\ b_{m''n''} \end{pmatrix}$$

So, comparing with Eq.3.9, we have,

$$\bar{\bar{T}}_{mnm''n''}(R) = ik \int_0^R dr' \, \bar{\bar{J}}_n^T(r') \bar{\bar{F}}_{mnm''n''}(r') \tag{3.36}$$

Eq.3.29 and 3.36 are the ingredients to derive a recurrence relation for the T-matrix, group the expressions for $\bar{\bar{T}}_{mnm''n''}(R)$ and $\bar{\bar{F}}_{mnm''n''}(r)$ together,

$$\bar{\bar{T}}_{mnm''n''}(R) = ik \int_0^R dr' \bar{\bar{J}}_n^T(r') \bar{\bar{F}}_{mnm''n''}(r') \tag{3.37}$$

$$\begin{aligned} \bar{\bar{F}}_{mnm''n''}(r) = {} & \bar{\bar{U}}_{mnm''n''}(r) \bar{\bar{J}}_{n''}(r) \\ & + \sum_{m'n'} \bar{\bar{U}}_{mnm'n'}(r) \int_0^R dr' \bar{\bar{g}}_{n'}(r,r') \bar{\bar{F}}_{m'n'm''n''}(r) \end{aligned} \tag{3.38}$$

Define the following super matrices, where each matrix element is a matrix,

$$\begin{gathered} \boldsymbol{T} = \left[\bar{\bar{T}}_{mnm''n''}\right], \boldsymbol{U} = \left[\bar{\bar{U}}_{mnm''n''}\right], \boldsymbol{F} = \left[\bar{\bar{F}}_{mnm''n''}\right], \\ \boldsymbol{J} = \left[\bar{\bar{J}}_{n''} \delta_{nn''} \delta_{mm''}\right], \boldsymbol{H} = \left[\bar{\bar{H}}_{n''} \delta_{nn''} \delta_{mm''}\right], \\ \boldsymbol{g} = \left[\bar{\bar{g}}_{n''} \delta_{nn''} \delta_{mm''}\right], \boldsymbol{J^T} = \left[\bar{\bar{J}}_{n''}^T \delta_{nn''} \delta_{mm''}\right]^T \end{gathered} \tag{3.39}$$

Rewrite Eq.3.37 and 3.38 in condensed form using these super matrices,

$$\boldsymbol{T}(R) = ik \int_0^R dr' \boldsymbol{J^T}(r') \boldsymbol{F}(r', R) \tag{3.40}$$

$$\boldsymbol{F}(r, R) = \boldsymbol{U}(r) \boldsymbol{J}(r) + \int_0^R dr' \boldsymbol{U}(r) \boldsymbol{g}(r, r') \boldsymbol{F}(r', R) \tag{3.41}$$

$$\boldsymbol{g}(r,r') = \begin{cases} ik\boldsymbol{H}(r)\boldsymbol{J}^{\boldsymbol{T}}(r'), & r > r' \\ \dfrac{ik}{2}[\boldsymbol{H}(r)\boldsymbol{J}^{\boldsymbol{T}}(r') + \boldsymbol{J}(r)\boldsymbol{H}^{\boldsymbol{T}}(r')], & r = r' \\ ik\boldsymbol{J}(r)\boldsymbol{H}^{\boldsymbol{T}}(r'), & r < r' \end{cases} \tag{3.42}$$

Now we begin deriving a recurrence relation for $\boldsymbol{T}(R)$. Consider first $\boldsymbol{F}(R,R)$ since it will be used many times in the derivation,

$$\begin{aligned} \boldsymbol{F}(R,R) &= \boldsymbol{U}(R)\boldsymbol{J}(R) + \int_0^R dr'\, \boldsymbol{U}(R)\boldsymbol{g}(R,r')\boldsymbol{F}(r',R) \\ &= \int_0^{R-\Delta R} dr'\, \boldsymbol{U}(R)\boldsymbol{g}(R,r')\boldsymbol{F}(r',R) \\ &\quad + \Delta R\boldsymbol{U}(R)\boldsymbol{g}(R,R)\boldsymbol{F}(R,R) \\ &= \int_0^{R-\Delta R} dr'\, \boldsymbol{U}(R)ik\boldsymbol{H}(R)\boldsymbol{J}^{\boldsymbol{T}}(r')\boldsymbol{F}(r',R) \\ &\quad + \Delta R\boldsymbol{U}(R)\boldsymbol{g}(R,R)\boldsymbol{F}(R,R) \end{aligned} \tag{3.43}$$

Group $\boldsymbol{F}(R,R)$ together,

$$\begin{aligned} &[\boldsymbol{I} - \Delta R\boldsymbol{U}(R)\boldsymbol{g}(R,R)]\boldsymbol{F}(R,R) \\ &\quad = \boldsymbol{U}(R)\boldsymbol{J}(R) + ik\boldsymbol{U}(R)\boldsymbol{H}(R)\int_0^{R-\Delta R} dr'\, \boldsymbol{J}^{\boldsymbol{T}}(r')\boldsymbol{F}(r',R) \end{aligned} \tag{3.44}$$

$$\boldsymbol{F}(R,R) = [\boldsymbol{I} - \Delta R\boldsymbol{U}(R)\boldsymbol{g}(R,R)]^{-1}\boldsymbol{U}(R)\left[\boldsymbol{J}(R) + ik\boldsymbol{H}(R)\int_0^{R-\Delta R} dr'\,\boldsymbol{J}^{\boldsymbol{T}}(r')\boldsymbol{F}(r',R)\right]$$
$$= \frac{1}{\Delta R}\boldsymbol{Q}(R)[\boldsymbol{J}(R) + \boldsymbol{H}(R)\boldsymbol{q}(R)] \tag{3.45}$$

Where $\boldsymbol{Q}(R)$ and $\boldsymbol{q}(R)$ are given by the following relationships,

$$\boldsymbol{Q}(R) = \Delta R[\boldsymbol{I} - \Delta R\boldsymbol{U}(R)\boldsymbol{g}(R,R)]^{-1}\boldsymbol{U}(R) \tag{3.46}$$

$$\boldsymbol{q}(R) = ik\int_0^{R-\Delta R} dr'\,\boldsymbol{J}^{\boldsymbol{T}}(r')\boldsymbol{F}(r',R) \tag{3.47}$$

discretize $\boldsymbol{T}(R)$,

$$\boldsymbol{T}(R) = ik\int_0^{R-\Delta R} dr'\,\boldsymbol{J}^{\boldsymbol{T}}(r')\boldsymbol{F}(r',R) + ik\Delta R\boldsymbol{J}^{\boldsymbol{T}}(R)\boldsymbol{F}(R,R)$$
$$= \boldsymbol{q}(R) + ik\Delta R\boldsymbol{J}^{\boldsymbol{T}}(R)\frac{1}{\Delta R}\boldsymbol{Q}(R)[\boldsymbol{J}(R) + \boldsymbol{H}(R)\boldsymbol{q}(R)]$$
$$= ik\boldsymbol{J}^{\boldsymbol{T}}(R)\boldsymbol{Q}(R)\boldsymbol{J}(R) + \boldsymbol{q}(R) + ik\boldsymbol{J}^{\boldsymbol{T}}(R)\boldsymbol{Q}(R)\boldsymbol{H}(R)\boldsymbol{q}(R) \tag{3.48}$$
$$= ik\boldsymbol{J}^{\boldsymbol{T}}(R)\boldsymbol{Q}(R)\boldsymbol{J}(R) + [\boldsymbol{I} + ik\boldsymbol{J}^{\boldsymbol{T}}(R)\boldsymbol{Q}(R)\boldsymbol{H}(R)]\boldsymbol{q}(R)$$
$$= \boldsymbol{Q}_{11}(R) + [\boldsymbol{I} + \boldsymbol{Q}_{12}(R)]\boldsymbol{q}(R)$$

where $\boldsymbol{Q}_{11}(R)$ and $\boldsymbol{Q}_{12}(R)$ are given by,

$$\boldsymbol{Q}_{11}(R) = ik\boldsymbol{J}^{\boldsymbol{T}}(R)\boldsymbol{Q}(R)\boldsymbol{J}(R) \tag{3.49}$$

$$\boldsymbol{Q}_{12}(R) = ik\boldsymbol{J}^{\boldsymbol{T}}(R)\boldsymbol{Q}(R)\boldsymbol{H}(R) \tag{3.50}$$

To form a recurrence for $\boldsymbol{T}(R)$, we need to connect $\boldsymbol{q}(R)$ in Eq.3.48 with $\boldsymbol{T}(R - \Delta R)$, from Eq.3.40,

$$\boldsymbol{T}(R - \Delta R) = ik \int_0^{R-\Delta R} dr'\, \boldsymbol{J}^{\boldsymbol{T}}(r')\boldsymbol{F}(r', R - \Delta R) \tag{3.51}$$

and,

$$\boldsymbol{q}(R) = ik \int_0^{R-\Delta R} dr'\, \boldsymbol{J}^{\boldsymbol{T}}(r')\boldsymbol{F}(r', R) \tag{3.52}$$

For $\boldsymbol{F}(r', R)$, we have,

$$
\begin{aligned}
\boldsymbol{F}(r,R) &= \boldsymbol{U}(r)\boldsymbol{J}(r) + \int_0^R dr'\, \boldsymbol{U}(r)\boldsymbol{g}(r,r')\boldsymbol{F}(r',R) \\
&= \boldsymbol{U}(r)\boldsymbol{J}(r) + \int_0^{R-\Delta R} dr'\, \boldsymbol{U}(r)\boldsymbol{g}(r,r')\boldsymbol{F}(r',R) \\
&+ \Delta R\boldsymbol{U}(r)\boldsymbol{g}(r,R)\boldsymbol{F}(R,R) \\
&= \boldsymbol{U}(r)\boldsymbol{J}(r) + \int_0^{R-\Delta R} dr'\, \boldsymbol{U}(r)\boldsymbol{g}(r,r')\boldsymbol{F}(r',R) \\
&+ \Delta R\boldsymbol{U}(r)ik\boldsymbol{J}(r)\boldsymbol{H}^{\boldsymbol{T}}(R)\boldsymbol{F}(R,R) \\
&= \boldsymbol{U}(r)\boldsymbol{J}(r)\,[\boldsymbol{I} + ik\Delta R\boldsymbol{H}^{\boldsymbol{T}}(R)\boldsymbol{F}(R,R)] \\
&+ \int_0^{R-\Delta R} dr'\, \boldsymbol{U}(r)\boldsymbol{g}(r,r')\boldsymbol{F}(r',R) \\
&= \boldsymbol{U}(r)\boldsymbol{J}(r)[\boldsymbol{I} + \boldsymbol{P}(R)] + \int_0^{R-\Delta R} dr'\, \boldsymbol{U}(r)\boldsymbol{g}(r,r')\boldsymbol{F}(r',R)
\end{aligned}
\tag{3.53}
$$

where

$$
\boldsymbol{p}(R) = ik\Delta R\boldsymbol{H}^{\boldsymbol{T}}(R)\boldsymbol{F}(R,R) \tag{3.54}
$$

Compare Eq.3.53 with $\boldsymbol{F}(r', R-\Delta R)$,

$$
\boldsymbol{F}(r,R-\Delta R) = \boldsymbol{U}(r)\boldsymbol{J}(r) + \int_0^{R-\Delta R} dr'\, \boldsymbol{U}(r)\boldsymbol{g}(r,r')\boldsymbol{F}(r',R-\Delta R) \tag{3.55}
$$

$\boldsymbol{F}(r,R)$ and $\boldsymbol{F}(r,R-\Delta R)$ solve the same Fredholm integral equation, but with different forcing functions $\boldsymbol{U}(r)\boldsymbol{J}(r)[\boldsymbol{I}+\boldsymbol{P}(R)]$ and $\boldsymbol{U}(r)\boldsymbol{J}(r)$, so

$$\boldsymbol{F}(r,R)=\boldsymbol{F}(r,R-\Delta R)[\boldsymbol{I}+\boldsymbol{p}(R)] \tag{3.56}$$

This relation should be valid for small values of *R* (the circumscribing sphere radius). We multiply Eq.3.51 by $[\boldsymbol{I}+\boldsymbol{P}(R)]$,

$$\begin{aligned}\boldsymbol{T}(R-\Delta R)[\boldsymbol{I}+\boldsymbol{p}(R)] &= ik\int_0^{R-\Delta R} dr'\,\boldsymbol{J}^{\boldsymbol{T}}(r')\boldsymbol{F}(r',R-\Delta R)[\boldsymbol{I}+\boldsymbol{P}(R)] \\ &= ik\int_0^{R-\Delta R} dr'\,\boldsymbol{J}^{\boldsymbol{T}}(r')\boldsymbol{F}(r',R)=\boldsymbol{q}(R)\end{aligned} \tag{3.57}$$

Furthermore,

$$\begin{aligned}\boldsymbol{p}(R) &= ik\Delta R\boldsymbol{H}^{\boldsymbol{T}}(R)\boldsymbol{F}(R,R) \\ &= ik\Delta R\boldsymbol{H}^{\boldsymbol{T}}(R)\frac{1}{\Delta R}\boldsymbol{Q}(R)[\boldsymbol{J}(R)+\boldsymbol{H}(R)\boldsymbol{q}(R)] \\ &= ik\boldsymbol{H}^{\boldsymbol{T}}(R)\boldsymbol{Q}(R)[\boldsymbol{J}(R)+\boldsymbol{H}(R)\boldsymbol{q}(R)] \\ &= ik\boldsymbol{H}^{\boldsymbol{T}}(R)\boldsymbol{Q}(R)\boldsymbol{J}(R)+ik\boldsymbol{H}^{\boldsymbol{T}}(R)\boldsymbol{Q}(R)\boldsymbol{H}(R)\boldsymbol{q}(R) \\ &= \boldsymbol{Q_{21}}(R)+\boldsymbol{Q_{22}}(R)\boldsymbol{q}(R)\end{aligned} \tag{3.58}$$

where,

$$\boldsymbol{Q_{21}}(R) = ik\boldsymbol{H^T}(R)\boldsymbol{Q}(R)\boldsymbol{J}(R) \tag{3.59}$$

$$\boldsymbol{Q_{22}}(R) = ik\boldsymbol{H^T}(R)\boldsymbol{Q}(R)\boldsymbol{H}(R) \tag{3.60}$$

Combine Eq.3.57 and 3.58 to solve for $\boldsymbol{q}(R)$,

$$\boldsymbol{q}(R) = [\boldsymbol{I} - \boldsymbol{T}(R - \Delta R)\boldsymbol{Q}_{22}(R)]^{-1}\boldsymbol{T}(R - \Delta R)[\boldsymbol{I} + \boldsymbol{Q}_{21}(R)] \tag{3.61}$$

Finally, insert 3.61 into Eq.3.48:

$$\begin{aligned}\boldsymbol{T}(R) = \boldsymbol{Q}_{11}(R) \\ + [\boldsymbol{I} + \boldsymbol{Q}_{12}(R)][\boldsymbol{I} - \boldsymbol{T}(R - \Delta R)\boldsymbol{Q}_{22}(R)]^{-1}\boldsymbol{T}(R - \Delta R)[\boldsymbol{I} \\ + \boldsymbol{Q}_{21}(R)]\end{aligned} \tag{3.62}$$

This is the radial recurrence relation for the T-matrix in the II-TM method.

Fig.3.1 illustrates the radial recurrence. The T-matrix $\boldsymbol{T}(r_0)$ of the inscribed sphere with radius r_0 is the initial T-matrix to start the recurrence [22]. The recurrence ends at the circumscribing sphere of the particle.

We show comparisons between II-TM and two benchmark single scattering methods, the Lorenz-Mie theory for homogeneous spheres and the Extended Boundary Condition Method (EBCM) [6] for spheroids.

According to previous chapters, three parameters control the accuracy of the II-TM method: the truncation order of the T-matrix *N,* the radial discretization Δr of the recurrence and the number of quadrature nodes N_q for the surface integrations in the U-matrix elements.

The first comparison is for a sphere and the two methods are Lorenz-Mie theory and the II-TM method, the initial radius of the recurrence R_0 is selected to be half the radius of the sphere R , and the radial resolution for the recurrence is $\Delta r = 0.005 * (R - R_0)$. The T-matrix truncation order for the Lorenz-Mie theory is given by Wiscombe [23],

$$N = x + 4.05x^{1/3} + 2, \tag{3.63}$$

In the II-TM method, we use the same truncation order. In later chapters we will elaborate on the choice of the number of quadrature nodes N_q. In these comparison test runs, $N_q = 100$. Since the integrands in the surface integrations in the case of a sphere (or spheroid) are simply products of polynomials, a low N_q is enough for high precision quadrature.

In Figs. 3.2(no absorption) and 3.3(with absorption), good agreement is achieved between the Lorenz-Mie theory and the II-TM method for sphere.

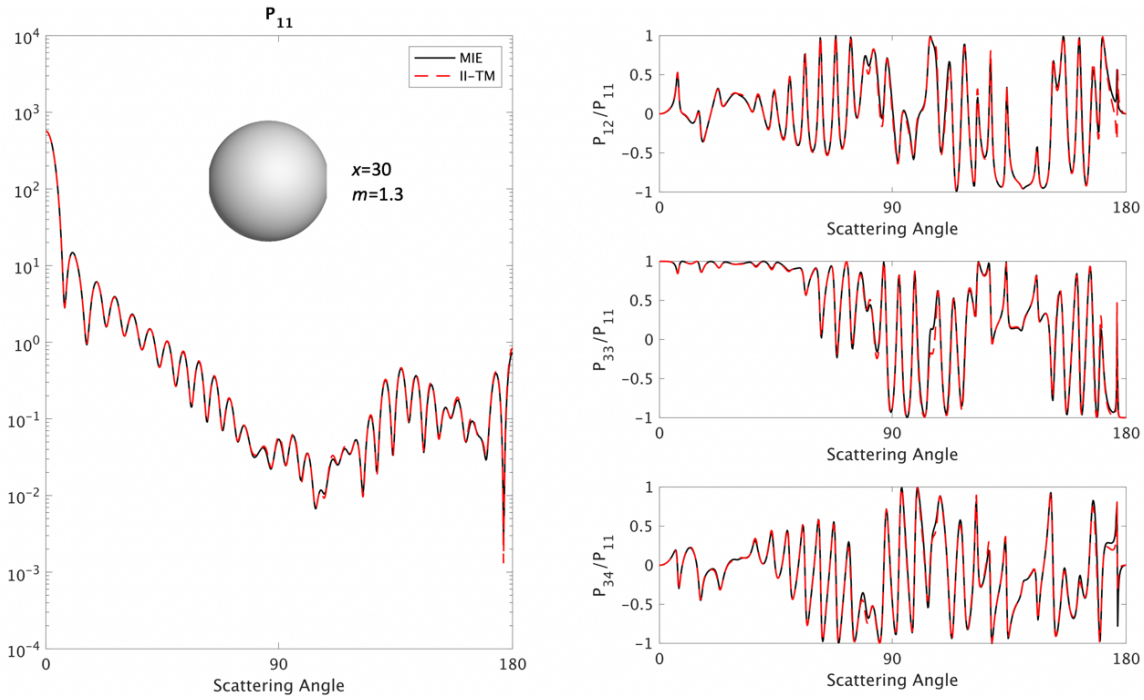

Figure 3.2 Comparison between II-TM and the Lorenz-Mie theory. Sphere is indicated in the figure, size parameter x=30 at incident wavelength 550nm, refractive index is 1.3.

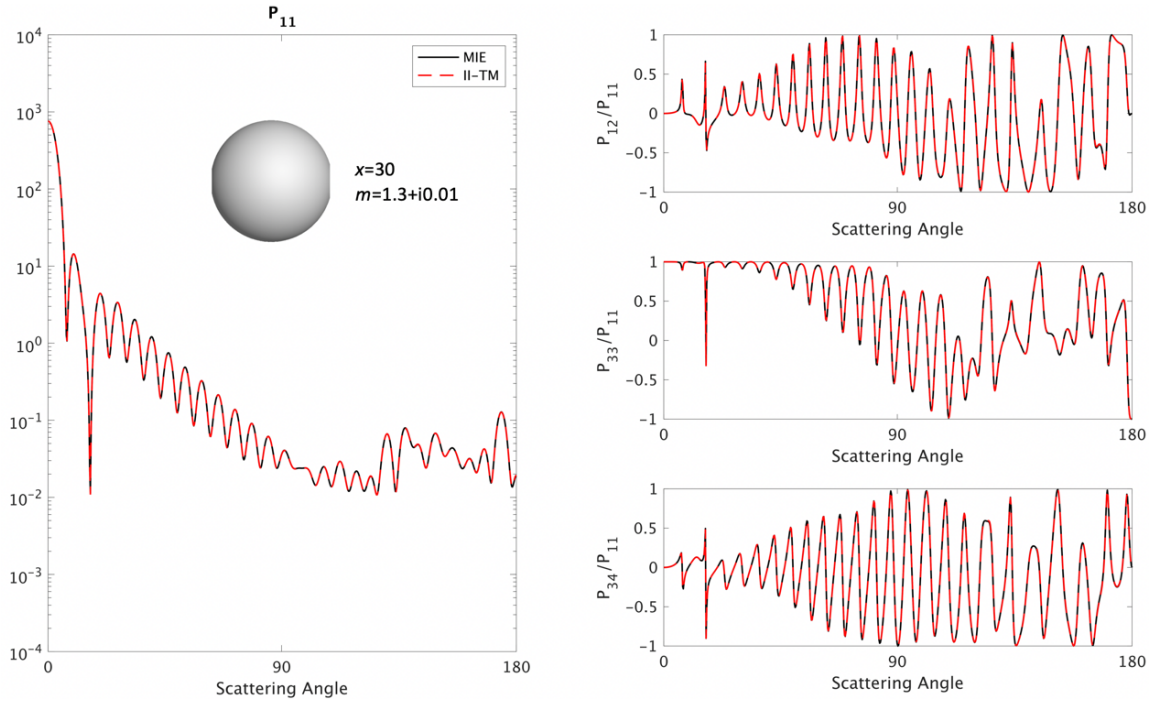

Figure 3.3 Comparison between II-TM and the Lorenz-Mie theory. Sphere is indicated in the figure, size parameter x=30 at incident wavelength 550nm, refractive index is 1.3+i0.01.

The second comparison is for a spheroid and the two methods are EBCM and II-TM. Unlike the II-TM method where the T-matrix is obtained with a radial recurrence in terms of a family of concentric spherical shells centered on the particle center, EBCM solves for the T-matrix with a direct matrix inversion obtained from a surface integral equation for the electric field surrounding the particle. Both methods are numerically exact methods in that they accurately solve the Maxwell's equations. The same truncation order is used for EBCM and II-TM. Good agreement can be achieved in Figs.3.4~5.

At large size parameters, comparison between the II-TM and PGOM method for hexagonal column is shown in Fig.3.6 and 3.7. The PGOM (physical geometric optics method) is a geometric optics method which is only accurate for large particles[14]. In the PGOM method, the near field is obtained by tracing the reflection and refraction of the light beam impinging on multiple facets. The far field is obtained via a near-to-far field transformation. The agreement between II-TM and PGOM is very good.

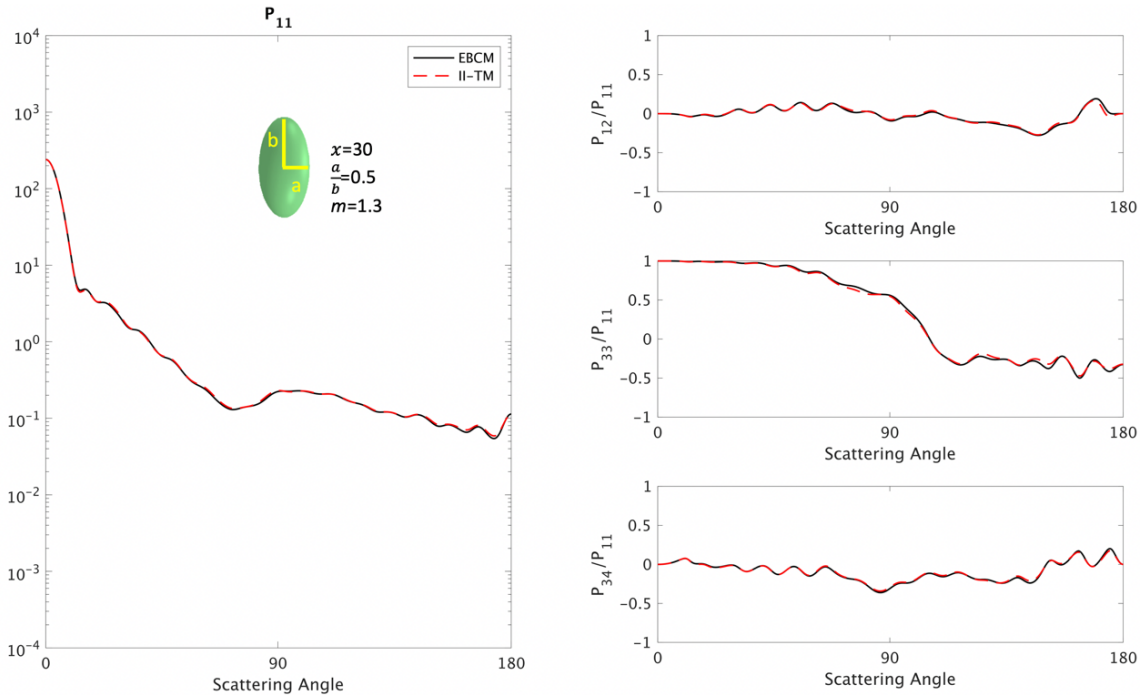

Figure 3.4 Comparison between II-TM and the EBCM method. Spheroid is indicated in the figure, size parameter x=30 at incident wavelength 550nm, aspect ratio=0.5, refractive index is 1.3.

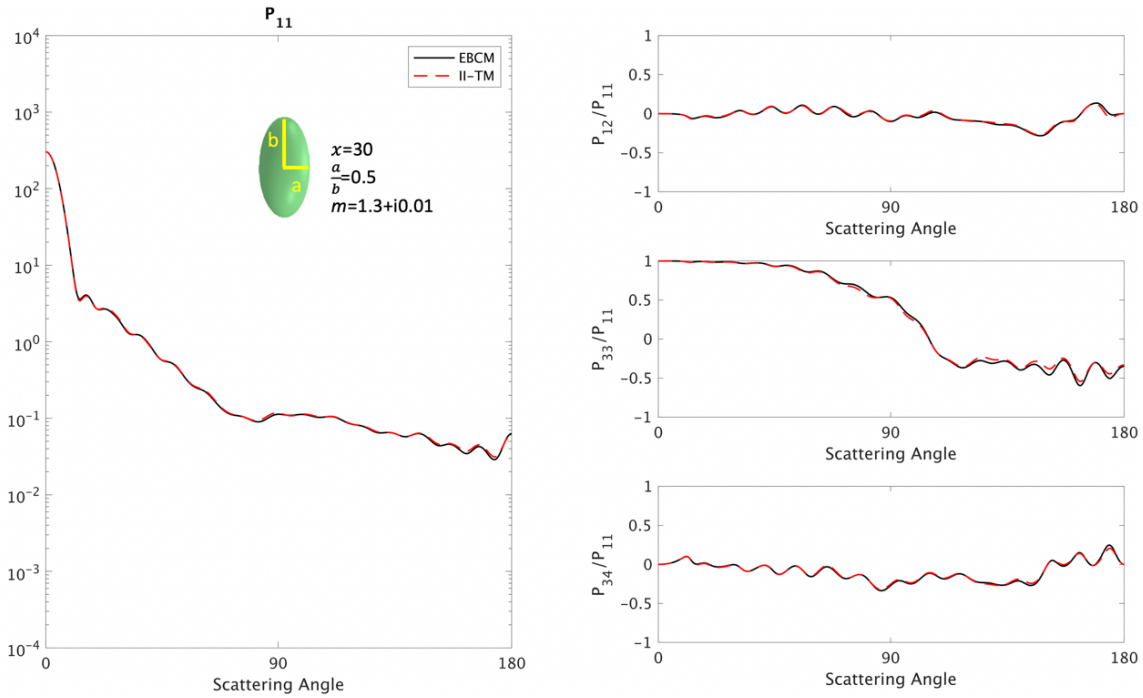

Figure 3.5 Comparison between II-TM and the EBCM method. Spheroid is indicated in the figure, size parameter x=30 at incident wavelength 550nm, aspect ratio=0.5, refractive index is 1.3+i0.01.

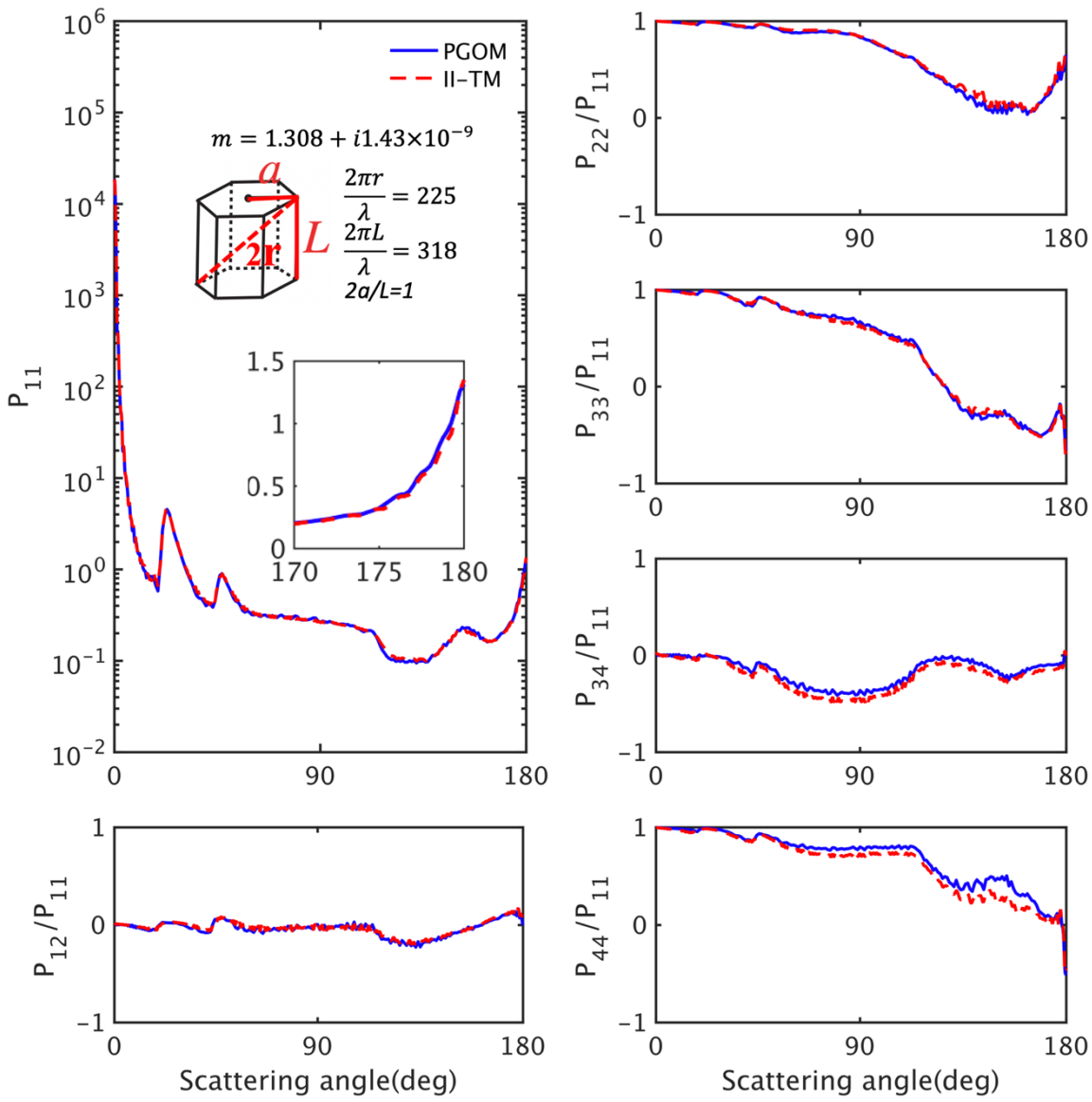

Figure 3.6 Comparison between II-TM and the PGOM method. Hexagonal column is indicated in the figure, size parameter x=225 defined with the circumscribing sphere radius. Refractive index m=1.308+i1.43 × 10^{-9}. This corresponds to ice refractive index at 650 nm wavelength.

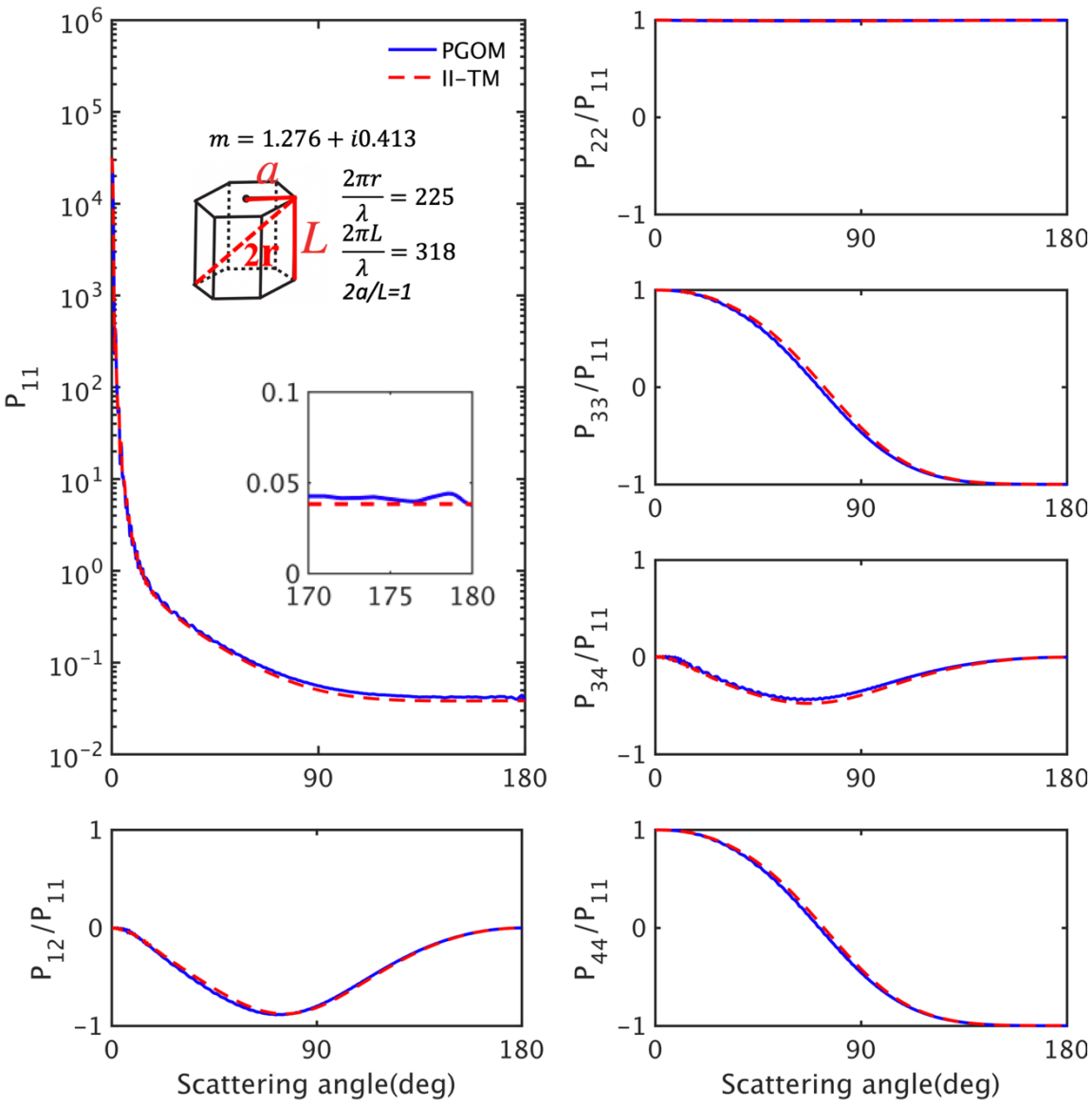

Figure 3.7 Comparison between II-TM and the PGOM method. Hexagonal column is indicated in the figure, size parameter x=225 defined with the circumscribing sphere radius. Refractive index m=1.276+i0.413. This corresponds to ice refractive index at 120 μm wavelength.

3.2. Improving the surface integrations in U-matrix elements

In this section we investigate and improve the precision of the II-TM method. Specifically, we look at the II-TM surface integrations in the U-matrix elements (Eq.3.24), which is repeated here:

$$\bar{\bar{U}}_{mnm'n'}(r) = r^2 \int_{\Omega} sin\theta d\theta d\varphi \, \bar{\bar{Y}}^{T*}_{mn}(\theta,\varphi)\chi(\vec{r})\bar{\bar{Z}}(r,\theta,\varphi)\bar{\bar{Y}}_{m'n'}(\theta,\varphi) \qquad (3.64)$$

The matrix elements of the U-matrix $\bar{\bar{U}}(r)$ in each iteration are surface integrals in zenith and azimuth directions on the spherical shell. The five nonzero elements in the U-matrix can be written as [22],

$$U^{ij}_{mnm'n'} = A_{mnm'n'} \int_0^{\pi} d\theta sin\theta \, F_{mm'}(r,\theta) K^{ij}_{mnm'n'}(\theta), \quad i,j = 1,2 \qquad (3.65)$$

$$U^{33}_{mnm'n'} = \tilde{A}_{mnm'n'} \int_0^{\pi} d\theta sin\theta \, \tilde{F}_{mm'}(r,\theta) d^{n}_{0m}(\theta) d^{n'}_{0m'}(\theta), \qquad (3.66)$$

where,

$$F_{mm'}(r,\theta) = \int_0^{2\pi} d\varphi \, e^{-i(m-m')\varphi} [\varepsilon(r,\theta,\varphi) - 1], \qquad (3.67)$$

$$\tilde{F}_{mm'}(r,\theta) = \int_0^{2\pi} d\varphi \, e^{-i(m-m')\varphi} \frac{[\varepsilon(r,\theta,\varphi) - 1]}{\varepsilon(r,\theta,\varphi)}, \qquad (3.68)$$

$$A_{mnm'n'} = (kr)^2(-1)^{m+m'}\left[\frac{2n+1}{4\pi n(n+1)}\right]^{\frac{1}{2}}\left[\frac{2n'+1}{4\pi n'(n'+1)}\right]^{\frac{1}{2}}, \tag{3.69}$$

$$\tilde{A}_{mnm'n'} = \sqrt{nn'(n+1)(n'+1)}A_{mnm'n'}, \tag{3.70}$$

$$\begin{aligned}&\left[K^{ij}_{mnm'n'}(\theta)\right]\\ &= \begin{bmatrix} \pi_{mn}(\theta)\pi_{m'n'}(\theta) + \tau_{mn}(\theta)\tau_{m'n'}(\theta) & -i[\pi_{mn}(\theta)\tau_{m'n'}(\theta) + \tau_{mn}(\theta)\pi_{m'n'}(\theta)] \\ i[\pi_{mn}(\theta)\tau_{m'n'}(\theta) + \tau_{mn}(\theta)\pi_{m'n'}(\theta)] & \pi_{mn}(\theta)\pi_{m'n'}(\theta) + \tau_{mn}(\theta)\tau_{m'n'}(\theta) \end{bmatrix},\end{aligned} \tag{3.71}$$

and π_{mn} and τ_{mn} are given by,

$$\pi_{mn}(\theta) = \frac{m}{sin\theta}\, d^n_{0m}(\theta), \tag{3.72}$$

$$\tau_{mn}(\theta) = \frac{d}{d\theta}\, d^n_{0m}(\theta). \tag{3.73}$$

In Eqs.3.66, 3.72 and 3.73, $d^n_{0m}(\theta)$ is the Wigner-d function. The U-matrix elements are different for different particles. We outline the formulations for a spheroid and a regular hexagonal column. These particle geometries are selected to represent particles with continuous and discrete symmetries. In particular, a spheroid has both rotational and mirror symmetry so the formulation is relatively simple, and a hexagonal column has mirror symmetry and 6-fold symmetry.

A spheroid has rotational symmetry with respect to the z-axis ($\varepsilon(r,\theta,\varphi) = \varepsilon(r,\theta)$) and mirror symmetry with respect to the xy-plane ($\varepsilon(r,\theta) = \varepsilon(r,\pi-\theta)$). Also,

$$[\varepsilon(r,\theta)-1] = \begin{cases} 0, & \theta > \theta_2 \\ [\varepsilon-1], & \theta \in [0,\theta_2] \end{cases}, \tag{3.74}$$

and θ_2 is the angle at which the spherical shell intersects the spheroid (Fig.3.8).

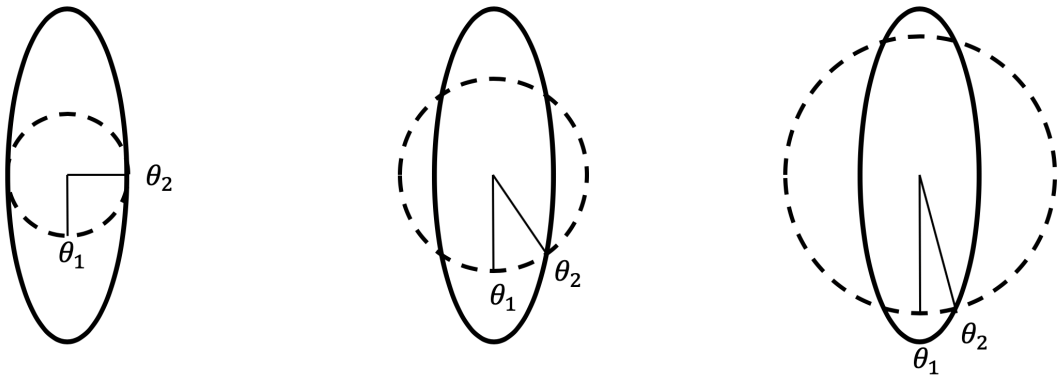

Figure 3.8 Progression of the spherical shell on a spheroid. In this case, $\boldsymbol{\theta_1 = 0}$. and $\boldsymbol{\theta_2}$ is the angle where the spherical shell intersects the spheroid.

The properties of the Wigner-d functions allow us to greatly simplify the formulations [24]:

$$\begin{aligned} &[\pi_{mn}(\theta)\pi_{mn'}(\theta) + \tau_{mn}(\theta)\tau_{mn'}(\theta)]sin\theta \\ &= \begin{cases} \dfrac{d}{d\theta}(\tau_{mn'}d^{n}_{0m}(\theta)sin\theta) + n'(n'+1)sin\theta d^{n}_{0m}(\theta)d^{n'}_{0m}(\theta) \\ \dfrac{d}{d\theta}(\tau_{mn}d^{n'}_{0m}(\theta)sin\theta) + n(n+1)sin\theta d^{n}_{0m}(\theta)d^{n'}_{0m}(\theta) \end{cases}, \end{aligned} \tag{3.75}$$

$$[\pi_{mn}(\theta)\tau_{mn'}(\theta)+\tau_{mn}(\theta)\pi_{mn'}(\theta)]sin\theta = m\frac{d}{d\theta}\Big(d_{0m}^{n}(\theta)d_{0m}^{n'}(\theta)\Big), \quad (3.76)$$

Substituting Eqs.3.75 and 3.76 into Eqs.3.65 and 3.66 and integrating by parts, we obtain the simplified formulations:

$$\begin{aligned} U_{mnm'n'}^{11}(r) &= U_{mnm'n'}^{22}(r) \\ &= A_{mnm'n'}2\pi\delta_{mm'}[\varepsilon-1]\Big[c_{nn'}\tau_{mn'}(\theta_2)d_{0m}^{n}(\theta_2)sin\theta_2 \\ &+ n'(n'+1)\int_0^{\theta_2} d\theta\, sin\theta\, d_{0m}^{n}(\theta)d_{0m}^{n'}(\theta)\Big], \\ c_{nn'} &= 1+(-1)^{n+n'}, \end{aligned} \quad (3.77)$$

$$\begin{aligned} &U_{mnm'n'}^{33}(r) \\ &= \tilde{A}_{mnm'n'}2\pi\delta_{mm'}\frac{[\varepsilon-1]}{\varepsilon}c_{nn'}\int_0^{\theta_2} d\theta sin\theta\, d_{0m}^{n}(\theta)d_{0m'}^{n'}(\theta), \end{aligned} \quad (3.78)$$

$$\begin{aligned} U_{mnm'n'}^{12}(r) &= -U_{mnm'n'}^{21}(r) \\ &= A_{mnm'n'}2\pi\delta_{mm'}[\varepsilon-1]\tilde{c}_{nn'}(-im)\big[\, d_{0m}^{n}(\theta_2)d_{0m}^{n'}(\theta_2) \\ &- d_{0m}^{n}(0)d_{0m}^{n'}(0)\big], \qquad \tilde{c}_{nn'} = 1+(-1)^{n+n'+1}. \end{aligned} \quad (3.79)$$

The original integrals in the zenith direction in Eqs. 3.65 and 3.66 are now reduced to $\int_0^{\theta_2} d\theta\, sin\theta\, d_{0m}^{n}(\theta)d_{0m}^{n'}(\theta)$ in Eqs.3.77 and 3.78.

In the case of a hexagonal column, without a rotational symmetry with respect to the z-axis, the azimuth integrals $F_{mm'}(r,\theta)$ and $\tilde{F}_{mm'}(r,\theta)$ cannot be decoupled from the

zenith integrals. Fig.3.9 illustrates the 3 different situations as the recurrence progresses in the case of a long column. The values of the azimuth integrals are dependent on θ and r because the spherical shell intersects with the hexagonal column in different ways as θ and r change.

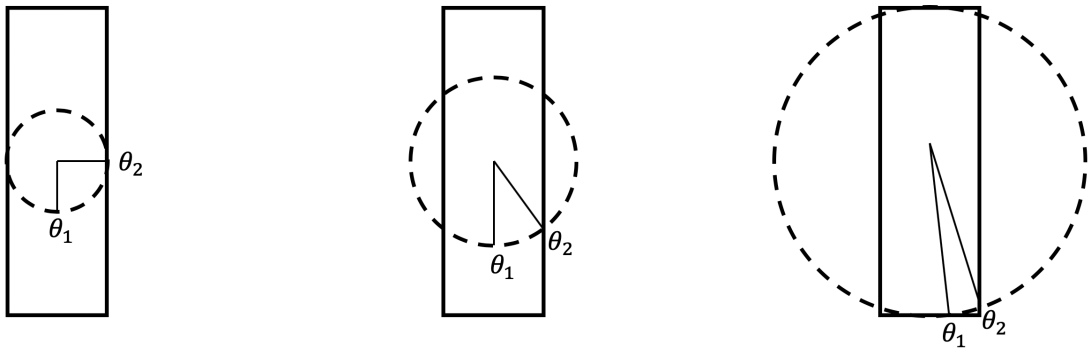

Figure 3.9 Progression of the spherical shell on a long hexagonal column.

Using the mirror symmetry of $\varepsilon(r,\theta) = \varepsilon(r,\pi-\theta)$, we can simplify Eqs.3.65 and 3.66:

$$U^{11}_{mnm'n'} = U^{22}_{mnm'n'}$$

$$= A_{mnm'n'} c_{nn'} \int_{\theta_1}^{\theta_2} d\theta sin\theta \, F_{mm'}(r,\theta) \, K^{ii}_{mnm'n'}(\theta), \qquad (3.80)$$

$$c_{nn'} = 1 + (-1)^{n+n'} \,,$$

$$U^{33}_{mnm'n'} = \tilde{A}_{mnm'n'} c_{nn'} \int_{\theta_1}^{\theta_2} d\theta sin\theta \, \tilde{F}_{mm'}(r,\theta) \, d^{n}_{0m}(\theta) d^{n'}_{0m'}(\theta), \qquad (3.81)$$

$$U^{12}_{mnm'n'} = -U^{21}_{mnm'n'}$$

$$= A_{mnm'n'}\tilde{c}_{nn'}\int_{\theta_1}^{\theta_2} d\theta sin\theta\, F_{mm'}(r,\theta)\, K^{ij}_{mnm'n'}(\theta), \qquad (3.82)$$

$$\tilde{c}_{nn'} = 1 + (-1)^{n+n'+1}.$$

$F_{mm'}(r,\theta)$ and $\tilde{F}_{mm'}(r,\theta)$ in this case are piecewise smooth functions in θ. Fig.3.10 shows $F_{mm'}(\theta)$ of some index mm' at a certain r_p. The discontinuity (in the first derivative) exists when the spherical shell intersects with the hexagonal surface. As a result, the U-matrix integrand $F_{mm'}(r,\theta)\, K^{ii}_{mnm'n'}(\theta)$ is no longer smooth in the interval $[\theta_1, \theta_2]$. The location of the discontinuity θ_{jump} is given in Eq.(16) of [22], where $r_p sin\theta_{jump} = \frac{\sqrt{3}a}{2}$.

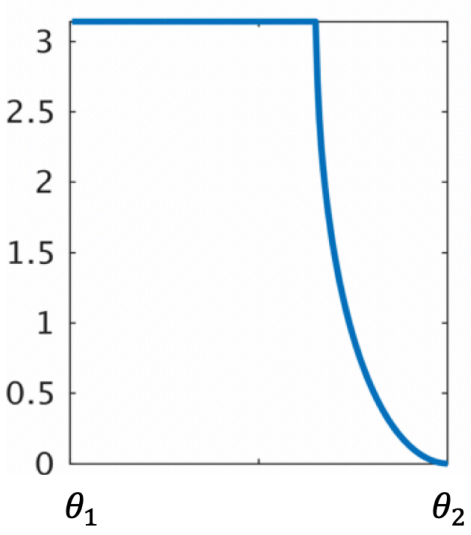

Figure 3.10 An example $F_{mm'}(r,\theta)$ as a function of θ.

In the II-TM method for spheroid and hexagonal column, the surface integration in the zenith direction (Eqs.3.77~3.82) are computed using Gauss-Legendre (GL) quadrature,

$$\int_0^{\pi} (d\theta sin\theta)\,(F_{mm'}(r,\theta)K^{ij}_{mnm'n'}(\theta)) \approx \sum_j^{N_q} w_j\,(F_{mm'}(r,\theta_j)K^{ij}_{mnm'n'}(\theta_j)), \tag{3.83}$$

In addition to the T-matrix truncation order N and the radial discretization Δr, the number of quadrature nodes N_q is an important parameter controlling the accuracy of the II-TM method. For a standard Gaussian Legendre quadrature like Eq.(3.83), the optimal numbers of nodes for quadrature of order N_q are given by the roots of the Legendre polynomials $P_{N_q}(x) = P_{N_q}(cos\theta)$. The GL quadrature is optimal if the integrand $(F_{mm'}(r,\theta)K^{ij}_{mnm'n'}(\theta))$ can be well approximated by polynomials of order $2N_q - 1$ or less. Generally, this means that the various orders of derivative of the integrand must be smooth. Discontinuities or singularities in the integrand or its derivatives will reduce the smoothness of the integrand. Higher order polynomials are required to approximate the fine scale oscillations of the integrand, and N_q in that case have very large values.

We use Gaussian quadrature on the following two integrals to illustrate our point that the convergence rate of the Gaussian quadrature depends on the behaviour of the integrand.

$$\int_0^1 f_1(x)dx \sim \sum_{n=1}^{N_q} w_n f_1(x_n), \qquad f_1(x) = \begin{cases} 1, & 0 \le x \le 0.5 \\ 2(1-x), & 0.5 < x \le 1 \end{cases} \tag{3.84}$$

$$\int_0^1 f_2(x)dx \sim \sum_{n=1}^{N_q} w_n f_2(x_n), \qquad f_2(x) = \begin{cases} 1, & 0 \le x \le 0.5 \\ 0.5[1 + cos2\pi(x-0.5)], & 0.5 < x \le 1 \end{cases} \tag{3.85}$$

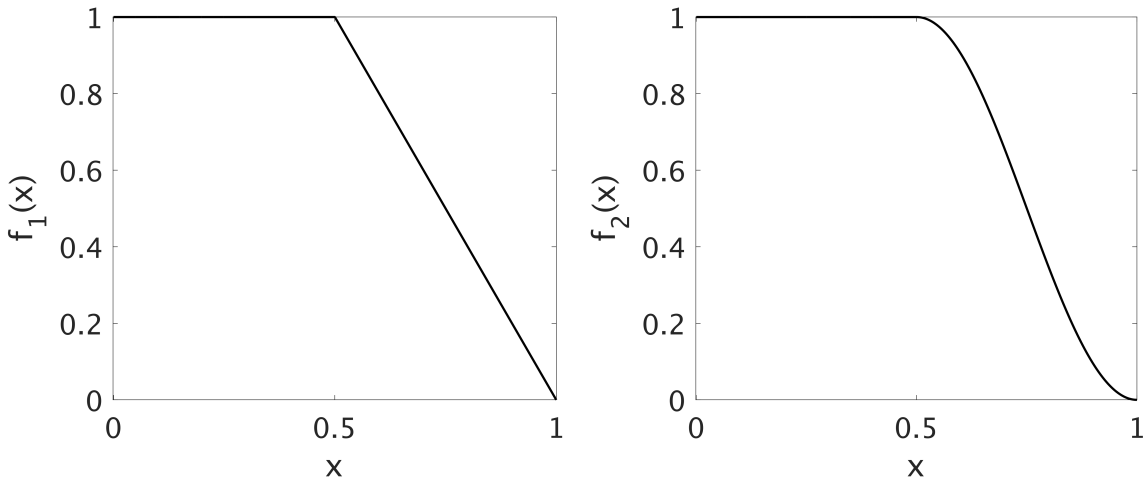

Figure 3.11 $f_1(x)$ and $f_2(x)$

The two integrals of $f_1(x)$ and $f_2(x)$ each have an analytical value of 0.75 so we can easily demonstrate the convergence rate of Gaussian quadrature on the two integrands. $f_2(x)$ is smooth inside the [0,1] interval while $f_1(x)$ possesses a discontinuity in its 1st derivative at x=0.5. The behaviour of $f_1(x)$ is very similar to that of $F_{mm'}(\theta)$ in Fig.3.10.

They both possess a discontinuity in the first derivative inside their integration range. Table 3.1 shows magnitude of the relative error with respect to an increasing number of nodes N_q for the two integrands. Apparently $f_2(x)$ has a superior rate of convergence.

	$f_1(x) = \begin{cases} 1, 0 \le x \le 0.5 \\ 2(1-x), 0.5 < x \le 1 \end{cases}$	$f_2(x) = \begin{cases} 1, 0 \le x \le 0.5 \\ 0.5[1 + cos2\pi(x-0.5)], 0.5 < x \le 1 \end{cases}$
	$\int_0^1 f_1(x)dx \sim \sum_{n=1}^{N_q} w_n f_1(x_n)$	$\int_0^1 f_2(x)dx \sim \sum_{n=1}^{N_q} w_n f_2(x_n)$
N_q	order of magnitude of RE	order of magnitude of RE
10	10^{-3}	10^{-9}
100	10^{-5}	10^{-9}
1000	10^{-7}	10^{-9}
10000	10^{-9}	10^{-9}

Table 3.1 Convergence rate of Gaussian quadrature for 2 different integrands in Fig.3.10. "RE" indicates the relative error which is given by the ratio of the difference between the quadrature and integral over the integral, or $RE = \frac{estimate-exact}{exact}$.

In the II-TM method, the spheroid has the simplest integrand among all other shapes (excluding sphere):

$$\int_0^{\theta_2} d\theta sin\theta \; d_{0m}^{n}(\theta) d_{0m'}^{n'}(\theta), \tag{3.86}$$

where the integrand is the product of Wigner-d functions $d_{0m}^{n}(\theta) d_{0m'}^{n'}(\theta)$. We expect rapid convergence of the quadrature with respect to N_q, since the integrand can be well approximated by polynomials,

$$\int_0^{\theta_2} d\theta sin\theta \; d_{0m}^{n}(\theta) d_{0m'}^{n'}(\theta) \approx \sum_{j}^{N_q} w_j \left(d_{0m}^{n}(\theta_j) d_{0m'}^{n'}(\theta_j) \right). \tag{3.87}$$

Fig.3.12 shows the convergence rate of the code outputs ($Q_{ext}, g, P_{11}(180^o)$) with respect to N_q. Q_{ext} is the extinction efficiency, and $P_{11}(180^o)$ is the phase function in the exact backscattering direction and g is the asymmetry factor. $N_q = 1000$ is chosen as the reference value and outputs of $N_q = 200{,}400{,}600 \; and \; 800$ are compared against it to show the convergence rate. Clearly, we can't do an $N_q = \infty$ calculation and $N_q = 1000$ is considered large enough. T-matrix truncation order N and radial discretization Δr are fixed. The T-matrix truncation order N is selected according to the formula,

$$N = x + 4.05x^{1/3} + 5, \tag{3.88}$$

This differs slightly from the Mie truncation order criterion for a sphere [23],

$$N_{MIE} = x + 4.05x^{1/3} + 2, \tag{3.89}$$

where x is the size parameter (Eq.1.10). Theoretically speaking, the T-matrix of a non-spherical particle should include more terms but no explicit formula has been published. We include 3 more terms than for a sphere. Δr is determined according to the formula,

$$\frac{\Delta \mathrm{r}}{R - r_0} = 0.1, \tag{3.90}$$

where r_0 is the radius of the homogeneous sphere inscribed inside the non-spherical particle and is the starting radius for the radial recurrence. R is the radius of the circumscribing sphere. The value 0.1 is considered to be enough for particles without small scale features like surface roughness. In our cases where the particle shapes are regular spheroids and hexagonal columns, 0.1 should be large enough.

The spheroid shape is indicated in the left panel of each row and x indicates the particle size parameter defined by,

$$x \approx \frac{2\pi R}{\lambda}, \tag{3.91}$$

where R is the radius of the circumscribing sphere of the particle.

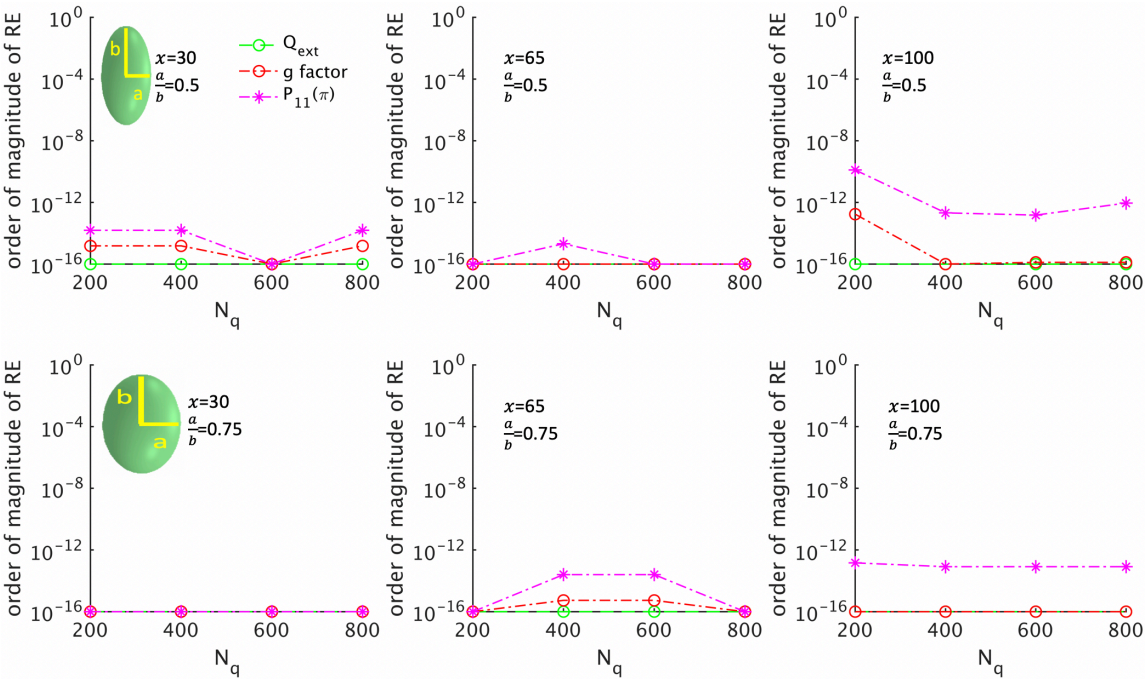

Figure 3.12 Convergence rate of the code outputs ($Q_{ext}, g, P_{11}(180^o)$) with respect to the number of quadrature nodes N_q. Each row has different aspect ratios, 3 panels in each row has different size parameters indicated in the top-left corner of each panel.

The convergence rates of different particle sizes show mixed behaviors. Generally, we can conclude that the convergence rate for a spheroid is relatively fast. In most cases, the outputs agree to more than 12 significant digits. As far as we know, the only obstacle for a spheroid is the intense oscillation shown by high-order Wigner-d functions for larger spheroids. Once N_q gets large enough (>200), the sampling rate is large enough and we have rapid convergence.

The integrals in the hexagonal column formulation take the following form,

$$\int_{\theta_1}^{\theta_2} d\theta sin\theta \, F_{mm'}(r,\theta) \, K^{ij}_{mnm'n'}(\theta) \, . \tag{3.92}$$

It was pointed out in Fig.3.10 that function $F_{mm'}(r,\theta)$ has a discontinuity in its first derivative when the spherical shell crosses the hexagonal column. We expect this to undermine the convergence of the quadrature if we do the quadrature in the interval $[\theta_1, \theta_2]$ which contains the discontinuity. Fig.3.13 shows the convergence rate of the code outputs ($Q_{ext}, g, P_{11}(180^o)$) with respect to N_q. $N_q = 1000$ is again used as the reference value. The hexagonal column shape is indicated in the left panel of each row and x is the size parameter.

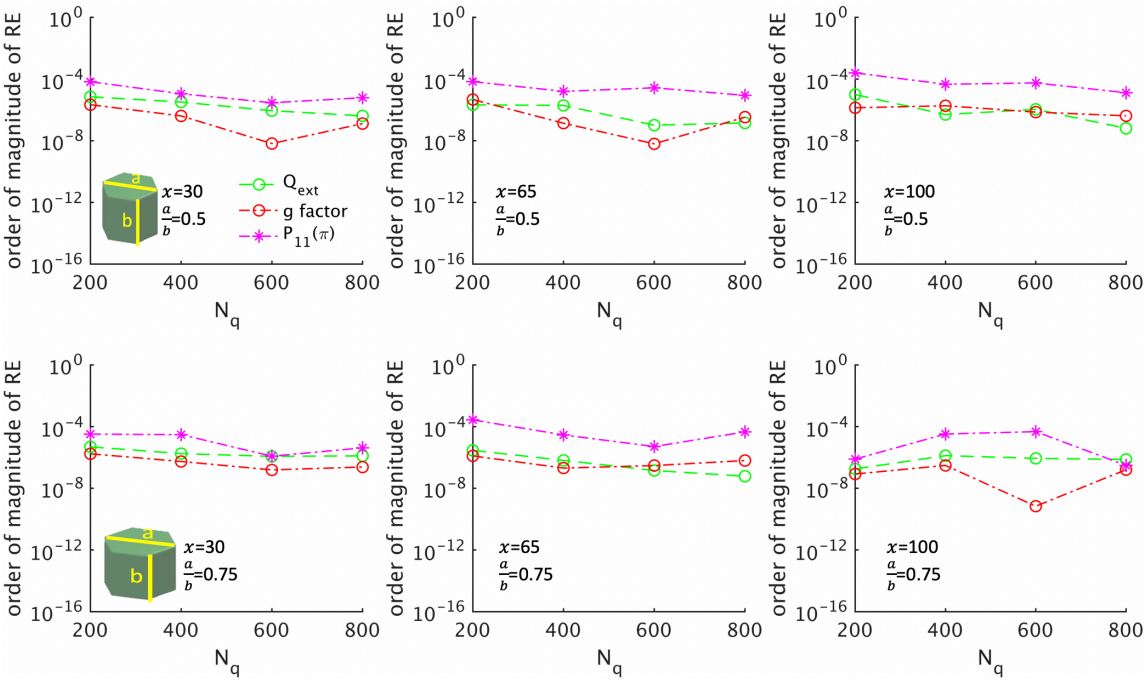

Figure 3.13 Convergence rate of the code outputs($Q_{ext}, g, P_{11}(180^o)$) with respect to number of quadrature nodes N_q as in Fig.3.11 but for hexagonal column.

Compared to spheroids (Fig.3.12), the convergence rate for hexagonal column is much slower. As is suspected, the discontinuity in $F_{mm'}(r,\theta)$ undermines the convergence rate of the quadrature (Fig.3.10). We know that there is only one discontinuity θ_{jump} in $[\theta_1, \theta_2]$ (Fig.3.10). A similar situation was encountered in EBCM for hexagonal columns [25]. A straightforward solution is to split the interval and perform quadrature on the two intervals where the integrand is smooth.

$$\int_{\theta_1}^{\theta_2} d\theta sin\theta\, F_{mm'}(r,\theta)\, K^{ij}_{mnm'n'}(\theta)$$

$$= \int_{\theta_1}^{\theta_{jump}} d\theta sin\theta\, F_{mm'}(r,\theta)\, K^{ij}_{mnm'n'}(\theta) \tag{3.93}$$

$$+ \int_{\theta_{jump}}^{\theta_2} d\theta sin\theta\, F_{mm'}(r,\theta)\, K^{ij}_{mnm'n'}(\theta).$$

After this modification, the results are shown in Fig.3.14. Compared to Fig.3.13, the convergence rate is accelerated. At this rate, we can expect to reach convergence to 16 digits at about $N_q = 1000$, which is an acceptable value for practical use.

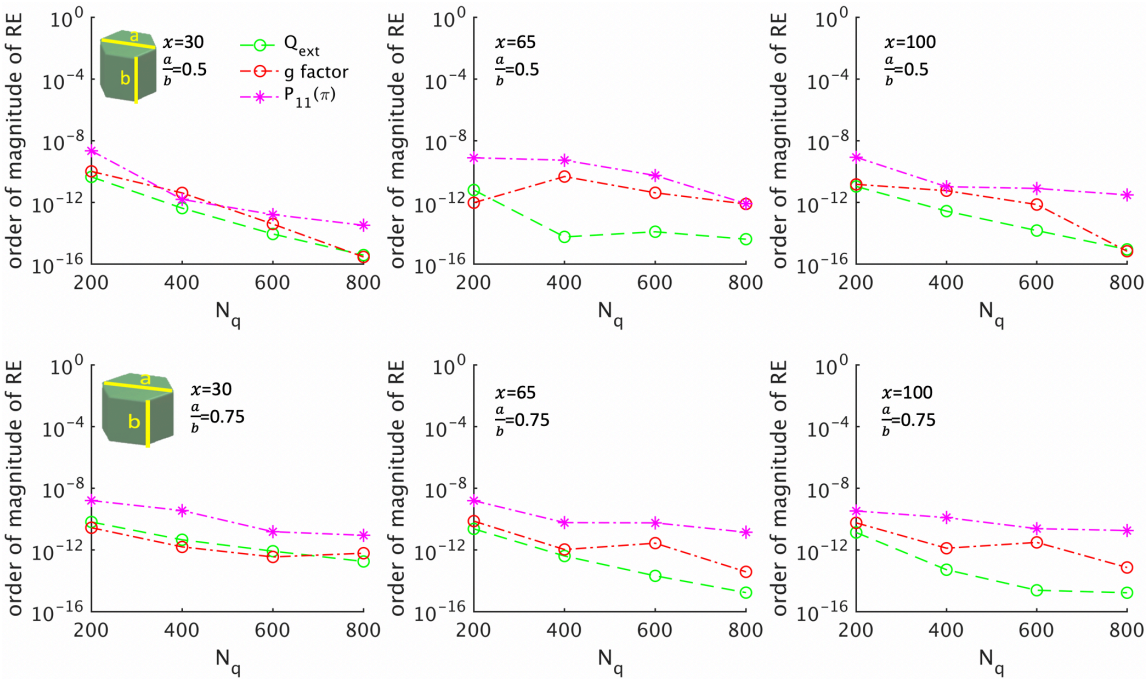

Figure 3.14 Convergence rate of the code outputs($Q_{ext}, g, P_{11}(180^o)$) with respect to number of quadrature nodes N_q as in Fig.3.12. Unlike Fig.3.12, the integration range is split into 2 smooth intervals, so the convergence rate is accelerated (see text).

From Figs.3.12 and 3.14, we can conclude that with respect to the number of quadrature points N_q, to reach convergence for common particle sizes and aspect ratios, N_q~1000 is enough for hexagonal columns and N_q~600 is enough for spheroids.

3.3. Accelerating the node generating scheme for Gaussian quadrature in II-TM

We have pointed out that the optimal nodes for Gaussian-Legendre quadrature of order L are the roots of Legendre Polynomials $P_L(x)$. There are no closed formulas for location of the roots, so they have to be generated numerically along with the corresponding weights. Different algorithms exist for generating the nodes and weights of Gauss-Legendre quadrature [26][27][28].

The current algorithm in the II-TM code uses the Newton-Raphson method to find the roots of $P_L(x)$[22]. Denote the L node-weight pairs by $\{x_{L,k}, w_{L,k}\}, k \in [0, L]$, and they satisfy $P_L\left(x_{L,k}\right) = 0$. The weights are given by $w_{L,k} = \frac{2(1-{x_{L,k}}^2)}{[(n+1)P_{L+1}(x_{L,k})]^2}$. For any large L, some initial value for $x_{L,k}$ is given and Newton-Raphson iterations are called to obtain a true value for $x_{L,k}$ up to a desired precision. The trick to the design of a fast algorithm is a proper choice of asymptotic expansions of the high-order Legendre polynomials.

The state-of-the-art algorithm for generating the Gaussian-Legendre quadrature nodes and weights is the Bogaert's algorithm [13][28]. In their algorithm, Newton-Raphson iteration is avoided by providing expansions directly for $x_{L,k}\ and\ w_{L,k}$. In the following discussions, the previous algorithm is referred to as "Newton" and the new algorithm is referred to as "Bogaert". The Bogaert algorithm is considered to be the fastest node and weight generating algorithm to date [29]. We expect the II-TM with the new algorithm (Bogaert) to produce the same outputs in less CPU time.

Table.3.2 shows the CPU time required to compute the same code section with the two methods. The code section is a simple quadrature of the integral $f_1(x) = \begin{cases} 1, 0 \le x \le 0.5 \\ 2(1-x), 0.5 < x \le 1 \end{cases}$ that appeared in Table.3.1. Obviously the Bogaert algorithm is much faster.

Nq	$\int_0^1 f_1(x)dx \sim \sum_{n=1}^{N_q} w_n f_1(x_n)$		$\frac{cpu\ time(Newton)}{cpu\ time(Bogaert)}$
	CPU time(sec) Newton	CPU time(sec) Bogaert	
10	<0.001	<0.001	--
100	<0.001	<0.001	--
1000	0.026	<0.001	--
10000	1.643	0.001	1643

Table 3.2 CPU time required to run the same code section (integrate $\boldsymbol{f_1(x) = \begin{cases} 1, 0 \le x \le 0.5 \\ 2(1-x), 0.5 < x \le 1 \end{cases}}$) with Newton and Bogaert algorithms.

Next, we put the Bogaert method into the II-TM code. Table.3.3 shows the acceleration for hexagonal columns and spheroids. II-TM is implemented with the Massage Passing Interface (MPI) parallelization and 100 CPUs were used for the experiments. Significant acceleration is achieved for hexagonal columns of all sizes and aspect ratios. Slight acceleration is achieved for spheroids.

shape	Size parameter	Aspect ratio	$\frac{CPU\ time(Newton)}{CPU\ time(Bogaert)}$	$\frac{wall\ clock\ time(Newton)}{wall\ clock\ time(Bogaert)}$
Hexagonal columns	$x = 30$	0.5	7.9	283.7
		0.75	9.5	432
	$x = 65$	0.5	2.2	34.1
		0.75	2.3	34.6
	$x = 100$	0.5	1.7	8.6
		0.75	1.6	9.1
spheroids	$x = 30$	0.5	1.1	0.9
		0.75	1.03	1.1
	$x = 65$	0.5	1.03	1.0
		0.75	1.2	1.1
	$x = 100$	0.5	1.1	0.8
		0.75	1.03	1.0

Table 3.3 Acceleration for hexagonal columns and spheroids of various sizes and aspect ratios.

We studied the performance of the angular quadrature in the II-TM method for a spheroid and a hexagonal column. The precision of the angular quadrature is of

fundamental importance to the entire II-TM procedure, and we want to obtain convergence to 16 significant digits by choosing an appropriate number of quadrature nodes N_q. A new node and weight generating algorithm (Bogaert algorithm) is implemented in the II-TM method, and considerable acceleration in computation time is achieved for hexagonal columns and spheroids. In the case of a hexagonal column, the previous formulation [8] is modified to avoid a discontinuity in the integration domain, and the convergence rate is massively accelerated. Based on convergence test results from spheroids and hexagonal columns with various sizes, we conclude that $N_q \sim 600$ for a spheroid and $N_q \sim 1000$ for a hexagonal column is sufficiently large.

4. MARINE HYDROSOL SINGLE SCATTERING DATASET

The previous chapters were devoted to single particle scattering problems where the solution is provided by the Maxwell's equations in the single scattering computational setup. This chapter focuses on the application of single scattering in oceanic forward and inverse radiative transfer problems, specifically, the comparison of the single scattering properties of spherical and irregular shapes.

The scattering and absorption characteristics of sea water are described by its inherent optical properties (IOPs). IOPs are properties of the medium and do not change with the ambient light field. One of the most important IOPs of a volume of water is the volume scattering function (VSF). The VSF describes the angular distribution ($0^o \sim 180^o$) of the scattered energy by a small volume of water. To measure the forward and backward scattering characteristics, the corresponding forward and backward coefficients are obtained by integrating the VSF in the forward and backward hemisphere respectively. IOPs can be measured in a laboratory on a water sample, or in situ on the open oceans. IOPs can also certainly be constructed with numerical models assuming certain particle shapes and composition. Comparison between measured and simulated IOPs can help to probe the composition of the sea water using remote sensing.

For observation and mapping of marine particulate matters on a global scale, aircraft and satellite remote sensing is the best approach. Given satellite or aircraft measurements overt a large area of ocean water, we attempt to obtain the IOPs and infer the constituents in those waters. Remote sensing is the inverse problem of radiative

transfer theory: Given measured radiometric signals of water-leaving or underwater light fields, determine the IOPs of the water.

To interpret either signals measured from lab water samples or a large ocean area, certain numerical models of the light field involved need to be constructed, but models on all scales require single scattering properties of small particles as inputs. Next, we will introduce the constituents of water and a dataset constructed as an expansion of the commonly assumed spherical particle shape.

4.1. Water constituents

According to their optical properties and measurement methods, water constituents can be divided into these groups:

1. Sea water (water with inorganic dissolved matter)
2. Bubbles
3. Colored dissolved organic matter
4. Phytoplankton
5. Non-phytoplankton organic detritus
6. Inorganic particles

The identification of these groups is defined both according to their strict chemical composition and measurement methods. For example, the distinction between dissolved

matter and particulate matter is defined by the measurement filter type/pore size used in measurements.

Among these particulates, the phytoplankton group is the most important and interesting. We have to account for them in forward and inverse radiative transfer studies due to their dominant number in marine particulate matters. Their relatively large size and wide size range make them a dominant factor in scattering in the visible wavelengths. Also, they are the base of the ocean food chain and a vital component in the global carbon cycle [30]. This makes it extremely important to monitor their concentration at the global scale via retrievals using satellite and airborne measurement data. Most phytoplankton are single-celled. One important composition in their cell is chlorophyll. Chlorophyll allows phytoplankton to do photosynthesis.

In terms of their taxonomy, phytoplankton is a very diverse group. The group consists of more than 10000 taxa and species[31]. The most numerous groups of phytoplankton include algae, diatoms, dinoflagellates and coccolithophores. Phytoplankton have different sizes, shapes and compositions. Their size ranges from around 0.1 μm to 1000 μm. Commonly encountered shapes include cylinders, ellipsoids and many more. Table 4.1 lists typical phytoplankton of various sizes.

Plankton	Size(**diameter**)	Phytoplankton types
mesoplankton	100~1000 μm	Metazoans Copepods Tunicates Pteropods Cladocera
microplankton	10~100 μm	large eukaryotic protists most phytoplankton ciliates
Nanoplankton	1~10 μm	Small eukaryotic protists Small diatoms Small flagellates Pyrrophyta (algae with hard shells) Chrysophyta (golden algae) Chlorophyta (green algae) Xanthophyta (yellow-green algae)
picoplankton	0.1~1 μm	Small eukaryotic protists Bacteria Chrysophyta
femtoplankton	<0.1 μm	viruses

Table 4.1 Categorization of different phytoplankton based on their sizes along with examples of those phytoplankton.

Table 1 in [32] provides a list of the real part of index of refraction of marine particles with the methods to obtain them. Relative to sea water, most organic and inorganic particles' refractive indices vary between 1.05 and 1.20. In terms of the approach of numerical modelling, the shape, internal structure and composition of marine particles are extremely complicated and varied. We cannot cover all the possibilities in the finite parameter space in our numerical models. Also, due to the

physical assumption of random orientation of single particle and size averaging on polydisperse particles with varying sizes in the scattering volume, it has been widely accepted that a spherical shape can adequately represent small particle bulk optical properties [33][34].

Compared to other single scattering solvers for non-spherical and inhomogeneous particles (FDTD, DDA, etc.), the Lorenz-Mie theory is extremely easy to use and very efficient. In a very short time, one can obtain numerical model outputs for a large number of model inputs (radii, refractive indices). However, a sphere is not likely to be a good representation of the average shape of marine particles. First of all, most marine particles are not spherical. Secondly, a sphere has the lowest surface area-to-volume ratio, in spite of the fact that most single-cell organisms try to have a high surface area-to-volume ratio for maximum efficiency in photosynthesis and capturing prey. Moreover, comparison of in-situ measured data and modelling results suggest that a homogeneous spherical shape often underestimate the bulk backscattering. This phenomenon is widely known and is given the name “backscattering enigma” [35]

An easy alternative is to use a coated sphere as the model particle shape, and some progress in interpreting the measured backscattering signal has been made [36][37][38]. The coated sphere model provides additional structural complexity and can still be easily modelled. Other studies look into the possibility of using an overall non-spherical shape to model marine particles [39][40][41] . All of these studies have found out that there is strong dependence of optical properties on the assumed particle shape.

4.2. The hexahedral ensemble dataset

To provide an alternative to using a sphere and a coated sphere, we computed and compiled a dataset for an ensemble of distorted hexahedra. For each incident wavelength, each refractive index n and size, there is a 20-random-hexahedra ensemble. Each individual hexahedron in the ensemble is assigned the same volume and the same refractive index. The only difference among them is that each individual shape is randomly distorted. The degree of distortion is controlled by a parameter which determines the distribution of the tilting angle of the 6 facets of a hexahedron. Each individual hexahedron is input into our single scattering simulation codes. The single scattering properties of the 20 hexahedra is averaged and is considered to represent a single marine hydrosol with that size (volume) and refractive index.

This random hexahedral ensemble approach was proposed and used in interpreting satellite data for dust particles [42]. Borrowing from their idea of representing natural irregular dust particles with a random hexahedral ensemble, we use it here for representing natural marine particles.

The incident wavelength is 658nm. The particle size is defined with the equivalent volume sphere radius. The equivalent-volume-sphere radius ranges from 0.001 μm ~300 μm in this dataset. This size range covers most hydrosols ranging from viruses to large phytoplankton, and organic and inorganic detritus particulates. The real part of refractive indices ranges from 1.02~1.2(relative to pure water), and the imaginary part ranges from 0.0005~0.01. The invariant-imbedding T-matrix (II-TM) introduced

earlier is used to compute those with size 0.001 μm ~2 μm. The physical geometric optics method (PGOM) is used to compute those with size 2.1~300 μm. The PGOM will be introduced later. Fig.4.1 shows each individual shape used in the hexahedra ensemble. Each irregular hexahedron is obtained by distorting a regular hexahedron. Specifically, the slope of each particle facet in the ensemble is controlled by the normal distribution,

$$P\ \ (t_x, t_y) = \frac{1}{\pi\sigma^2}\exp\left(-\frac{{t_x}^2 + {t_y}^2}{\sigma^2}\right) \tag{4.1}$$

where t_x, t_y are the slopes along two orthogonal directions with respect to the regular facet. The standard deviation of the normal distribution is σ^2 ,and controls statistically how rough these distorted hexahedra are. Larger σ^2 values correspond to a more irregular hexahedron.

In Fig.4.1, the four rows each has $\sigma^2 = 0.3,0.4,0.5,1.0$ respectively.

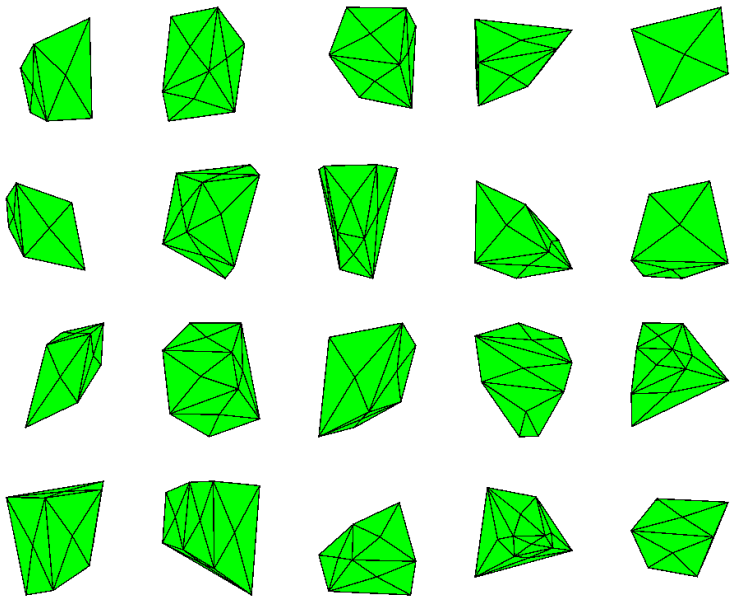

Figure 4.1 The 20-shapes ensemble. 4 rows from top to bottom were constructed with σ^2=0.3,0.4,0.5,1.0, respectively.

The single scattering properties are averaged in the following manner [43],

$$P_{ij}(n, size, \theta) = \frac{\sum_{k=1}^{20} C_{sca,k}(n, size) P_{ij,k}(n, size, \theta)}{\sum_{k=1}^{20} C_{sca,k}(n, size)} \tag{4.2}$$

$$Q_{ext,sca}(n, size) = \frac{\sum_{k=1}^{20} C_{ext,sca,k}(n, size)}{\sum_{k=1}^{20} C_{geo,k}(n, size)} \tag{4.3}$$

where n is the refractive index, *size* is particle size defined according to its volume, $C_{sca,k}$ is the scattering cross section and $C_{geo,k}$ is the projected area. The asymmetry factor is computed with the averaged phase function. Fig.4.2 shows the phase matrix elements of

the individual hexahedra and their average when the particle equivalent-volume sphere radius is 2.0 μm. Results are computed with II-TM.

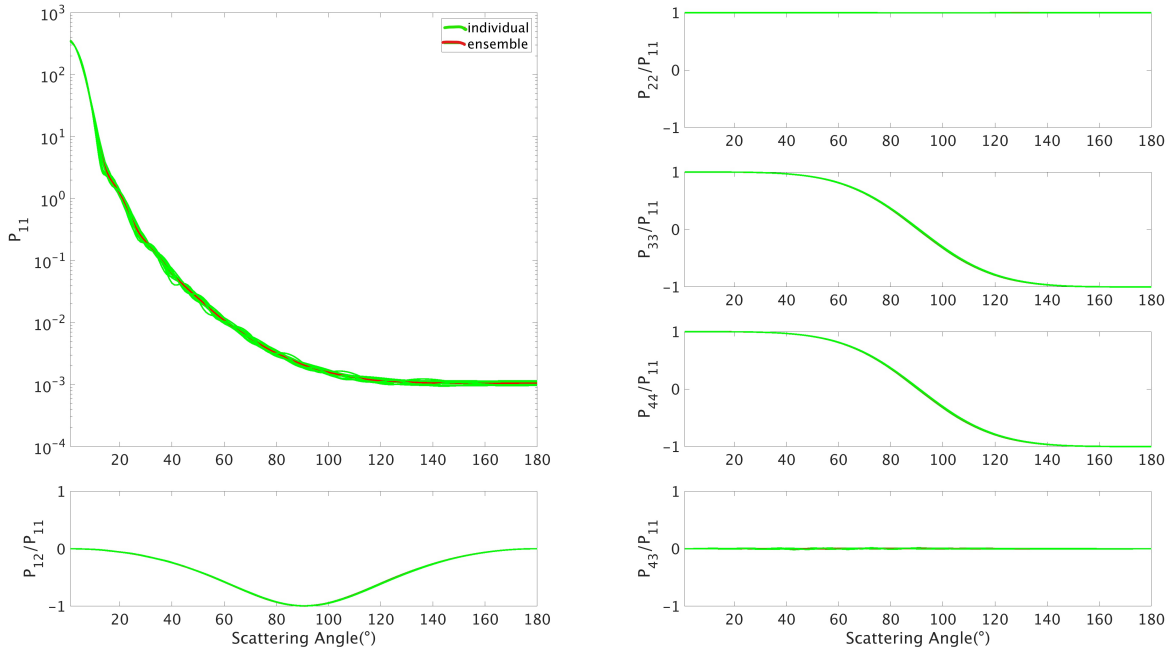

Figure 4.2 Individual phase matrix elements(green) against their ensemble averaged values. The average(red) is in between the individual lines.

The structure of the dataset is illustrated in Fig.4.3. X-axis is the equivalent-volume sphere radius, y-axis is the refractive index.

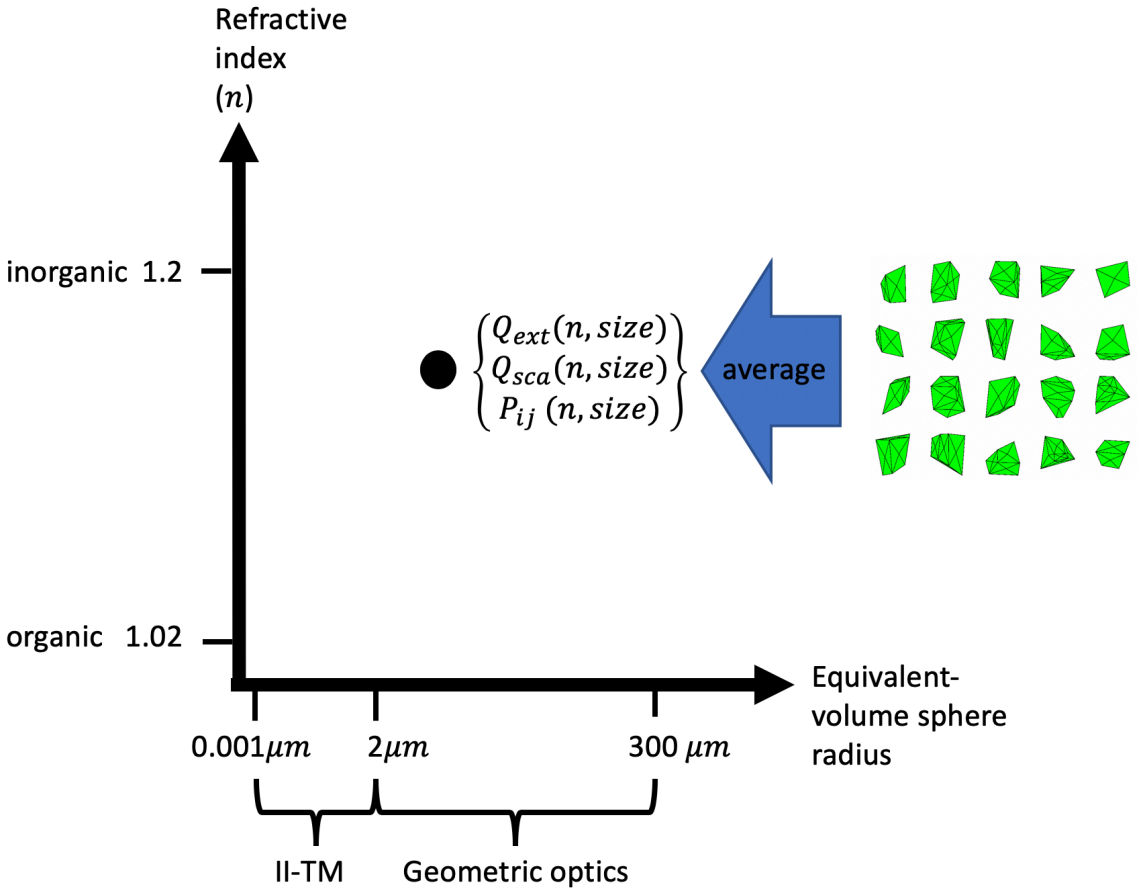

Figure 4.3 Parameter space of the dataset.

It is vital to check that the transition at size 2.0μm between II-TM and PGOM is smooth. Fig.4.4 shows the comparison between II-TM and PGOM at equivalent-volume-radius 2.0 μm. The particle refractive index is 1.02+0.0005i. The agreement between II-TM and PGOM is very good. Fig.4.6 shows that the physical quantities, namely, the extinction, scattering efficiency ($Q_{ext,sca}$), single scattering albedo (SSA), asymmetry factor(g). Note that all curves have a smooth transition at 2.0 μm, except for a little jump in the asymmetry factor. Overall, the combination of II-TM and PGOM can safely cover the size range 0.001 μm ~300 μm.

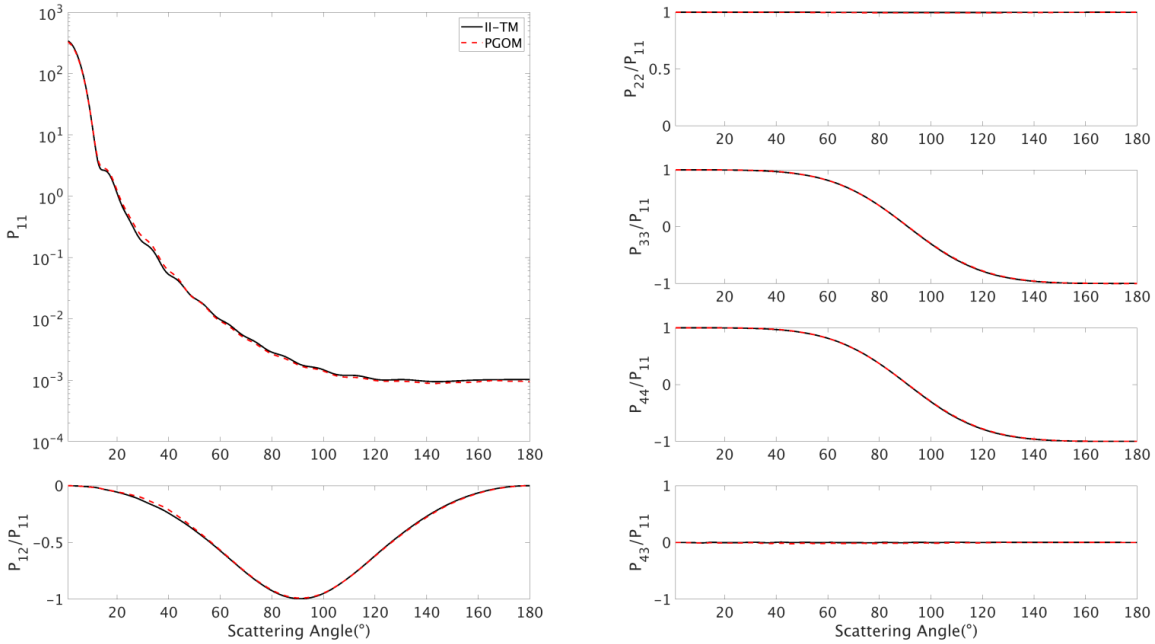

Figure 4.4 Phase matrix elements of ocean particles at incident wavelength 658 nm, particle refractive index 1.02+i0.0005, and particle equivalent-volume-sphere radius 2.0 μm.

4.3. The physical geometric optics method (PGOM)

The PGOM ray tracing method used to compute the optical properties for large particles is briefly introduced in this section. For details go to [14]. The ray tracing method and its numerical implementation has a long history [44]. The conventional geometric optics method (CGOM) uses an enormous number of rays to trace the electromagnetic near field [45]. After the near field is obtained with ray tracing, the analytical near-to-far-field

mapping is replaced with certain empirical formulas [45]. Thus, the interference between different rays on their way from the particle to infinity is ignored.

The PGOM method uses beam tracing to compute the near field. For faceted particles, all rays incident on a facet can be treated all together as a single beam. This has the advantage that the large number of rays we need to account for is reduced to one single beam. On the other hand, the near-to-far-field mapping is carried out with Eq. (2.1), which is repeated here,

$$\overrightarrow{E_s}(\vec{r})\Big|_{kr\to\infty} = \frac{k^2 e^{ikr}}{4\pi r}\iiint_V d^3\overrightarrow{r'}\left[m^2\left(\overrightarrow{r'}\right)-1\right]e^{-ik\hat{r}\cdot\overrightarrow{r'}}\left\{\vec{E}\left(\overrightarrow{r'}\right) - \hat{r}\left[\hat{r}\cdot\vec{E}\left(\overrightarrow{r'}\right)\right]\right\}, \tag{4.4}$$

Thus, the near-to-far-field mapping is conducted analytically, which greatly improves the accuracy of the method.

The direction and amplitude of the reflected and refracted waves at the particle interface is of course accounted for by the usual Snell's law and Fresnel formulas (Fig.4.5b). The challenge in the method is proper beam splitting once the beam impinges on multiple facets. Fig.4.5a illustrates the situation where during the beam tracing iterations, one beam could face multiple particle facets. When the beam column impinges on multiple facets,

the beam needs to be split correctly to ensure that each divided sub-beam is incident only on its own facet.

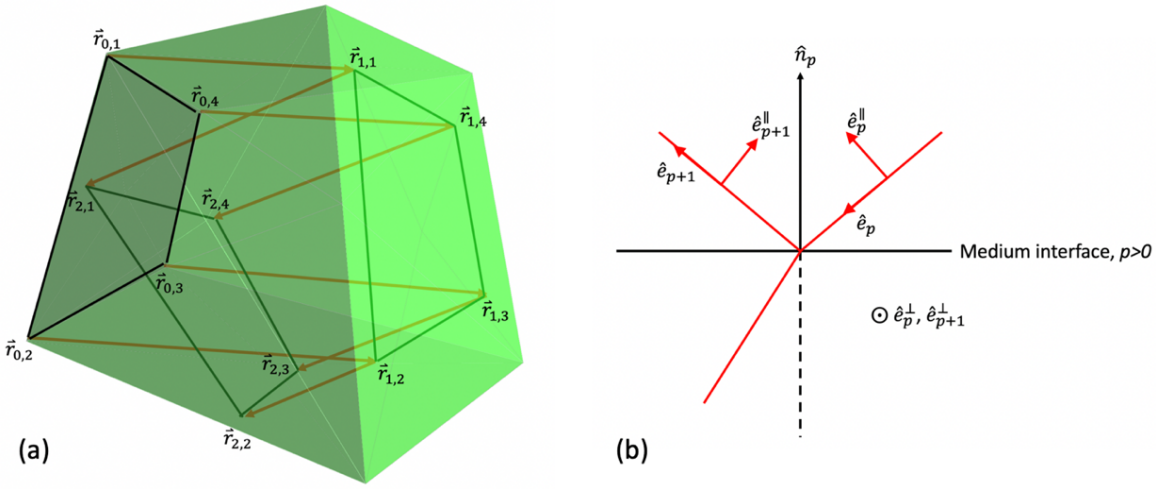

Figure 4.5 (a)Beam tracing in a faceted particle. (b)Schematic of reflection and refraction event at an interface of changing refractive index.

4.4. Comparison with spheres

Here we compare the simulated single and bulk scattering properties of homogeneous spheres and our homogeneous irregular hexahedral ensembles.

Fig.4.6 shows the single scattering properties: extinction, scattering efficiencies ($Q_{ext,sca}$), single scattering albedo (SSA), asymmetry factor(g). The high refractive index (1.18) corresponds to inorganic particles. The transition from II-TM (solid line) to PGOM (dashed line) is smooth.

In terms of Q_{ext} and Q_{sca}, a sphere and a hexahedral ensemble generally show the same trend, but a sphere shows much higher peaks. For larger particles(>10um), a sphere shows a higher SSA, meaning the scattering of a sphere is stronger than for hexahedra. The asymmetry factors of the 2 shapes basically share the same trend.

Observational data usually measure bulk properties. Since our dataset provides single scattering properties across the size spectrum, we can integrate with respect to a particle size distribution (PSD) to obtain our modelled bulk scattering properties. The Junge distribution in the form Ar^{-4} is selected, based on previous studies [43].

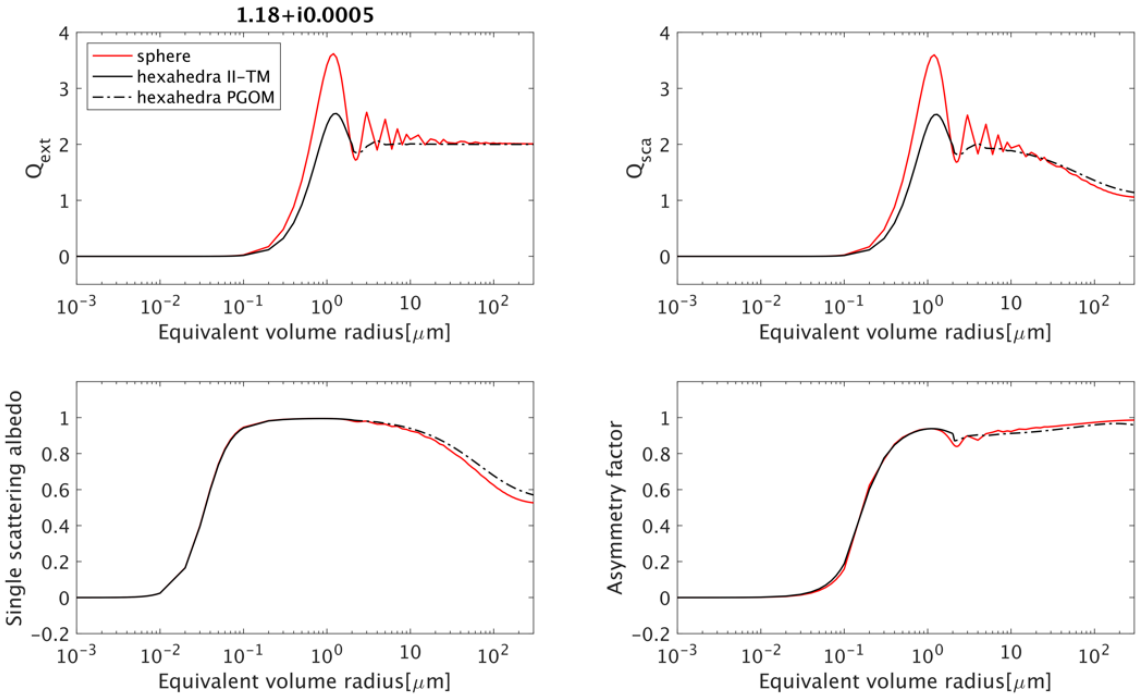

Figure 4.6 Qext, Qsca, SSA (single scattering albedo) and asymmetry factor as functions of particle size. Refractive index=1.18+i0.0005.

The size distribution is a Junge distribution with exponent -4,

$$\frac{dN}{dr} = \mathrm{A}r^{-4} \tag{4.5}$$

The bulk Mueller matrix is obtained by integrating over the particle size distribution,

$$M_{ij}(n,\theta) = \int_{r_{min}}^{r_{max}} dr \frac{dN}{dr} C_{sca}(n, size)\, P_{ij}(n, size, \theta), \qquad i,j = 1,4 \tag{4.6}$$

M_{11} is the volume scattering function (VSF). In most cases, the Mueller matrix elements are normalized to M_{11} for comparison with other data,

$$\bar{M}_{ij}(n,\theta) = \frac{M_{ij}(n, size, \theta)}{\int_0^{180} d\theta sin\theta M_{11}(n, size, \theta)} \tag{4.7}$$

The backscattering ratio indicates the relative backscattering intensity,

$$B_b/B(n) = \frac{\int_{90}^{180} d\theta sin\theta M_{11}(\theta)}{\int_0^{180} d\theta sin\theta M_{11}(\theta)} \tag{4.8}$$

Figs.4.7 and 4.8 show the normalized VSF $\bar{M}_{11}(n,\theta)$ values in four cases. Two indices of refraction are shown, n=1.06+i0.0005 and n=1.12+i0.0005, in order to

represent organic and inorganic particles respectively. The only difference between the data presented in Fig.4.7 and 4.8 is their integration size range. In both figures, $r_{max} = 70um$ while $r_{min} = 0.1um$ in Fig.4.7 and $r_{min} = 1um$ in Fig.4.8. It was pointed out that submicron particles are the major source of oceanic particulate backscattering [46][47] .Through our simple comparison of Figs.4.7 and 4.8, taking out the submicron (<1um) particles leads to a significant drop in backscattering. The decrease in backscattering ratio is both visible in the shape of $\overline{M}_{11}(n, \theta)$ and the backscattering ratio. In Fig.4.7, the hexahedral ensemble model produces backscattering ratio as high as ~0.2 while a sphere produces much lower backscattering. In Fig.4.8, without the submicron particles, the hexahedral ensemble model produces a slightly lower backscattering ratio than sphere. This comparison demonstrates the drastically different optical signals produced by spheres and hexahedral ensembles. Through Figs.4.6~8, we see that the sphere model and our hexahedral model have their similarities and differences. Their huge difference in the bulk scattering properties will lead to different retrieval results when both are implemented in actual retrieval studies using ocean optics measurement data.

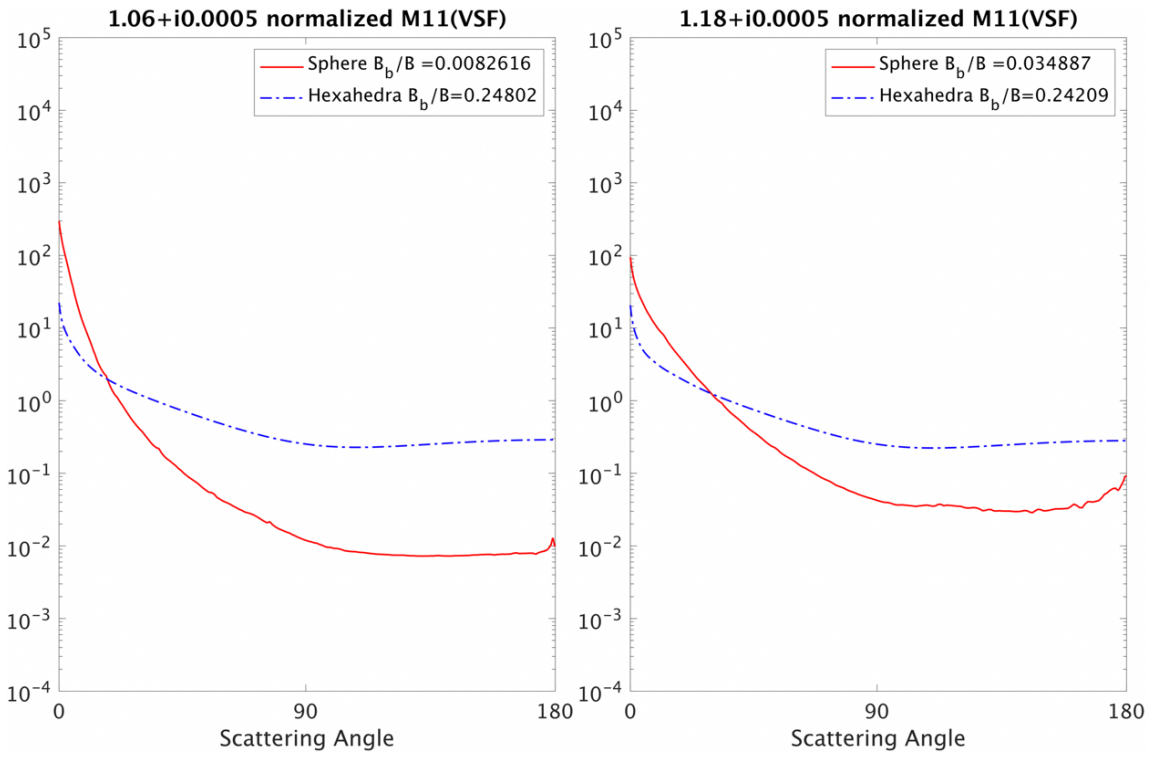

Figure 4.7 Normalized VSF of a sphere (red line) and hexahedra ensemble (blue dotted). Two refractive indices are indicated in the titles. The integration size range [0.1um,70um] is used in the computation of VSF. In this case, our hexahedral model produces much higher backscattering than the spherical model.

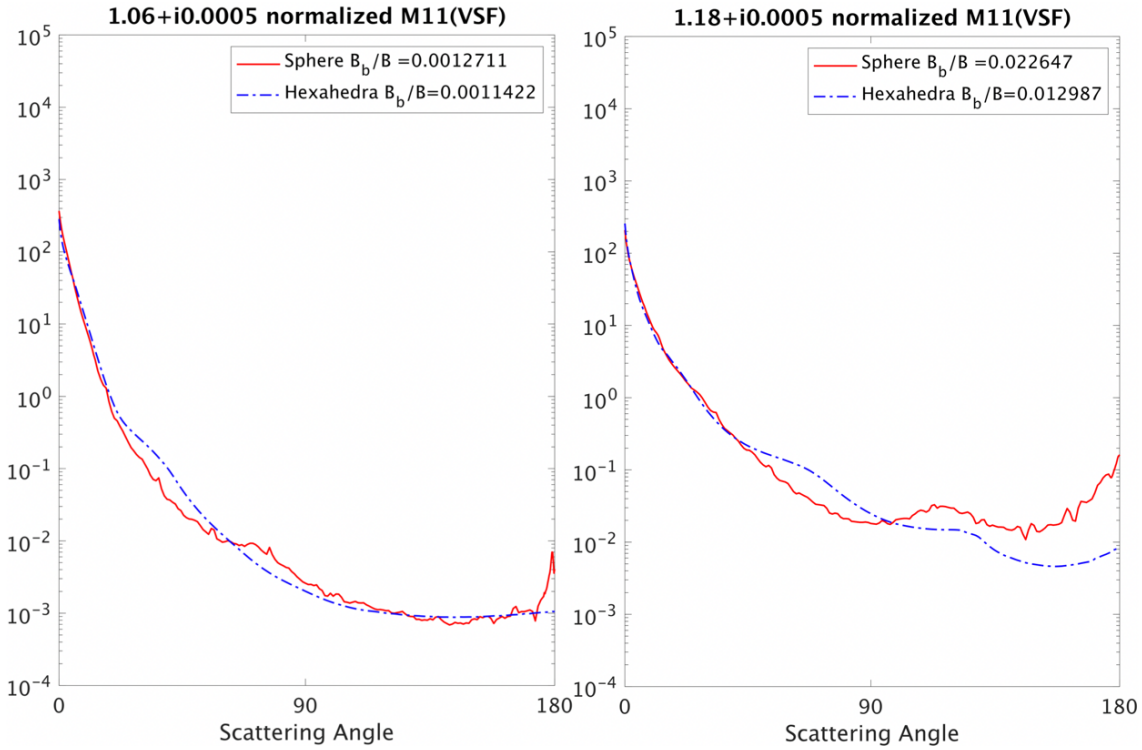

Figure 4.8 Normalized VSF of sphere (red line) and hexahedra ensemble (blue dotted). Two refractive indices are indicated in the titles. The integration size range [1um,70um] is used in the computation of VSF. In this case, our hexahedral model produces lower backscattering than the spherical model.

5. CONCLUSIONS

In this dissertation, investigation of the convergence behaviors of two numerical schemes for single scattering simulations (PSTD and II-TM) is presented. Improvements in the convergence are shown for the II-TM method. Both methods are designed for accurately solving the Maxwell's Equation to obtain the single scattering properties of non-spherical and inhomogeneous particles.

For the PSTD method, we study the electromagnetic near field in a 2-D computational domain to see how the near field decays to zero. The decay pattern determines how long (or how many time steps) we should integrate the discretized Maxwell's equation in time domain. A travelling surface wave packet is observed in the particle interior along its boundary. Three different cross-sectional shapes are considered: a circle, ellipse and hexagon. We observe three different mechanisms for the surface wave packets to escape the particle interior. For the II-TM method, we investigate the Gaussian quadrature employed to compute the surface integrations. We also modify the original quadrature scheme to avoid doing quadrature over discontinuities in the case of a hexagonal column. We also implement a new node and weight generating procedure into the II-TM method. These two improvements greatly improve the computational efficiency of the II-TM method for hexagonal columns and spheroids.

A dataset intended for marine hydrosols is computed with the II-TM and PGOM methods. A hexahedral ensemble is employed to represent the complex particle

geometry seen in natural oceanic particles. Size and refractive index values in the dataset cover most natural marine hydrosol parameters. A comparison between a sphere and our hexahedra ensemble shows major differences are found in the shape of the volume scattering functions (VSF). This difference in the bulk scattering properties of sphere and hexahedral ensemble will lead to different retrieval results when both are implemented in actual retrieval studies using ocean optics measurement data.

REFERENCES

[1] Feynman RP. Quantum electrodynamics. 2018. doi:10.1201/9780429493249.

[2] Jackson JD. Jackson - Classical Electrodynamics (3rd Ed.). Am J Phys 1962. doi:10.1119/1.19136.

[3] Mishchenko MI. Multiple scattering by particles embedded in an absorbing medium. 2. Radiative transfer equation. J Quant Spectrosc Radiat Transf 2008. doi:10.1016/j.jqsrt.2008.05.006.

[4] Bohren CF, Huffman DR. Absorption and Scattering of Light by Small Particles (Wiley science paperback series). 1998. doi:10.1017/S0263574798270858.

[5] Asano S, Sato M. Light scattering by randomly oriented spheroidal particles. Appl Opt 2008. doi:10.1364/ao.19.000962.

[6] Mishchenko MI, Travis LD. Capabilities and limitations of a current FORTRAN implementation of the T-matrix method for randomly oriented, rotationally symmetric scatterers. J Quant Spectrosc Radiat Transf 1998. doi:10.1016/S0022-4073(98)00008-9.

[7] Johnson BR. Invariant imbedding T matrix approach to electromagnetic scattering. Appl Opt 1988. doi:10.1364/AO.27.004861.

[8] Bi L, Yang P, Kattawar GW, Mishchenko MI. Efficient implementation of the invariant imbedding T-matrix method and the separation of variables method applied to large nonspherical inhomogeneous particles. J Quant Spectrosc Radiat Transf 2013. doi:10.1016/j.jqsrt.2012.11.014.

[9] Yee KS. Numerical Solution of Initial Boundary Value Problems Involving Maxwell's Equations in Isotropic Media. IEEE Trans Antennas Propag 1966. doi:10.1109/TAP.1966.1138693.

[10] Yang P, Liou KN. Finite-difference time domain method for light scattering by small ice crystals in three-dimensional space. J Opt Soc Am A 1996. doi:10.1364/JOSAA.13.002072.

[11] Yurkin MA, Hoekstra AG. The discrete dipole approximation: An overview and recent developments. J Quant Spectrosc Radiat Transf 2007. doi:10.1016/j.jqsrt.2007.01.034.

[12] Liu C, Lee Panetta R, Yang P. Application of the pseudo-spectral time domain method to compute particle single-scattering properties for size parameters up to 200. J Quant Spectrosc Radiat Transf 2012. doi:10.1016/j.jqsrt.2012.04.021.

[13] Bogaert I. Iteration-Free Computation of Gauss--Legendre Quadrature Nodes and Weights. SIAM J Sci Comput 2014. doi:10.1137/140954969.

[14] Sun B, Yang P, Kattawar GW, Zhang X. Physical-geometric optics method for large size faceted particles. Opt Express 2017. doi:10.1364/oe.25.024044.

[15] Taylor FW. Theory of Atmospheric Radiative Transfer: A Comprehensive Introduction, by Manfred Wendisch and Ping Yang. Contemp Phys 2012. doi:10.1080/00107514.2012.732967.

[16] Panetta RL, Zhai S, Yang P. Internal electromagnetic waves, energy trapping, and energy release in simple time-domain simulations of single particle scattering. J Quant Spectrosc Radiat Transf 2019. doi:10.1016/j.jqsrt.2019.01.015.

[17] Heifetz A, Kong SC, Sahakian A V., Taflove A, Backman V. Photonic nanojets. J Comput Theor Nanosci 2009. doi:10.1166/jctn.2009.1254.

[18] Nussenzveig HM. High-frequency scattering by a transparent sphere. I. Direct reflection and transmission. J Math Phys 1969. doi:10.1063/1.1664764.

[19] Nussenzveig HM. High-frequency scattering by a transparent sphere. II. Theory of the rainbow and the glory. J Math Phys 1969. doi:10.1063/1.1664747.

[20] Laven P. Time domain analysis of scattering by a water droplet. Appl Opt 2011. doi:10.1364/ao.50.000f29.

[21] Khaled EEM, Hill SC, Barber PW. Scattered and internal intensity of a sphere illuminated with a Gaussian beam. IEEE Trans Antennas Propag 1993. doi:10.1109/8.233134.

[22] Bi L, Yang P. Accurate simulation of the optical properties of atmospheric ice crystals with the invariant imbedding T-matrix method. J Quant Spectrosc Radiat Transf 2014. doi:10.1016/j.jqsrt.2014.01.013.

[23] Wiscombe WJ. Improved Mie scattering algorithms. Appl Opt 1980. doi:10.1364/AO.19.001505.

[24] Somerville WRC, Auguié B, Le Ru EC. Simplified expressions of the T-matrix integrals for electromagnetic scattering. Opt Lett 2011. doi:10.1364/OL.36.003482.

[25] Kahnert FM, Stamnes JJ, Stamnes K. Application of the extended boundary condition method to particles with sharp edges: a comparison of two surface integration approaches. Appl Opt 2001. doi:10.1364/AO.40.003101.

[26] Glaser A, Liu X, Rokhlin V. A Fast Algorithm for the Calculation of the Roots of Special Functions. SIAM J Sci Comput 2007. doi:10.1137/06067016x.

[27] Golub GH, Welsch JH. Calculation of Gauss Quadrature Rules. Math Comput 2006. doi:10.2307/2004418.

[28] Townsend A, Trogdon T, Olver S. Fast computation of Gauss quadrature nodes and weights on the whole real line. IMA J Numer Anal 2014. doi:10.1093/imanum/drv002.

[29] Townsend A. The race to compute high-order Gauss-Legendre quadature. SIAM J Sci Comput 2015.

[30] Falkowski PG, Raven JA. 1. An Introduction to Photosynthesis in Aquatic Systems. Aquat. Photosynth., 2014. doi:10.1515/9781400849727.1.

[31] Jeffrey SW. Introducction to marine phytoplankton and their pigment signatures. Phyitoplankt. Pigment. Oceanogr. Guid. to Mod. metohods, 1997.

[32] Aas E. Refractive index of phytoplankton derived from its metabolite composition. J Plankton Res 1996. doi:10.1093/plankt/18.12.2223.

[33] Holland AC, Gagne G. The Scattering of Polarized Light by Polydisperse Systems of Irregular Particles. Appl Opt 2008. doi:10.1364/ao.9.001113.

[34] Plass GN, Kattawar GW. Comment on: The Scattering of Polarized Light by Polydisperse Systems of Irregular Particles 1. Appl Opt 2008. doi:10.1364/ao.10.1172_1.

[35] Stramski D, Boss E, Bogucki D, Voss KJ. The role of seawater constituents in light backscattering in the ocean. Prog Oceanogr 2004.

doi:10.1016/j.pocean.2004.07.001.

[36] Poulin C, Zhang X, Yang P, Huot Y. Diel variations of the attenuation, backscattering and absorption coefficients of four phytoplankton species and comparison with spherical, coated spherical and hexahedral particle optical models. J Quant Spectrosc Radiat Transf 2018. doi:10.1016/j.jqsrt.2018.05.035.

[37] Bhowmik A, Pilon L. Can spherical eukaryotic microalgae cells be treated as optically homogeneous? J Opt Soc Am A 2016. doi:10.1364/josaa.33.001495.

[38] Zaneveld JR V., Kitchen JC. The variation in the inherent optical properties of phytoplankton near an absorption peak as determined by various models of cell structure. J Geophys Res 2004. doi:10.1029/95jc00451.

[39] Gordon HR. Backscattering of light from disklike particles: is fine-scale structure or gross morphology more important? Appl Opt 2006. doi:10.1364/ao.45.007166.

[40] MacCallum I, Cunningham A, McKee D. The measurement and modelling of light scattering by phytoplankton cells at narrow forward angles. J Opt A Pure Appl Opt 2004. doi:10.1088/1464-4258/6/7/007.

[41] Quirantes A, Bernard S. Light-scattering methods for modelling algal particles as a collection of coated and/or nonspherical scatterers. J Quant Spectrosc Radiat Transf 2006. doi:10.1016/j.jqsrt.2005.11.048.

[42] Bi L, Yang P, Kattawar GW, Kahn R. Modeling optical properties of mineral aerosol particles by using nonsymmetric hexahedra. Appl Opt 2010. doi:10.1364/ao.49.000334.

[43] Xu G, Sun B, Brooks SD, Yang P, Kattawar GW, Zhang X. Modeling the

inherent optical properties of aquatic particles using an irregular hexahedral ensemble. J Quant Spectrosc Radiat Transf 2017. doi:10.1016/j.jqsrt.2017.01.020.

[44] Liou KN, Yang P. Light scattering by ice crystals: Fundamentals and applications. 2016. doi:10.1017/CBO9781139030052.

[45] Yang P, Liou KN. Geometric-optics–integral-equation method for light scattering by nonspherical ice crystals. Appl Opt 2008. doi:10.1364/ao.35.006568.

[46] Organelli E, Dall'Olmo G, Brewin RJW, Tarran GA, Boss E, Bricaud A. The open-ocean missing backscattering is in the structural complexity of particles. Nat Commun 2018;9:5439. doi:10.1038/s41467-018-07814-6.

[47] Zhang X, Twardowski M, Lewis M. Retrieving composition and sizes of oceanic particle subpopulations from the volume scattering function. Appl Opt 2011. doi:10.1364/ao.50.001240.